Migration-Based Image Reconstruction Methods for Plane-Wave Ultrasound Imaging

by

Mohammed Albulayli
B.Sc., King Saud University, 2005
M.Sc., University of Victoria, 2012

A Dissertation Submitted in Partial Fulfillment
of the Requirements for the Degree of

DOCTOR OF PHILOSOPHY

in the Department of Electrical and Computer Engineering

Supervisory Committee

Migration-Based Image Reconstruction Methods for Plane-Wave Ultrasound Imaging

by

Mohammed Albulayli
B.Sc., King Saud University, 2005
M.Sc., University of Victoria, 2012

Supervisory Committee

Dr. Daler Rakhmatov, Department of Electrical and Computer Engineering
Supervisor

Dr. Panajotis Agathoklis, Department of Electrical and Computer Engineering
Departmental Member

Dr. Daniela Constantinescu, Department of Mechanical Engineering
Outside Member

Abstract

Supervisory Committee

Dr. Daler Rakhmatov, Department of Electrical and Computer Engineering
Supervisor

Dr. Panajotis Agathoklis, Department of Electrical and Computer Engineering
Departmental Member

Dr. Daniela Constantinescu, Department of Mechanical Engineering
Outside Member

Ultrasound imaging plays an important role in biomedical diagnostics due its safety, noninvasive nature, and low cost. Conventional ultrasound systems typically form an image frame by scanning the region of interest line-by-line, using a focused beam during transmission and dynamic focusing during reception. Alternatively, the region of interest can be insonified at once using a plane wave, which allows for ultrafast data acquisition rates but reduces the resulting image quality. The latter can be improved by means of coherent plane-wave compounding (CPWC), whereby multiple plane waves are emitted at different angles to obtain multiple image datasets that are subsequently combined to enhance the final compounded image.

We present two novel Fourier-domain techniques for CPWC image reconstruction from raw linear-array sensor data. In particular, we show how to modify two classic algorithms used for geophysical data processing, namely Stolt's and slant-stack depth migration under zero-offset constant-velocity assumptions, so that their new versions become applicable to plane-wave ultrasound data processing. To demonstrate the merits and limitations of our approach, we provide qualitative and quantitative comparisons with other Fourier-domain methods reported in the ultrasound literature. Our evaluation results are based on the image resolution, contrast, and similarity metrics obtained for several public-domain experimental benchmark datasets.

We also describe another novel Fourier-domain method for CPWC image reconstruction that can be used in situations where the speed of sound varies with depth in a layered propagation medium. Our technique builds on Gazdag's phase-shift migration algorithm that has been modified to handle plane-wave ultrasound data processing. Our simulation results show that the proposed method is capable of accurately imaging point targets in a three-layer medium, mimicking tissue-bone-tissue ultrasound propagation.

Table of Contents

List of Tables

List of Figures

Acknowledgments

First and foremost, I would like to express my most sincere gratitude to my supervisor Dr. Daler Rakhmatov for his encouragement, support and guidance throughout the course of my PhD program. Further, I would like to thank Dr. Panajotis Agathoklis, Dr. Daniela Constantinescu, and Dr. Chaitali Chakrabarti for their time serving as members of the supervisory and examination committees.

Also, I would like to express my deepest gratitude to my family for their love and support throughout my PhD journey.

Finally, I would like to express my sincere appreciation to the Ministry of Higher Education in Saudi Arabia and the Saudi Arabian Cultural Bureau in Canada for providing financial support during my graduate studies at the University of Victoria.

Dedication

To my wonderful parents, Ghaytha and Bani.

To my lovely wife, Bushra.

To my beloved son, Khalid.

Chapter 1

Introduction

The application of ultrasound in biomedical imaging has been studied since the 1950s [38]. One of the earliest devices used in clinical ultrasound was the reflectoscope which sent pulses through the tissue and displayed the detected echoes on an oscilloscope as amplitude versus time plots, also known as A-mode [81]. Since then ultrasound imaging has evolved to become one of the most ubiquitous diagnostic tool employed in hospitals because of its low cost, non-invasive nature, portability and safety. Modern ultrasonic devices provide high resolution real-time images without using ionizing radiation and their use includes cardiology, obstetrics and gynecology, abdominal imaging, and vascular imaging [65]. Fundamentally, clinical ultrasound is based on acoustical echo method, i.e., the part of the body under examination is insonified with an acoustic pulse which gets reflected and scattered by the variations in density of the tissues along the propagation path [65, 81]. The reflected signals, which carry the information about the mechanical properties of the body, are then received by piezoelectric sensors [81]. The image is extracted from the received signals by averaging them after supplying appropriate set of delays determined by the geometric paths between the field points and transducers. The rest of this chapter will provide an overview of ultrasound imaging system and related work.

1.1 Ultrasound Imaging System

In biomedical ultrasound imaging, the main task is to provide an image that conveys the actual internal structure of body parts under investigation. There are different modes of displaying an ultrasound image such as A-mode, M-mode and B-mode depending on the scanning mode [15]. This work is concerned with the two-dimensional B-mode imaging, which will be the focus of our discussion in the sequel. In B-mode images each pixel represents the brightness of the returned echoes. Figure 1.1 shows an example of a B-mode cross-sectional image of the carotid artery [17].

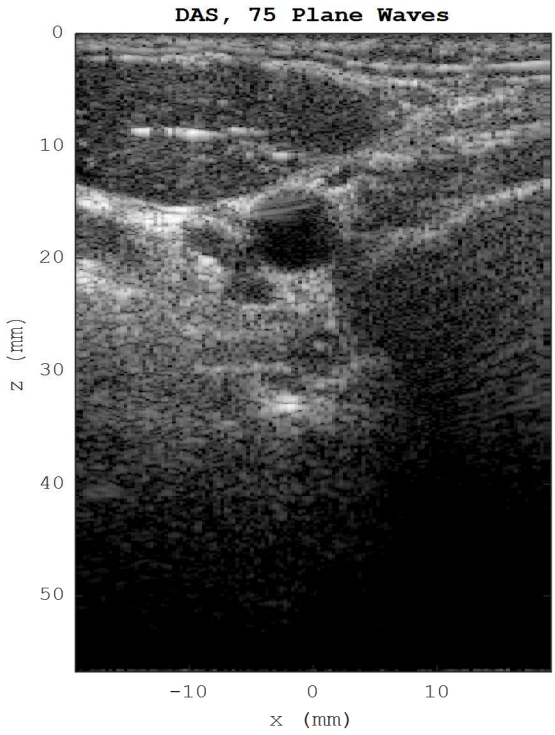

Figure 1.1: A cross-sectional image of carotid artery acquired with 75 plane waves and processed with a delay-and-sum beamformer [17].

1.2 System Components

Figure 1.2 shows the basic block diagram of the major components of a typical ultrasound system.

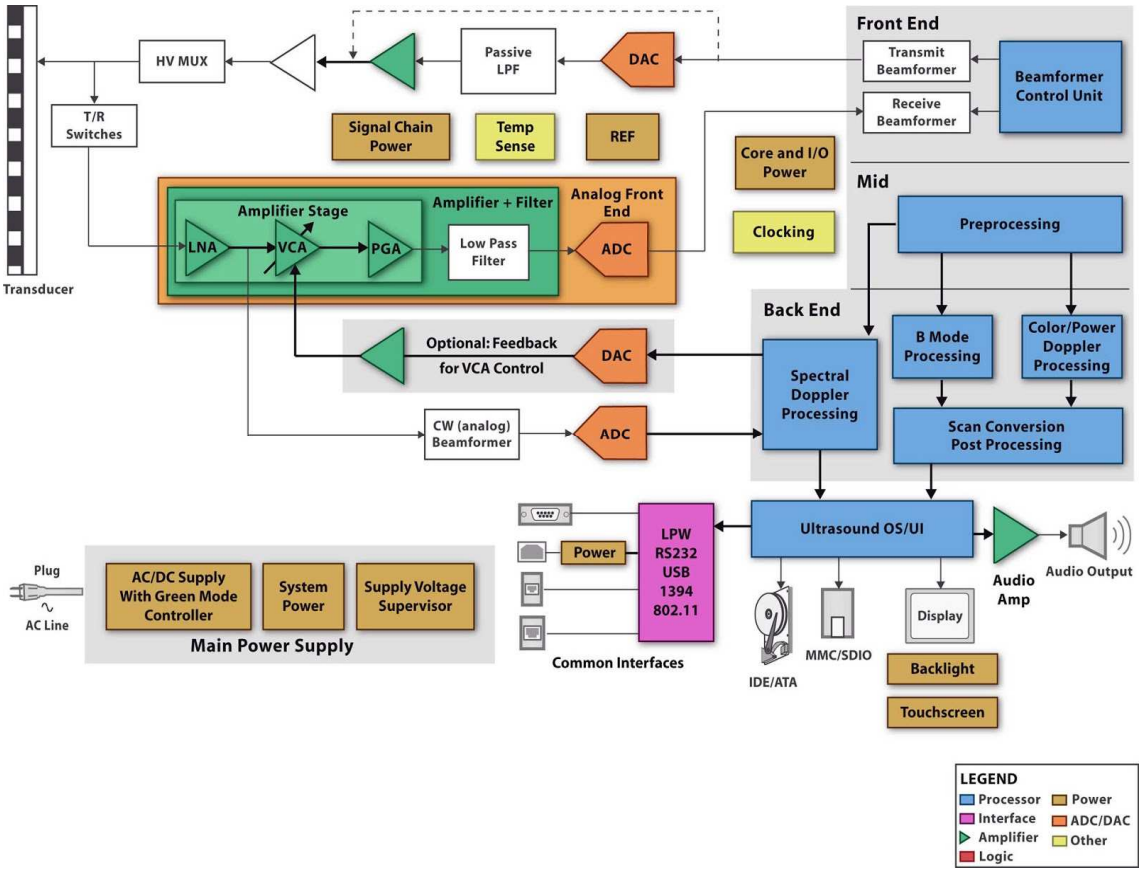

Figure 1.2: Block diagram of system components of a typical ultrasound system [5].

The Transmit Beamformer sends appropriately delayed electrical pulses through digital-to-analog converter (DAC) to provide the necessary voltage to drive the transducer elements in order to produce an acoustic wave [15]. The acoustic wave is transmitted into the medium and encounters different structures with different acoustic impedances, which in turn, causes a series of reflections. The backscattered waves are then recorded by the same transducer elements. The echoes received by the transducers result in low voltage signals due to attenuation, which is depth- and frequency-dependent. For instance, in the soft tissues the acoustic wave undergoes an attenuation of 0.5dB/(MHz-cm) [38]. Consequently, typical ultrasound systems work with carrier frequencies ranging from 2 to 15 MHz to decrease the frequency-dependent attenuation [38]. The received signal is amplified using time gain compensation (TGC), which counters depth-dependent attenuation [81]. The resulting amplified analog signal is sampled by analog-to-digital converter (ADC) and then fed to the Receive Beamformer. The latter applies appropriate delays to the output of each channel before summing them. In order to obtain the final B-mode image, several postprocessing steps are carried out. First, the envelope of the beamformed data is extracted through the quadrature demodulation and envelope detection, which is accomplished by taking the absolute value its Hilbert transform [45, 57]. This step is followed by logarithmic compression, which reduces the dynamic range of the envelope. If needed, the logarithmic compressed data is also interpolated along Cartesian coordinates to make the image suitable for display [5].

1.3 Scanning and Acquisition Modes

In B-mode imaging, there are several ways in which the raw data are acquired, such as phased array imaging, synthetic aperture imaging, and linear array imaging. Phase arrays are used to cover angular regions (usually less than 90 degrees), in which an image is divided into radial scanlines. The need to steer the beam across an angular sector imposes a strict requirement on the spacing between transducer elements: it must be half of the wavelength, which corresponds to the Nyquist rate to avoid artifacts caused by spatial aliasing [81]. In synthetic aperture imaging, on the other hand, the medium illuminated by activating one transducer element at a time, and the resulting echoes are recorded by all the elements of the receiving array [39]. As a result, the beamformed image has low resolution. In order to increase the resolution of the image, this acquisition strategy is repeated for all elements, one at a time, and the resulting frames are compounded to increase the resolution of the final image [81]. In linear array imaging, the image is acquired by scanning the region of interest line by line to form a single frame [81]. That is, the region of interest is divided into scanlines, and each scanline is imaged by an active subset of the entire array. The process starts by sending a focused pulse using the activated subset of transducer elements and waiting for all the returning echoes to arrive. Then, the next scanline is imaged by shifting the active sensor positions by one element and repeating the same process until the last scanline is reached [81]. At the end of the scanning process, the receive beamforming is used to process the acquired data. During this process dynamic focusing at different depths can be used to increase the resolution. More focal points yield

finer resolution; however, this comes at the expense of the frame rate reduction. The spacing between elements can be relaxed to as much as three wavelengths without introducing noticeable artifacts, since there is no transmit beam steering [81].

1.4 Ultrasound Image Quality

There are several important quantitative criteria used to characterize the image quality, such as resolution and contrast, which we shall summarize next.

1.4.1 Spatial Resolution

Spatial resolution is a performance metric used to measure how well the imaging system can distinguish between close points along the axial and lateral directions. The axial resolution is defined as the capability of the imaging system to distinguish objects along the beam direction. It is a function the of transmitted pulse width and the speed of sound [38]. When transmitting a pulse of M sinusoidal periods, the axial resolution can be obtained from the following formula [38]:

$$dz = \frac{cM}{2f} = \frac{\lambda M}{2}, \tag{1.1}$$

where c, f, and λ are the speed, frequency, and wavelength of the transmitted pulse, respectively. Note that the factor of two takes into account the two-way travel time of the

acoustic pulse. The above equation indicates that shorter and higher-frequency pulses yield higher axial resolution. However, as mentioned previously, as the frequency increases, so does the attenuation.

The lateral resolution, on the other hand, is a measure of the ability of the imaging system to differentiate between close points along the lateral direction parallel to the transducers. The 3-dB beamwidth, also known as full-width at half maximum (FWHM), is determined by the width D of the active aperture, the imaging depth z of interest, and the wavelength λ of the transmitted pulse [38]:

$$w_{3dB} = \frac{\lambda z}{D} = \lambda F\# \,, \tag{1.2}$$

where $F\#$ is the so-called F-number of the imaging system (the ratio z/D). The F-number is used to maintain a constant resolution throughout the entire image and control the directivity in the near-field by preventing the elements on the edges from contributing to the image [49].

1.4.2 Contrast to Noise Ratio

Contrast to noise ratio (CNR) is a measure of the system's ability to distinguish a cyst object from the speckle background [81]. The speckle is the grainy texture in the image caused by the structures that are much smaller in size than the wavelength of the

transmitted beam [40]. The CNR can be estimated using the following formula [48]:

$$\mathrm{CNR} = 20\log_{10}\left(\frac{|\mu_{in}-\mu_{out}|}{\sqrt{(\sigma_{in-}^2\sigma_{out}^2)/2}}\right), \tag{1.3}$$

where μ_{in} and μ_{out} are the average signal levels inside the anechoic cyst region, while σ_{in} and σ_{out} are the standard deviations inside and outside the anechoic cyst region.

1.5 Related Work

Over the past decade, receive beamforming has been one of the main research areas in ultrasound imaging. Several beamforming schemes have been applied to improve the image resolution and contrast. Sasso and Cohen [71] applied minimum variance distortionless response (MVDR) beamforming coupled with the spatial smoothing preprocessing step [72] to decorrelate coherent echoes. Their work showed very promising results in terms of both resolution and contrast enhancement and indicated that adaptive beamforming algorithms can be successfully applied to ultrasound imaging. Similar approaches to [70] were examined in [79, 6]. Synnevag *et al.* [79] included a diagonal loading to the spatially smoothed covariance matrix and demonstrated robustness against errors in the estimated velocity. Asl and Mahloojifar [6] applied a so-called Eigen-beamformer to ultrasound imaging. The basic idea of the Eigen-beamformer is to project the weights onto the signal space which increases its robustness compared to the standard

MVDR beamformer [73]. In [6] it was shown that the Eigen-beamformer outperforms even the regularized MVDR beamformer in terms of resolution and contrast in the presence of errors in the estimated steering vector. In [36], Hollman *et al.* introduced and applied the coherence factor to ultrasound imaging. The coherence factor (CF) is a ratio of the coherent sum across the array elements to the incoherent sum: it measures the relative distribution of ultrasonic energy between the mainlobe and sidelobe of the beampattern [36]. In [64] it was shown that the quality of the image could be improved by weighting the output beamformed data by the coherence factor, since it suppresses energy coming from the sidelobes, thus improving the overall contrast. Additionally, they have shown mathematically that multiplying the output of the delay-and sum (DAS) or MVDR beamformer by the CF is equivalent to implementing a Wiener post-filter or Wiener beamforming, respectively. All of these previous works treated ultrasound received echoes as narrowband signals. Narrowband MVDR beamforming can be extended to process broadband signals both in the time domain and in the frequency domain [86]. In the time domain, the output of each sensor is processed by an finite impulse response (FIR) filter whose weights are optimized to minimize mean-squared error of the output [28-30, 66, 67, 86]. In the frequency domain, the received signal at each sensor is Fourier-transformed, so that a narrowband beamforming can be used to process frequencies across narrow bands from each sensor; then, the outputs from all narrowband beamformers are added together and inverse-Fourier-transformed to obtain the final beamformed data [86, 35]. Naturally,

the broadband beamformers are superior to their narrowband beamformers counterparts in terms of image resolution and contrast; however, most of the implementations of broadband beamformers are done off-line because of their high computational complexity.

Recently, many researchers have targeted efficient implementations of ultrasound beamformers. The following example gives an insight into the amount of data involved to form one frame of an ultrasound image. Consider an ultrasound system that assumes the speed of sound to be c = 1540 m/s and uses sampling frequency f_s = 40 MHz. In addition, suppose that the depth of the region to be imaged is z = 15 cm [81]. It follows that the duration of the received signals is $T = 2z/c \approx 195$ μsec. That gives a number of samples $N = T f_s \approx 7800$ for one RF line. Assuming that each scanline is generated using M = 64 sensors, the total number of samples becomes $N_t = N M \approx$ 500e3. Assuming that each frame consists of N_s = 64 scanlines, the total number of samples per frame is $N_f = N_t N_s \approx$ 30e6 samples. It is obvious that a high sampling frequency and a large number of sensors result in the heavy computational loads during the beamforming step. Several research groups have taken different approaches aiming to decrease the computational load associated with receive beamforming. Tur *et al*. [87] have applied a novel sampling technique, known as finite rate of innovation (FRI), to the output of a single ultrasound sensor. In the FRI model, a stream of pulses can be sampled at a rate lower than the Nyquist rate, based on the fact that each pulse is determined by two variables: its time delay (location) and its amplitude. Therefore, each pulse can be represented by at least two samples in order to recover both

variables [19]. In their work, they showed that the sampling rate at the front-end can be reduced by 8-fold in comparison to the Nyquist rate. In [91], Wagner *et al.* extended the work in [87] to multiple sensors to produce a single frame and named their method 'compressed beamforming'. Their method achieved 8-fold reduction during the data acquisition stage. In [12], the authors have implemented the compressed beamforming in the frequency domain and showed that 28-fold reduction in the sampling rate can be achieved in comparison with standard beamforming. In [3], the authors proposed a method in which the receive aperture was dynamically and uniformly downsampled. Instead of using specially optimized sparse arrays [41] that reduce the artifacts caused by the grating lobe associated with their non-uniform element spacing, a switching mechanism was introduced (based on the coherence factor) to dynamically select a uniform downsampled pattern of activated elements.

Synnevag *et al.* [80] presented a low-complexity data dependent beamformer, based on the idea that was briefly mentioned earlier in [90]. The basic approach is to use a predefined distortionless set of apodization windows and choose the one that results in the lowest output power. Their technique yielded a significant improvement in the image resolution over fixed nonadaptive beamformers. This method has linear complexity, as opposed to cubic complexity of the MVDR beamformer that involves covariance matrix inversions. A gradient-driven and reduced-rate beamformer based on generalized sidelobe canceler (GSC) was proposed in [44]. In this method, the covariance matrix inversion process was

approximated by the use of classic unconstrained iterative optimization algorithms, such as conjugate-gradient (CG) minimization. They showed that the output of the GSC beamformer using CG with three iterations was comparable to the GSC beamformer with exact inversion in terms of resolution and contrast with 20% computational savings. In [4], a hybrid scheme of adaptive and nonadaptive beamforming was proposed to reduce the computational load associated with the fully adaptive GSC beamforming. Building on the ideas presented in [44, 80], the proposed method in [4] uses the coherence factor: if the CF of a given input snapshot is larger than a predefined threshold, then the adaptive GSC beamformer is used to process it, otherwise nonadaptive DAS beamformer is used. In [68], the authors proposed a two-pass beamforming scheme that combined adaptive and nonadaptive methods to achieve high-quality ultrasound images at low computational cost. In the first pass, the buffered snapshots were nonadaptively beamformed to obtain preliminary envelope information, while during the second pass adaptive beamforming was applied to a subset of buffered snapshots selected based on predefined envelope thresholds. Nilsen and Hafizovic [63] applied an adaptive beamspace beamformer that used three beams where the most energy was concentrated. The obtained imaging results were comparable to those of the fully adaptive MVDR beamformer. Beamspace beamformers work in the beamspace domain instead of the element space. That is, instead of using the spatial information of the transducer elements to distinguish the desired signal from the interference and noise, the beamspace beamformer uses the spatial information of a set of orthogonal beams to differentiate between the desired signal and the interferers. Each

beamformer consists of M sensors capable of generating M orthogonal beams, but only a few of them are needed to produce an output close to that of the MVDR beamformer [86, 63].

As mentioned earlier, in order to generate one frame, we need to illuminate the region of interest, also known as the field of view (FOV), N_e times, where N_e is the number of emitted focused pulses per frame, that is, the number of scans N_s performed. Using $N_e = N_s = 64$ from our previous example, the time needed to produce one frame is $T_f = N_e\, T \approx 12.5$ ms. Therefore, the frame rate is given by $F_r = 1/\ (T_f + D_t) \approx 80$ frames/s, assuming the deadtime $D_t = 0$ for convenience. The deadtime D_t is defined as the time needed for the returning waves to decay to a negligible level [81, 91]. Hence, regardless of the available computational power, we cannot break the physical frame rate limit imposed by the round-trip travel time T of an acoustic wave. The frame rate $F_r \approx 80$ frames/s calculated above does not take into account the processing time and deadtime D_t. Typical ultrasound systems support frame rates in the range of 30 to 60 frames per second [81], which fail to adequately capture and track, for instance, the heart movements during the cardiac cycle [82]. The physical constraint imposed by the acoustic wave propagation stalled any effort to increase the frame rate of the conventional ultrasound imaging and that was the conventional wisdom among the ultrasound community. During the 1990s, however, J. Lu and his co-authors published a series of pioneering papers in which they developed the theory of high frame rate imaging based on the concept of limited-diffraction beams [53-55]. In their

work, a single broad pulsed wave is transmitted into the medium and a limited-diffraction beam is used to weigh the received echoes. In their work, they achieved the ultrafast frame rate of 3750 frames/s for the depth ranges of up to 20 cm. The key idea is to apply the two-dimensional Fourier transform to the received echoes in the (x, t)-domain to obtain the spectrum in the (k_x, f)-domain, and then extract the object function in the (k_x, k_z)-domain by interpolating the spectrum on a dispersion grid represented by the equation

$$k_z = \sqrt{\frac{f^2}{c^2} - {k_x}^2} = \sqrt{k^2 - {k_x}^2} \quad , \tag{1.4}$$

using different interpolation methods, such as linear or truncated sinc functions [33, 47, 83]. After the interpolation step, the (k_x, k_z)-domain is the Fourier transform of the imaged object. Finally, the two-dimensional inverse Fourier transform can be applied to the interpolated data to obtain the object function in the (x, z)-domain. In [11], Cheng and Lu extended the work in [53, 54] to include spatial compounding scheme with different types of limited-diffraction beams and steered plane waves to improve the signal to noise ratio (SNR) and resolution. The resulting images from different transmissions were added coherently to improve the resolution and added incoherently to reduce the speckle level. The term "incoherent compounding" means combining the intensity images to smooth out the speckle pattern, while the term "coherent compounding" means combining the received echoes from different illuminations, i.e., it acts on the pressure intensity [60]. Kruizinga *et al*. replaced the spectral remapping process, represented by the interpolation step

mentioned above, by using the non-uniform Fourier transform (NUFFT) along the temporal axis [46]. They implemented the NUFFT with Kaiser-Bessel min-max interpolation [20] and demonstrated that their method improved the SNR by 4 dB and offered 15% speed-up of the processing time in comparison to linear interpolation with an upsampling factor of two. In [21], Garcia *et al*. adapted Stolt's migration method, also known as the *f-k* migration algorithm, to plane wave ultrasound imaging. Stolt's migration is a well-known method in seismology and is considered to be among the fastest migration algorithms [56, 78], to be explored in greater detail in later chapters. The method is based on the exploding reflector model (ERM) [14], where reflectors "explode" at time $t = 0$, so that the two-way wave propagation can be reduced to one-way propagation (from a reflector to the surface). The method works entirely in the Fourier domain. Garcia *et al*. showed that their modified Stolt's migration method applied to compounded plane wave ultrasound produced images of quality similar to that of multi-focused ultrasound beamforming. In [8], Bernard *et al*. applied the Fourier slice theorem to the radially sampled spectrum of the received signal to recover the spectrum of the desired image. More precisely, by simulating several steering angles at reception for a given angle at transmission, they managed to reconstruct the spectrum of the desired image [8]. In [9], the authors applied sparse regularization in the Fourier domain image reconstruction and demonstrated that their method could outperform classical approaches in terms of the resulting image quality.

All of the algorithms that deal with plane-wave imaging mentioned so far have been implemented in the Fourier domain. Montaldo *et al.* [60], on the other hand, implemented plane-wave image reconstruction in the time domain using the conventional DAS beamformer as shown in Figure 1.3. The process starts by sending a single plane wave and then collecting the retuning echoes. Having obtained all the echoes, the image plane is divided into a number of synthetic scanlines, where each scanline is constructed using DAS beamforming. To speed up the process a set of parallel DAS beamformers could be used, one for each scanline. Montaldo *et al.* also proved that sending N_e plane waves, each tilted at an angle θ with respect to the aperture axis, is equivalent to using conventional multi-focusing imaging with $N_e < M$, where M is the number of transducer elements. The delays needed to steer and focus the received acoustic echoes at the target location (x_s, z_s) are given by [60]:

$$\tau_{tx}(\theta, x_s, z_s) = \frac{(x_s \sin\theta + z_s \cos\theta)}{c}, \tag{1.5}$$

$$\tau_{rx}(x_s, z_s, x_i) = \frac{\sqrt{z_s{}^2 + (x_s - x_i)^2}}{c}, \tag{1.6}$$

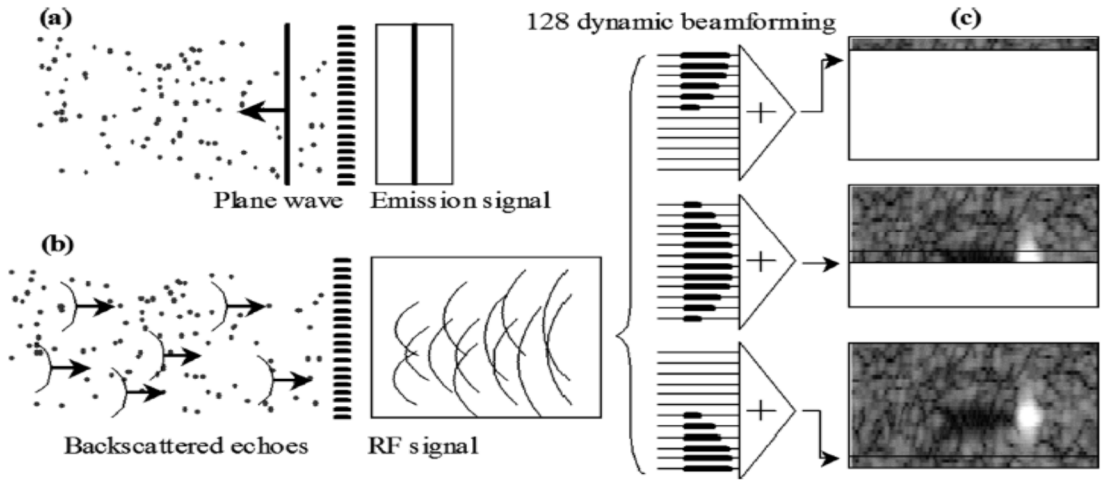

Figure 1.3: (a) An ultrasonic array insonifies the medium using a plane-wave transmission. (b) Backscattered RF signals are recorded by the transducer array. (c) The beamforming procedure involves applying time delays laws and summations to the raw RF signals to focus in the receive mode [60].

where $\tau_{tx}(\theta, x_s, z_s)$ is the time needed for the transmitted pulse to reach the point (x_s, z_s), and $\tau_{rx}(x_s, z_s, x_i)$ is the time needed for a reflected echo from the point (x_s, z_s) to reach the receiving element x_i. Therefore, two-way time travel for a plane wave tilted at an angle θ (see Figure 1.4) is given by:

$$\tau(\theta, x_s, z_s, x_i) = \tau_{tx}(\theta, x_s, z_s) + \tau_{rx}(x_s, z_s, x_i)\,. \tag{1.7}$$

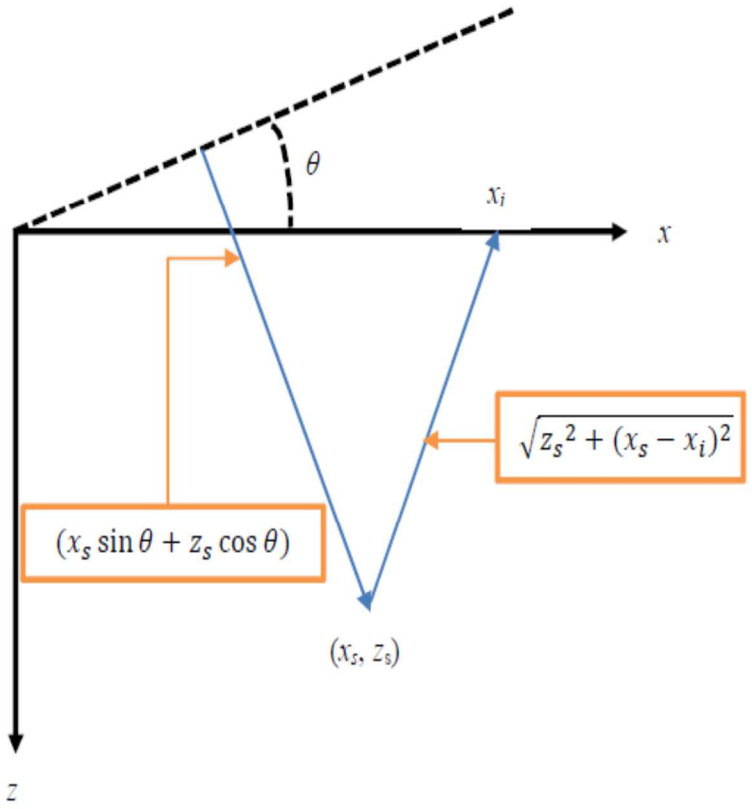

Figure 1.4: Two-way time delays for a plane wave tilted at an angle θ.

In [52], it was demonstrated that applying adaptive sign coherence factor (SCF) weighting to DAS beamforming improved both axial and lateral resolution in comparison to conventional DAS beamformers. The authors of [58] have investigated the application of the filtered-delay-multiply-and-sum (F-DMAS) beamforming to plane wave imaging, showing improvements in both lateral resolution and contrast. Meanwhile, Cohen

et al. [16] have demonstrated that the (x,f)-domain DAS beamformer using only a quarter of input samples can, in fact, produce similar quality images as those obtained by conventional time domain DAS beamforming that processes all samples, i.e., the former is considerably less expensive than the latter.

Several studies have also dealt with the application of adaptive beamforming to ultrasound plane-wave imaging. For example, Deylami *et al.* [18] employed an improved version of MVDR beamformer by Eigen-decomposing the covariance matrix and using generalized coherence factor (GCF) to highlight the coherent part of images. In [88], Varray *et al.* have applied MVDR beamformer coupled with the phase coherence factor (PCF) to the IQ data, which reduces the number of samples (compared with raw RF data) and guarantees invertibility of the covariance matrix. Their results showed not only an improvement in the contrast and resolution (as in [18]), but also a reduction in the amount of computations. In another attempt to improve the lateral resolution and contrast, Chau *et al.* [10] proposed a new weighting factor for the output of the MVDR beamformer known as the short-lag spatial coherence weighting. Their technique resulted in improvements of 7%-55% in lateral resolution and of 2.5%-13% in contrast. Finally, Rindal and Austeng developed a double adaptive weighting technique, where the first set of weights is the traditional MVDR weight vector and the second set of weights is used for coherent compounding [69]. Their technique produced images with significantly improved lateral resolution and contrast; however, the amount of computations involved was significant.

It is important to note that migration techniques used in seismology (e.g., Stolt's and Gazdag's [24] methods among others) have been successfully applied to synthetic-aperture ultrasound imaging [37, 59, 74, 75], since the data acquisition setup in both cases is somewhat similar (unlike imaging with plane waves). For example, Stepinski [75] applied Stolt's migration to monostatic synthetic aperture imaging. After taking the 2-D FFT of the raw data, he applied 2-D match filter followed by Stolt's transformation: his results offered improved performance in terms of both lateral and axial resolution compared to DAS beamforming [75]. In [74], the authors developed an algorithm named multi-layer omega-k (MULOK), which is a combination of phase-shift migration (dealing with multilayer structures) and Stolt's remapping within individual layers (for efficiency purposes). In their work, they managed to lower the computational cost and increase the spatial resolution for multilayered media. As for full matrix imaging (such as multistatic NDT imaging), the authors of [37] applied Stolt's migration, which improved point-spread function of the imaging system and was more efficient than conventional DAS beamforming. In [59], the authors have implemented an efficient reconstruction method utilizing well-known nonzero-offset Stolt's migration in the context of multistatic synthetic aperture ultrasound imaging. Their results showed lateral resolution improvements in comparison to DAS beamforming. However, in terms of contrast and axial resolution DAS performed better.

To conclude this section, we point out that plane-wave ultrasound image reconstruction using seismic migration techniques is still a relatively unexplored area, which has motivated the work presented here.

1.6 Scope and Contributions

The rest of this dissertation consists of six more chapters. Since our work adapts certain algorithms from the seismic imaging literature, a summary of the different seismic migration techniques is presented in Chapter 2.

In Chapter 3, we present our two novel Fourier-domain techniques for plane-wave ultrasound image reconstruction that can be used as an alternative to conventional DAS beamforming and the existing Fourier-domain methods [11, 14, 21]. In particular, we show how to modify two classic algorithms used for geophysical data processing (namely, Stolt's and slant-stack depth migration under zero-offset constant-velocity assumptions), so that we can use their new versions for plane-wave ultrasound data processing. Our derivations of the proposed plane-wave constant-velocity Stolt's and slant-stack migration methods rely on the same underlying model, which is potentially applicable to other fields such as nondestructive testing (NDT).

Chapter 4 provides qualitative and quantitative comparisons with other Fourier-domain methods reported in the ultrasound literature: Lu's method [11, 50], Garcia's method [21], and Fourier-slice beamforming [8, 9]. The evaluation results are based on the image resolution, contrast, and similarity metrics obtained for several public domain experimental benchmark datasets [13]. These results indicate that our proposed methods often produce either the best or second-best image contrast, resolution, and similarity indicators, which demonstrates their competitive potential.

In Chapter 5, we present another novel Fourier-domain technique for reconstructing plane-wave ultrasound images when the speed of sound varies with depth in a propagation medium. Starting from classic Gazdag's phase-shift migration method used for geophysical data processing, we show how one can obtain modified zero-offset model equations applicable to plane-wave ultrasound imaging. Our proposed method can potentially be used for brain imaging through the skull (transcranial ultrasound). In Chapter 6, our initial simulation results using K-WAVE MATLAB toolbox show that the proposed plane-wave phase-shift migration method is capable of accurately imaging point targets in a three-layer medium, mimicking tissue-bone-tissue ultrasound propagation.

Lastly, Chapter 7 provides concluding remarks and outlines several ideas for the future work.

Chapter 2

Basics of Seismic Imaging

2.1 Introduction

Acoustic imaging is used to construct high resolution images from the reflected data by identifying the spatially variant parameters of the Earth, human body, material properties, etc. [27]. In human body, for example, the aim is to identify tissues and organs; in non-destructive testing imaging, the goal is to detect defects within materials; while in seismology, the objective is to reconstruct an image of the geological structure of the Earth [7]. The aforementioned imaging modalities use the same mathematical model based on the wave equation [27]. In the following, the principles of acoustic imaging, as used in seismology, is discussed. In later chapters we show how one can adapt seismic imaging techniques presented here to plane-wave biomedical ultrasound imaging.

2.2 Acoustic Imaging by Migration

When transmitting an acoustic wave into a homogenous medium, every point within the medium becomes a secondary source, emitting a spherical wave in accordance with the Huygens principle [14, 26]. These secondary sources form diffraction hyperbolic curves in

the (x, t)-domain, and such hyperbolas can be mathematically expressed by the following equation [14]:

$$\tau(x_s, z_s) = 2\frac{\sqrt{{z_s}^2+(x_s-x_i)^2}}{c}, \tag{2.1}$$

where (x_s, z_s) and x_i are the coordinates of the target and the receiving element, respectively. Note also that the deeper the sources, the flatter the curves are. The migration imaging process can be thought of as the reverse process of diffraction, that is, these hyperbolas are integrated back to their original sources [14]. Reflection seismology dates back to the 1920s, and by the 1940s several methods had been developed in order to improve the transformation of the raw data into a better image of the subsurface [22, 70]. These methods would move apparent subsurfaces to their correct positions; hence, they were referred to as migration [70]. By the 1960s, geophysicists started to move to the wave-equation-based methods such as Kirchhoff integration [22]. Kirchhoff integration amounts to summing the traces over hyperbolas in the (x, t)-domain based on the geometry of the targets and the acquisition sensors. It is also known as DAS beamforming in the engineering community [21, 51]. In the 1970s, Claerbout and his group developed numerical approximations of the wave equation, known as the parabolic wave equation, which can be solved by implicit and explicit finite-difference methods in the (x, t) domain and (x,f) domain [14]. These methods can handle changing velocities along the horizontal and vertical axes. Explicit finite-difference migration in the frequency domain is more attractive than that in the time

domain due to the former's computational efficiency and convolution resemblance; consequently, it has received more attention [31, 61]. From digital signal processing perspective, frequency-domain extrapolators are a set of spatial non-causal complex-valued finite impulse response (FIR) filters [61]. Several algorithms have been developed to improve the performance of the FIR extrapolators with minimum number of coefficients, as reported in [31, 42, 84, 61]. In 1978 a major breakthrough occurred in seismic imaging, when R. Stolt published his work in which he solved the migration problem by using the Fourier transform [78]. Stolt's migration is implemented in the (k_x, f)-domain, and it focuses the entire image in one step by interpolation, which makes it the fastest migration method. One drawback of Stolt's migration is that it assumes a constant velocity throughout the medium. In an effort to overcome this drawback, Gazdag proposed a new method in the same year. It is also based on the Fourier transform and referred to as phase shift migration. It deals with changing velocity along the vertical axis by backpropagating the wavefield in incremental steps [24]. Later, Gazdag and Sguazzero [23] extended the phase shift migration to handle velocity variations along the vertical and horizontal axes. This method is regarded as one of the most accurate migration methods; however, it is computationally expensive.

2.3 Seismic Data Acquisition and Processing

The seismic raw data is typically acquired in the common shot gather (CSG) "mode" configuration. That is, the process starts "on land survey" by firing the source and then

receiving the echoes by a set of aligned geophones [43]; then, the source is moved to another position and the same experiment is repeated. The acquired data in this geometrical setting is referred to as prestack data and is represented graphically by the so-called stacking chart shown in Figure 2.1 [32, 62]. There are three geometrical factors that must be taken into consideration before processing the raw data: the location of the geophone g, the location of the source s, and the position of the subsurface reflection point [43]. The horizontal position of the subsurface reflection point can be approximated by assuming its location mid-way between the source and the receiving geophone, referred to as the midpoint [43]:

$$m = \frac{g+s}{2}. \tag{2.2}$$

By collecting all the traces that have common midpoint m, the common midpoint (CMP) gather is obtained as shown in Figure 2.2 [43]. Before stacking, that is, 'summing' the traces that make up the CMP gather in order to enhance the signal to noise ratio, the traces must be corrected for the normal moveout (NMO). Each trace is delayed by its corresponding offset given by [43]:

$$h = \frac{g-s}{2}. \tag{2.3}$$

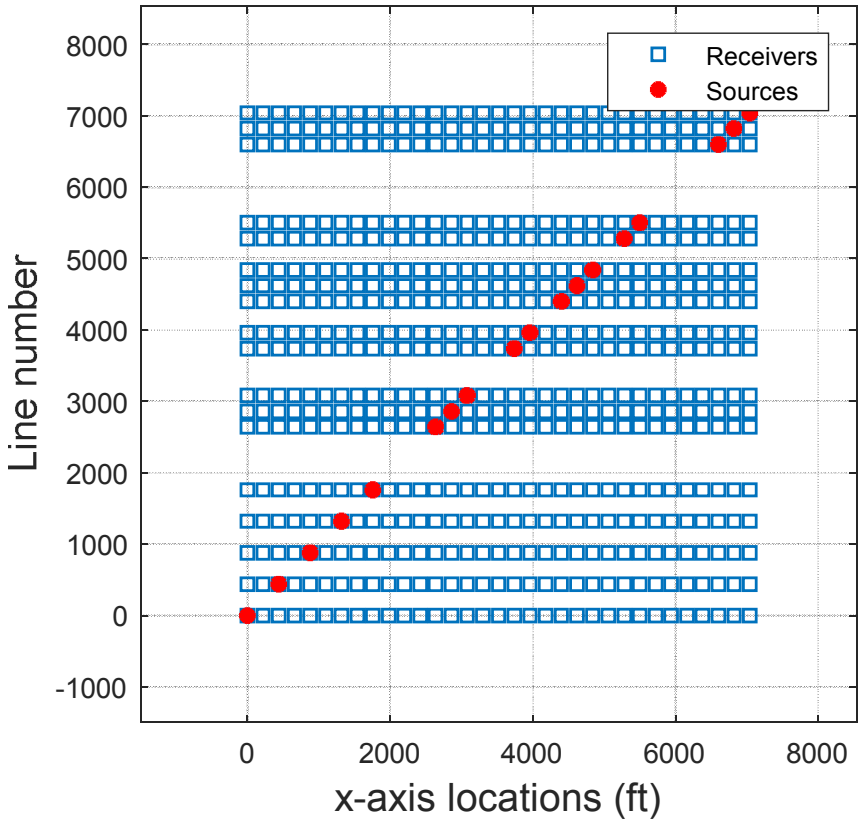

Figure 2.1: Stacking chart of the seismic data [62].

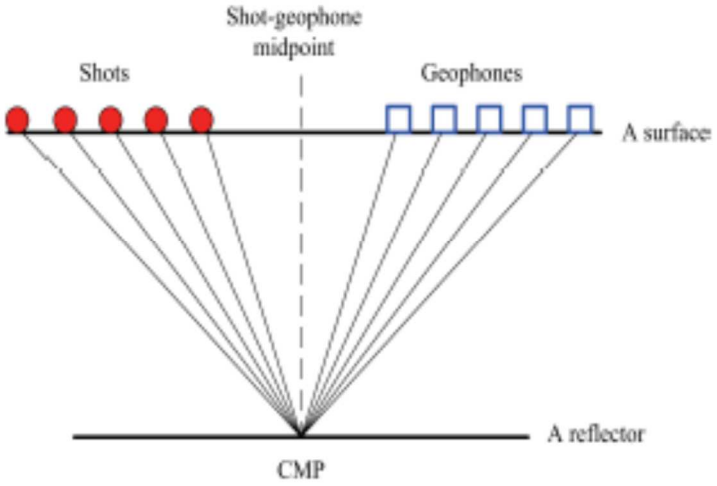

Figure 2.2: Common midpoint gather configuration [62].

The stacking process is similar to delay-and-sum beamforming, i.e., each trace will be delayed by:

$$t(h) = \sqrt{t_0^2 + \frac{4h^2}{c^2}}\,, \tag{2.4}$$

where t_0 is the time needed to travel the vertical zero-offset distance (at $h = 0$), and c is the speed of sound [22]. The data at this stage is termed zero-offset section, and the migration algorithm applied to it is referred to as poststack migration.

2.4 Exploding Reflector Model

The exploding reflector model (ERM) is a thought experiment which assumes that all points in the medium (that is, the secondary sources mentioned earlier) "explode" simultaneously at time $t = 0$, as shown in Figure 2.3 below [14].

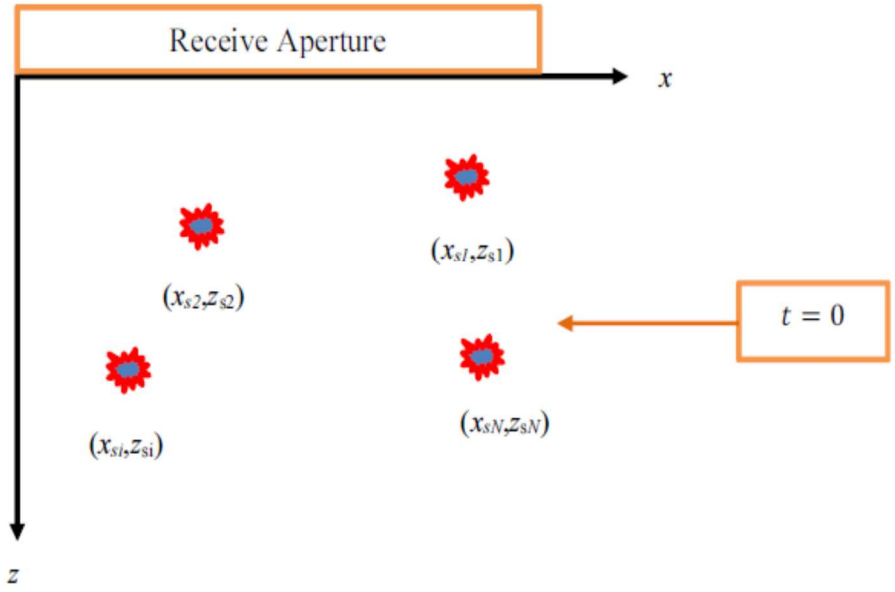

Figure 2.3: Exploding reflector model (ERM).

The ERM provides an intuitive illustration of the zero-offset migration imitating one-to-one correspondence between the transmitter and receiver; that is, data traces are obtained by sending and receiving at the same position [14]. The advantage of ERM is that one needs to be concerned with upgoing propagation only and use half the speed of

sound, which leads to the following travel-time relationship:

$$\hat{\tau}(x_s\ z_s) = \frac{\sqrt{z_s^2+(x_s-x_i)^2}}{\hat{v}}, \tag{2.5}$$

where $\hat{v} = \frac{c}{2}$, x_i is the location of the i^{th} sensor, (x_s, z_s) is the coordinate of the exploding reflector, and $\hat{\tau}(x_s\ z_s)$ is the one-way travel time from the reflector to the recording sensor located at x_i.

2.5 Stolt's Migration

Stolt's migration algorithm works in the (k_x, f)-domain, which makes it fast compared to other migration techniques [22]. To start, let $\mathrm{P}(x, z, t)$ denote a scalar wavefield that satisfies the following wave equation [56]:

$$\nabla^2\mathrm{P}(x,z,t) - \frac{1}{\hat{v}^2}\frac{\partial^2}{\partial t^2}\mathrm{P}(x,z,t) = 0\,, \tag{2.6}$$

where $\hat{v} = \frac{c}{2}$ is the one-way propagation velocity under the ERM assumption. It is desired to obtain the field at the time of the explosion $\mathrm{P}(x, z, t = 0)$ - the imaging condition - from the knowledge of the recorded field at the surface $\mathrm{P}(x, z = 0, t)$ - the boundary condition. The wavefield $\mathrm{P}(x, z, t)$ can also be written as:

$$\mathrm{P}(x,z,t) = \int \int \Psi(k_x,z,f)\, e^{j2\pi(k_x x+ft)} dk_x df\,, \tag{2.7}$$

where $\Psi(k_x,z,f)$ is the two-dimensional Fourier transform of $\mathrm{P}(x,z,t)$ over the (x, t) domain. Substituting equation (2.7) into equation (2.6) yields:

$$\int \int \left[\frac{\partial^2}{\partial z^2}\Psi(k_x,z,f) + \left(\frac{4\pi^2 f^2}{\hat{v}^2} - 4\pi^2 {k_x}^2\right)\Psi(k_x,z,f)\right] e^{j2\pi(k_x x+ft)} dk_x df = 0\,. \tag{2.8}$$

Letting $k_z^2 = \frac{f^2}{\hat{v}^2} - k_x^2$, we obtain

$$\int \int \left[\frac{\partial^2}{\partial z^2}\Psi(k_x,z,f) + 4\pi^2 k_z^2 \Psi(k_x,z,f)\right] e^{j2\pi(k_x x+ft)} dk_x df = 0\,. \tag{2.9}$$

Note that the above equation represents the inverse Fourier transform of the terms between the square brackets. The Fourier transform uniqueness property states that if a function vanishes everywhere, then so does its Fourier transform; therefore, [56]:

$$\frac{\partial^2}{\partial z^2}\Psi(k_x,z,f) + 4\pi^2 k_z^2 \Psi(k_x,z,f) = 0\,, \tag{2.10}$$

where k_z is the wavenumber along the vertical axis. It is related to the temporal frequency f, the horizontal wavenumber k_x, and the velocity $\hat{v}$ of the ERM model through the

dispersion relation, $k_z^2 = \frac{f^2}{\hat{v}^2} - k_x^2$. The general solution of equation (2.10) takes the following form:

$$\Psi(k_x, z, f) = C_{down}(k_x, f)\, e^{-j2\pi k_z z} + C_{up}(k_x, f)\, e^{j2\pi k_z z}\,, \tag{2.11}$$

where $C_{down}(k_x, f)$ and $C_{up}(k_x, f)$ are the two solution parts associated with downgoing and upgoing waves, respectively. The ERM model, however, allows us to focus on $C_{up}(k_x, f)$ only. Letting $C_{down}(k_x, f) = 0$ and given that $C_{up}(k_x, f) = \Psi(k_x, z = 0, f)$ at $z = 0$, we have:

$$\Psi(k_x, z, f) = \Psi(k_x, 0, f)\ e^{j2\pi k_z z}\ . \tag{2.12}$$

Note that, $\Psi(k_x, z = 0, f)$ is the two-dimensional Fourier transform of the recorded data $\mathrm{P}(x, z = 0, t)$. Equation (2.12) essentially states that the desired field spectrum $\Psi(k_x, z, f)$ can be determined by extrapolating the recorded field spectrum $\Psi(k_x, z = 0, f)$ to any point in space using the extrapolation operator $e^{j2\pi k_z z}$ [26, 51]. Essentially, the extrapolation operator $e^{j2\pi k_z z}$ phase shifts the recorded data to the depth $z > 0$, and for this reason equation (2.12) is also known as downward continuation operation [14]. Substituting equation (2.12) into equation (2.7) and setting $t = 0$ (that is, invoking the imaging condition) we obtain:

$$\mathrm{P}(x,z,0) = \int \int \Psi(k_x, z=0, f)\, e^{j2\pi(k_x x + k_z z)} dk_x df \ . \qquad (2.13)$$

To make use of the FFT, we need to change the integration variable from f to k_z. By solving $k_z^2 = \frac{f^2}{\hat{v}^2} - k_x^2$ for the temporal frequency variable f, one obtains $f = \hat{v}k_z\sqrt{1+\left(\frac{k_x}{k_z}\right)^2}$. After taking the derivative of the variable f with respect to the wavenumber k_z, one obtains $\frac{df}{dk_z} = \hat{v}/\sqrt{1+\left(\frac{k_x}{k_z}\right)^2}$. After substituting the above formulas into equation (2.13), we have:

$$\mathrm{P}(x,z,t=0) = \int \int_{f^2 > \hat{v}^2 k_x^2} \frac{\hat{v}\Psi\left(k_x,\ 0,\ \hat{v}k_z\sqrt{1+\left(\frac{k_x}{k_z}\right)^2}\right)}{\sqrt{1+\left(\frac{k_x}{k_z}\right)^2}} e^{-j2\pi(k_x x + k_z z)} dk_x dk_z \ . \qquad (2.14)$$

Equation (2.14) is the basis of Stolt's migration algorithm [56]. One first Fourier-transforms the recorded data $\mathrm{P}(x, z=0, t)$ along the x-axis and t-axis which results in $\Psi(k_x, z=0, f)$. Next, due to the condition $f^2 \leq \hat{v}^2 k_x^2$, the evanescent waves are removed from the data in the (k_x, f) space. After that, the resulting data $\Psi(k_x, z=0, f)$ is evaluated on a set of frequencies given by $f(k_z) = \hat{v}k_z\sqrt{1+\left(\frac{k_x}{k_z}\right)^2}$, to obtain the interpolated data in the (k_x, k_z) space, and then scaled by the factor $\hat{v}/\sqrt{1+\left(\frac{k_x}{k_z}\right)^2}$, or more compactly:

$$\widehat{\Psi}(k_x, 0, k_z) = \frac{\hat{v}\Psi\left(k_x,\ 0,\ \hat{v}k_z\sqrt{1+\left(\frac{k_x}{k_z}\right)^2}\right)}{\sqrt{1+\left(\frac{k_x}{k_z}\right)^2}}. \quad (2.15)$$

The interpolated spectrum $\widehat{\Psi}(k_x, z = 0, k_z)$ represented by the above equation, is then inverse Fourier-transformed back to the (x, z) domain to obtain the final migrated image.

2.6 Slant-Stack Migration

Let $\Phi(x, z, f)$ denote the wavefield which is Fourier-transformed along the temporal axis. Now, after applying the inverse Fourier transform along the k_x-axis, we have:

$$\Phi(x, z, f) = \int \ \Psi(x, z, f)\ e^{j2\pi k_x x} dk_x = \int \ \Psi(k_x, z = 0, f)\ e^{j2\pi(k_x x + k_z z)}\, dk_x\ . \quad (2.16)$$

Fixing $k_x = p_x f$, where p_x is referred to as the Fourier-domain slant parameter, we obtain the following equation after changing the integration variable from k_x to p_x:

$$\Phi(x, z, f) = \int \ |f|\ \Psi(p_x f, z = 0, f)\ e^{j2\pi(p_x f x + k_z z)}\, dp_x\ . \quad (2.17)$$

Note that each p_x value corresponds to a particular reflection slope $\frac{dx}{dt} = \frac{\sin\alpha}{\hat{v}}$, where α is a propagation angle of an ERM wavefront upgoing to the surface.

After plugging the dispersion equation

$$k_z = \frac{f}{\hat{v}}\sqrt{1-\frac{\hat{v}^2 k_x^2}{f^2}} = \frac{f}{\hat{v}}\sqrt{1-\hat{v}^2 p_x^2} \tag{2.18}$$

into equation (2.17), we get:

$$\Phi(x,z,f) = \int |f|\,\Psi(p_x f, z=0, f)\; e^{j2\pi f\left(p_x x+\frac{z}{\hat{v}}\sqrt{1-\hat{v}^2 p_x^2}\right)}\, dp_x\,. \tag{2.19}$$

Letting

$$\tau(p_x, x, z) = p_x x + \frac{z}{\hat{v}}\sqrt{1-\hat{v}^2 p_x^2} \tag{2.20}$$

in equation (2.19) and invoking the imaging condition when taking the inverse Fourier transform along the *f*-axis, we obtain:

$$\mathrm{P}(x,z,t=0) = \int\int |f|\,\Psi(p_x f, z=0, f)\; e^{j2\pi f\tau(p_x,x,z)}\, dp_x\, df. \tag{2.21}$$

Replacing p_x with $\frac{\sin\alpha}{\hat{v}}$ and using the trigonometric identity $\sin^2\alpha + \cos^2\alpha = 1$ reveals that

$$\tau(p_x, x\,, z) = \frac{x}{\hat{v}}\sin\alpha + \frac{z}{\hat{v}}\cos\alpha \ , \tag{2.22}$$

which can be interpreted as the travel time of an upgoing α-angled ERM wavefront from point (0, *z*) to point (*x*, 0). To simplify equation (2.21), let $\Phi(x, z = 0, f)$ denote the temporal Fourier transform of $\mathrm{P}(x, z = 0, t)$ measured at the surface:

$$\Phi(x, z = 0, f) = \int \ \mathrm{P}(x, z = 0, t)\ e^{-j2\pi f t} dt \ , \tag{2.23}$$

from which we can compute $|f|\ \Psi(p_x f, z = 0, f)$ as follows:

$$|f|\ \Psi(p_x f, z = 0, f) = |f|\ \int \ \Phi(x, z = 0, f)\ e^{-j2\pi f p_x x} dx \ . \tag{2.24}$$

Next, let $\widehat{\Phi}(p_x, z = 0, t)$ denote the inverse Fourier transform of $|f|\ \Psi(p_x f, z = 0, f)$ along the *f*-axis, i.e.,

$$\widehat{\Phi}(p_x, z = 0, t) = \int \ |f|\ \Psi(p_x f, z = 0, f)\ e^{j2\pi f t} df \ , \tag{2.25}$$

which leads to the following expression for $\mathrm{P}(x, z, t = 0)$, restricted to the region $\hat{v}^2 p_x^2 < 1$ to avoid the inclusion of evanescent waves:

$$\mathrm{P}(x, z, t = 0) = \int_{\hat{v}^2 p_x^2 < 1} \widehat{\Phi}\left(p_x, z = 0, \tau(p_x, x\,, z) = \ p_x x + \frac{z}{\hat{v}}\sqrt{1 - \hat{v}^2 p_x^2}\right) dp_x \ . \tag{2.26}$$

Fixing x and z makes $\tau(p_x, x, z)$ a function of p_x only, which allows us to compute $\mathrm{P}(x, z, t = 0)$ by integrating $\widehat{\Phi}\big(p_x, z = 0, \tau(p_x, x, z)\big)$ over p_x (slant-stacking), in accordance with equation (2.26).

2.7 Phase-Shift Migration

As mentioned previously, Stolt's migration is among the fastest migration methods; however, it cannot handle variations in the speed of sound. To correct for velocity changes along the vertical axis, Gazdag introduced a method known as phase shift migration [24]. The following section provides pertinent background on this method based on references [24, 92]. The algorithm begins by transforming the recorded data $\mathrm{P}(x, z = 0, t)$ into $\Psi(k_x, z = 0, f)$ by using the two-dimensional Fourier transform. Next, we consider equation (2.10) from section 2.5, which is rewritten here for convenience:

$$\frac{\partial^2}{\partial z^2}\Psi(k_x, z, f) + 4\pi^2 k_z^2 \Psi(k_x, z, f) = 0 \ .$$

Assuming that $\hat{v}_z$ does not change within a propagation medium layer extending from z to $z+\Delta z$, we have the following solution of equation (2.10):

$$\Psi(k_x, z + \Delta z, f) = \Psi(k_x, z, f)\ e^{j2\pi k_z \Delta z} \ , \tag{2.27}$$

where Δz is the discretization step along the z-axis, and k_z is given by $k_z = \frac{f}{\hat{v}_z}\sqrt{1 - \frac{\hat{v}_z{}^2 k_x^2}{f^2}}$ subject to $f^2 > \hat{v}_z{}^2 k_x^2$, which effectively excludes the evanescent wavefield region and requires that $f \neq 0$ to avoid singularities. Note that $\Delta z > 0$ is positive, and the sign of k_z coincides with the sign of f, which means that equation (2.27) describes the downward wavefield continuation process. Equation (2.27) lets us compute $\Psi(k_x, z + \Delta z, f)$ from $\Psi(k_x, z = 0, f)$ by applying appropriate phase shifts iteratively. Thus,

$$\mathrm{P}(x, z + \Delta z, t = 0) = \iint_{f^2 > \hat{v}_z{}^2 k_x^2} \left(\Psi(k_x, z, f)\ e^{j2\pi k_z \Delta z}\right) e^{j2\pi k_x x}\, dk_x df\ . \qquad (2.28)$$

In other words, finding $\mathrm{P}(x, z + \Delta z, t = 0)$ takes three steps: first, determine k_z and multiply $\Psi(k_x, z, f)$ (which represents the wavefield in the previous layer) by $e^{j2\pi k_z \Delta z}$ (extrapolation operator) , then apply the inverse Fourier transform with respect to k_x, and finally, integrate over all the temporal frequencies f. Alternatively, one can integrate the product $\Psi(k_x, z, f)\ e^{j2\pi k_z \Delta z}$ over the f-axis first, i.e., before applying the inverse Fourier transform along the k_x-axis. In the special case of constant $\hat{v}_z = \hat{v} = \frac{c}{2}$ throughout the entire propagation medium, equation (2.28) can be simplified as follows:

$$\mathrm{P}(x, z, t = 0)|_{\hat{v}_z = \hat{v} = \frac{c}{2}} = \iint_{f^2 > \hat{v}^2 k_x^2} \Psi(k_x, z = 0, f) e^{j2\pi\left(k_x x + \frac{f}{\hat{v}}\sqrt{1 - \frac{\hat{v}^2 k_x^2}{f^2}}\right)} dk_x df\ . \qquad (2.29)$$

Chapter 3

Constant-Velocity Migration for Plane-Wave Ultrasound Imaging

3.1 Introduction

In the following, we will present two novel methods that are suitable for constant-velocity plane-wave ultrasound image reconstruction. Our proposed algorithms rely on a modelling approach that incorporates the following features: homogeneous two-dimensional scalar wave equation, zero-offset ERM setting, and reflector "explosion" time adjustments. This approach is advantageous due to its effectiveness in adapting well-known seismic data processing techniques to plane-wave ultrasound imaging. In this chapter, we take classic Stolt's and slant-stack migration methods as an example and develop their modified versions for plane-wave image reconstruction. Our modelling approach, however, is applicable to other techniques, such as phase-shift migration [24] that takes into account depth-dependent velocity variations, which will be presented in Chapter 5.

3.2 Proposed Method

The classic migration algorithms described in Chapter 2 work in the zero-offset setting, which means that location (x, 0) of a receiver at the surface is the same as that of a transmitter, while a reflector located at (x, z) "explodes" at time $t = 0$. In other words, point source emissions from the transmitter cause the reflector to "explode" after a certain downward propagation delay (from the transmitter to the reflector), but this delay is discarded and instead, the upward propagation velocity (from the reflector to the receiver) is assumed to be $\hat{v} = \frac{c}{2}$. These algorithms cannot be applied directly to plane-wave imaging without appropriate modifications.

To handle the case of plane-wave emissions at zero angle we shall modify the dispersion equation $k_z = \frac{f}{\hat{v}}\sqrt{1 - \frac{\hat{v}^2 k_x^2}{f^2}}$ by setting $\hat{v} = c$ and then multiplying $\Psi(k_x, z = 0, f)$ by $e^{j2\pi f\frac{z}{c}}$ to compensate for overmigration of the reflectors locations along the z-axis caused by setting $\hat{v} = c$. Essentially, for a horizontal plane wave (i.e., a plane wave traveling at a zero angle) the "explosion" time of any reflector located at depth z is delayed by $\frac{z}{c}$. On the other hand, for the non-zero plane-wave emission angle $\theta \neq 0$, as shown in Figure 3.1, the apparent reflector locations at (x_1, z_1) and (x_2, z_2) must be corrected to $(x_1, \hat{z}_1)$ and $(x_1, \hat{z}_2)$, respectively, based on the following travel-time relationships. For a reflector located on the left hand side with respect to the z-axis, one has:

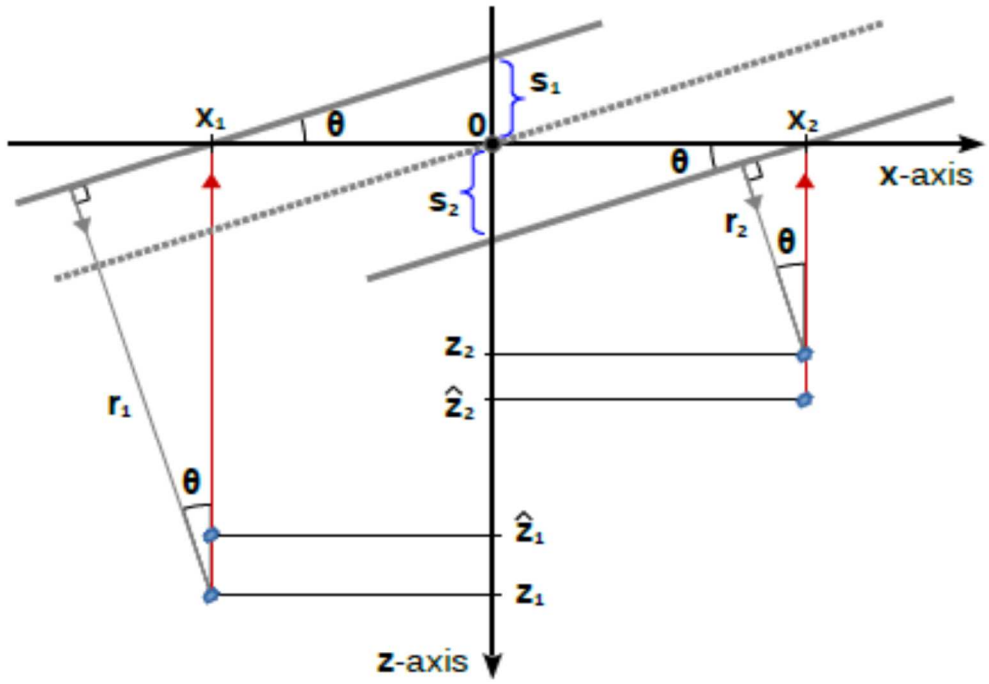

Figure 3.1: Exploding reflector depth corrections for plane-wave zero-offset migration [1].

$$\frac{2\hat{z}_1}{c} = \frac{r_1}{c} + \frac{z_1 - |\, s_1|}{c}, \tag{3.1}$$

where $r_1 = z_1 \cos\theta$ and $s_1 = x_1 \tan\theta$. Thus,

$$\hat{z}_1 = z_1 \frac{1+\cos\theta}{2} + |\, x_1| \frac{\tan\theta}{2}, \tag{3.2}$$

In a similar manner, for a reflector located on the right hand side with respect to the *z*-axis, one has:

$$\frac{2\hat{z}_2}{c} = \frac{r_2}{c} + \frac{z_2 + s_2}{c} \quad , \tag{3.3}$$

where $r_2 = z_2 \cos\theta$ and $s_2 = x_2 \tan\theta$. Thus,

$$\hat{z}_2 = z_2 \frac{1+\cos\theta}{2} + x_2 \frac{\tan\theta}{2} \, . \tag{3.4}$$

The *z*-axis shifts $|s_1|$ and s_2 account for the travel distance differences between the actual plane-wave emission (centered at $x = 0$) and the zero-offset wavefronts associated with the transmitter locations $(x_1, 0)$ and $(x_2, 0)$, respectively. For $\theta > 0$ (shown in Figure 3.1), $z_1$is corrected upward to $\hat{z}_1$ (negative x_2), while z_2 is corrected downward to $\hat{z}_2$ (positive x_1). For $\theta < 0$, its sine becomes negative, and the correcting directions are reversed. Note that such corrections are dependent on the reflector's *x*-coordinate whenever $\theta \neq 0$.

3.3 Plane-Wave Stolt's Migration

Setting $\hat{v} = c$ and multiplying $\Psi(k_x, 0, f)$ by $e^{j2\pi f\frac{z}{c}}$ in equation (2.13) yields the following result for the special case of zero-angle plane-wave emissions (i.e., $\theta = 0$):

$$P(x, z, 0) = \iint_{f^2 > c^2 k_x^2} \Psi(k_x, z = 0, f) e^{j2\pi(k_x x + k_z z + f\frac{z}{c})} dk_x df \, , \tag{3.5}$$

where k_z is given by

$$k_z = \frac{f}{c}\sqrt{1-(\frac{ck_x}{f})^2}\,. \tag{3.6}$$

Let us introduce a new variable $\hat{k}_z$:

$$\hat{k}_z = \frac{f}{c} + k_z = \frac{f}{c}\left[\;1+\sqrt{1-\left(\frac{ck_x}{f}\right)^2}\;\right], \tag{3.7}$$

which is subject to the condition $f^2 > c^2k_x^2$ implying $\hat{k}_z^2 > k_x^2$ and $\hat{k}_z \neq 0$. After plugging equation (3.7) into equation (3.5), we get the following result:

$$P(x,z,0) = \iint_{f^2>c^2k_x^2} \Psi(k_x,z,f)e^{j2\pi(k_xx+\hat{k}_zz)}dk_xdf\,. \tag{3.8}$$

The above equation represents the migrated image for the transmission angle $\theta = 0$, and it is computationally demanding. Similar to Stolt's approach, our next step is to change the integration variable f to $\hat{k}_z$ to enable the use of the Fourier transform. From equation (3.6), we have

$$f = \frac{c\hat{k}_z}{2}\left[\;1+\left(\frac{k_x}{\hat{k}_z}\right)^2\;\right], \tag{3.9}$$

whose first derivative with respect to the wavenumber $\hat{k}_z$ is as follows:

$$\frac{df}{d\hat{k}_z} = \frac{c}{2}\left[\ 1 - \left(\frac{k_x}{\hat{k}_z}\right)^2\ \right]. \tag{3.10}$$

Upon substituting equations (3.9) and (3.10) into equation (3.8), we can express the final migrated image in terms of the interpolated spectrum $\widehat{\Psi}(k_x, 0\ , \hat{k}_z)$ for $\hat{k}_z^2 > k_x^2$ as

$$P(x, z, 0) = \iint_{\hat{k}_z^2 > k_x^2} \widehat{\Psi}\left(k_x, 0\ , \hat{k}_z\right) e^{j2\pi(k_x x + \hat{k}_z z)} dk_x d\hat{k}_z\ , \tag{3.11}$$

where

$$\widehat{\Psi}\left(k_x, 0\ , \hat{k}_z\right) = \frac{c}{2}\left[\ 1 - \left(\frac{k_x}{\hat{k}_z}\right)^2\ \right] \Psi\left(k_x, 0\ , \frac{c\hat{k}_z}{2}\left[\ 1 + \left(\frac{k_x}{\hat{k}_z}\right)^2\ \right]\right). \tag{3.12}$$

Thus, to get the migrated spectrum $\widehat{\Psi}\left(k_x, 0\ , \hat{k}_z\right)$ for $\hat{k}_z^2 > k_x^2$ from the spectrum of the recorded data $\Psi(k_x, 0, f)$, we need to perform one-dimensional interpolation along the *f*-axis and then scale the resulting spectrum using equation (3.12). As for the remaining values of $\hat{k}_z$, i.e., those satisfying $\hat{k}_z^2 \leq k_x^2$, we set $\widehat{\Psi}\left(k_x, 0\ , \hat{k}_z\right)$ to zero.

To handle transmission at any angle $\theta\ \neq 0$, a coordinate transformation $\mathrm{P}(x, z, 0) \mapsto \mathrm{P}_\theta(x, \hat{z}, 0)$ needs to be performed. The transformed $\hat{z}$-axis is obtained from the original *z*-

axis using the following formula:

$$\hat{z} = z^* + x\frac{\tan\theta}{2} \text{ , where } z^* = z\frac{1+\cos\theta}{2}. \tag{3.13}$$

In other words, the z-axis undergoes compression by the factor $\frac{1+\cos\theta}{2}$, which yields an intermediate z^*-axis, followed by the vertical shift $x\frac{\tan\theta}{2}$ upward or downward, depending on the signs of x and θ (see Figure 3.1). Using the scaling property of the Fourier transform, one arrives at

$$\widehat{\Psi}_\theta\left(k_x, 0\,, \hat{k}_z\right) = \frac{c}{1+\cos\theta}\left[\ 1 - \left(\frac{k_x}{\hat{k}_z}\right)^2\ \right]\Psi\left(k_x, 0\,, \frac{c\hat{k}_z}{1+\cos\theta}\left[\ 1 + \left(\frac{k_x}{\hat{k}_z}\right)^2\ \right]\right)\ . \tag{3.14}$$

Note that when the plane-wave emission angle θ in equation (3.14) is set to zero, it becomes the same as equation (3.12).

After computing the interpolated and scaled spectrum according to equation (3.14), we apply the two-dimensional inverse Fourier transform to $\widehat{\Psi}_\theta\left(k_x, 0\,, \hat{k}_z\right)$ to obtain the following result:

$$P_\theta(x, z^*, 0) = \iint_{\hat{k}_z^2 > k_x^2} \widehat{\Psi}_\theta\left(k_x, 0\,, \hat{k}_z\right) e^{j2\pi(k_x x + \hat{k}_z z)} dk_x d\hat{k}_z\ , \tag{3.15}$$

where $P_\theta(x, z^*, 0)$ is the migrated image in the (x, z^*) domain. The final image $\mathrm{P}(x, \hat{z}, 0)$ can be computed as $P_\theta\left(x, z^* + x\frac{\tan\theta}{2}, 0\right)$ via interpolation along the z*-axis. Alternatively, the desired shift along the z*-axis can be produced by multiplying the $(x, \hat{k}_z)$ domain data by $e^{j\pi\hat{k}_z x \tan\theta}$. In summary, our proposed plane-wave Stolt's method consists of the following steps.

Step 1: Compute $\Psi(k_x, 0, f)$ by applying the Fourier transform to $P(x, 0, t)$. Set $\Psi(k_x, 0, f)$ to zero whenever $f^2 \leq c^2 k_x^2$.

Step 2: For each k_x, obtain $\widehat{\Psi}_\theta\left(k_x, 0\,, \hat{k}_z\right)$ from $\Psi(k_x, 0, f)$ via interpolation along the f-axis and amplitude scaling, as per equation (3.14). Set $\widehat{\Psi}_\theta\left(k_x, 0\,, \hat{k}_z\right)$ to zero whenever $\hat{k}_z^2 \leq k_x^2$.

Step 3: Apply the inverse Fourier transform to $\widehat{\Psi}_\theta\left(k_x, 0\,, \hat{k}_z\right)$ along the k_x-axis.

Step 4: Multiply the previous result by $e^{j\pi\hat{k}_z x \tan\theta}$ and then apply the inverse Fourier transform along the $\hat{k}_z$-axis, thus obtaining final $\mathrm{P}(x, \hat{z}, 0)$.

3.4 Plane-Wave Slant-Stack Migration

Figure 3.2 illustrates a plane wave emitted at an angle θ. The recorded wavefield is decomposed into a set of upgoing plane waves as well, each having a specific slant angle α corresponding to a specific slant parameter

$$p_x = \frac{\sin\alpha}{c}\,. \tag{3.16}$$

To put it simply, when transmitting at an angle θ, the received data is synthetically steered at different α angles, i.e., along different p_x-parameter "slopes" measured with respect to the vertical axis [14], and the resulting steered "slanted" traces are summed, or "stacked". Essentially, a two-dimensional function, which is the received data acquired in the (x, t)-domain, is projected onto a one-dimensional $p_x = k_x/f$ domain. This is also known as the forward Radon transform [14, 25].

We start by letting $\hat{v} = c$ and substituting $k_z = \frac{f}{c}\sqrt{1-(\frac{ck_x}{f})^2}$ with $\hat{k}_z$, in accordance with equation (3.7), rewritten here for convenience:

$$\hat{k}_z = \frac{f}{c} + k_z = \frac{f}{c}\left[\ 1 + \sqrt{1-\left(\frac{ck_x}{f}\right)^2}\ \right]. \tag{3.17}$$

Next, we fix

$$k_x = f p_x = f \frac{\sin \alpha}{c}, \tag{3.18}$$

where $p_x = \frac{\sin \alpha}{c}$ is a specific slant value corresponding to a specific α-angled upgoing ERM wavefront. By substituting equation (3.18) into equation (3.17) we obtain

$$\hat{k}_z = \frac{f}{c} + k_z = \frac{f}{c}\left[\ 1 + \sqrt{1 - c^2 p_x^2}\ \right], \tag{3.19}$$

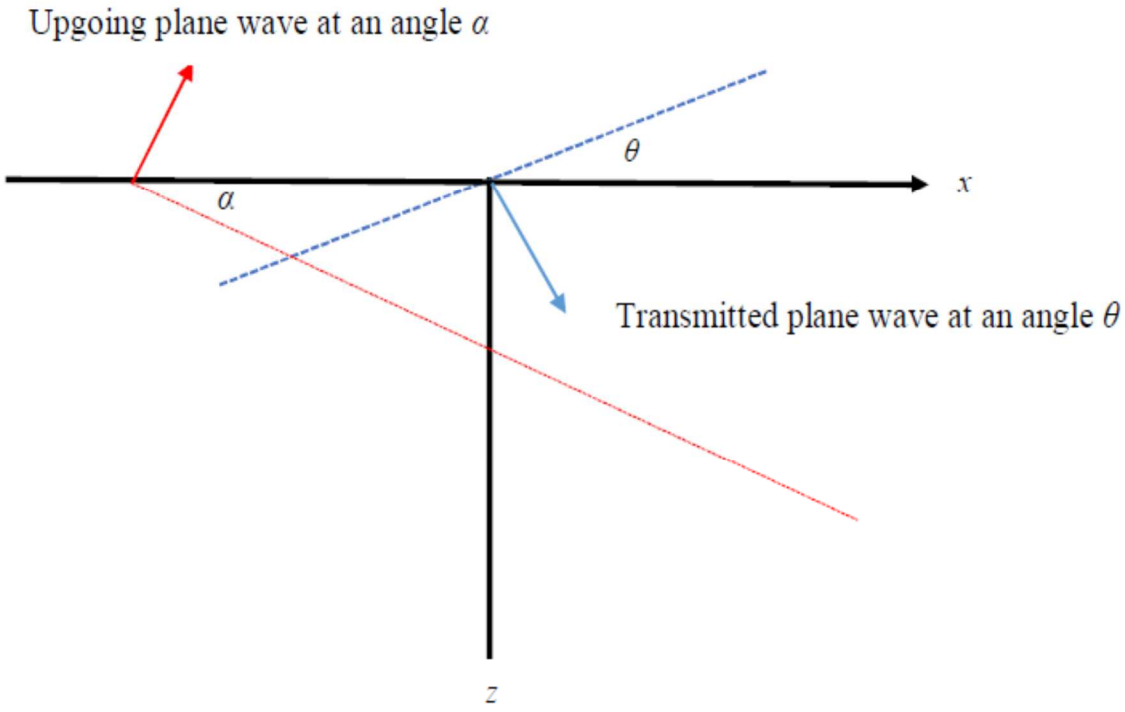

Figure 3.2: Illustration of the image construction using slant-stack migration.

subject to $c^2p_x^2 < 1$. Consequently, after substituting equations (3.18) and (3.19) into equation (3.8) from the previous section, we get the following result for $\theta = 0$:

$$P(x,z,0) = \iint_{c^2p_x^2<1} |f|\Psi(fp_x,0,f)e^{j2\pi\frac{f}{c}\left(cp_xx+\left[\ 1+\sqrt{1-c^2p_x^2}\right]z\right)}dp_xdf \ . \tag{3.20}$$

Note that the argument of the exponential function $e^{j2\pi\frac{f}{c}\left(cp_xx+\left[\ 1+\sqrt{1-c^2p_x^2}\right]z\right)}$ contains the time delay

$$\hat{\tau}(p_x\ ,x\ ,z) = p_xx + \frac{z}{c}\left[\ 1+\sqrt{1-c^2p_x^2}\ \right]. \tag{3.21}$$

Alternatively, equation (3.21) can be reformulated as

$$\hat{\tau}(\alpha\ ,x\ ,z) = \frac{\sin\alpha}{c}x + \frac{z}{c}\left[\ 1+\cos\alpha\right]. \tag{3.22}$$

Equations (3.21) and (3.22) represent the time delay needed to migrate events to their proper positions when $\theta = 0$. Thus,

$$P(x,z,0) = \iint_{c^2p_x^2<1} |f|\Psi(fp_x,0,f)e^{j2\pi f\hat{\tau}(p_x\ ,x\ ,z)}dp_xdf \ . \tag{3.23}$$

By applying the inverse Fourier transform with respect to the temporal frequency axis, we obtain

$$\mathrm{P}(x,z,0) = \int_{c^2 p_x^2 < 1} \widehat{\Phi}(p_x, 0\,, t = \hat{\tau}(p_x\,, x\,, z))dp_x\,, \tag{3.24}$$

where

$$\widehat{\Phi}(p_x, 0\,, t) = \int |f|\Psi(fp_x, 0, f)\, e^{j2\pi f t}\, df.$$

Alternatively, one can view $\widehat{\Phi}\big(p_x, 0\,, t = \hat{\tau}(p_x\,, x\,, z)\big)$ as

$$\rho(t) * \int \Phi(x, 0\,, t = \hat{\tau}(p_x\,, x\,, z))dx,$$

where $\rho(t) = \int |f| e^{j2\pi f t} df$ is known as the ideal rho filter.

Equation (3.24) shows that, in order to get the final migrated image $\mathrm{P}(x, z, 0)$ from the "trace" $\widehat{\Phi}(p_x, 0\,, t)$ steered along a slant parameter p_x, one needs to calculate the delay $\hat{\tau}(p_x\,, x\,, z)$, pick the corresponding point $\widehat{\Phi}(p_x, 0\,, t)$ along the *t*-axis, and accumulate such points over all slants p_x.

To handle plane-wave emissions at $\theta \neq 0$, one needs to transform $P(x, z, 0)$ into $P_\theta(x, \hat{z}, 0)$, where $\hat{z} = z^* + x\frac{\tan\theta}{2}$ and $z^* = z\frac{1+\cos\theta}{2}$ as expressed in equation (3.13) in the previous section. That is,

$$P_\theta(x, z^*, 0) = \int_{c^2 p_x^2 < 1} \widehat{\Phi}_\theta(p_x, 0\,, t = \hat{\tau}_\theta(p_x\,, x\,, z \mapsto z^*))dp_x\,, \tag{3.25}$$

where

$$\hat{\tau}_\theta(p_x\,, x\,, z^*) = p_x x + z\frac{1+\cos\theta}{2c}\left[\ 1 + \sqrt{1 - c^2 p_x^2}\ \right]. \tag{3.26}$$

Equation (3.25) is a generalization of equation (2.24): we first interpolate $\widehat{\Phi}(p_x, 0\,, t)$ along the *t*-axis at positions specified by $\hat{\tau}_\theta$ for a fixed pair of values (p_x, x) and then sum over p_x to produce $P_\theta(x, z^*, 0)$. Our final result $P_\theta\left(x, z^* + x\frac{\tan\theta}{2}, 0\right)$ can be obtained from $P_\theta(x, z^*, 0)$ via interpolation along the z^*-axis.

In summary, our proposed plane-wave slant-stack migration method consists of the following steps.

Step 1: Compute $\Phi(x, 0, f)$ by applying the Fourier transform to $P(x, 0, t)$ along the *t*-axis. Select a range of p_x values such that $c^2 p_x^2 < 1$. Initialize $P_\theta(x, z^*, 0)$ to zeros.

Step 2: For each p_x, perform the following computations:

Step 2a: Multiply $\Phi(x, 0, f)$ by $e^{-j2\pi f p_x x}$ and then sum over x. Multiply the result by $|f|$, which yields $|f|\Psi(fp_x, 0, f)$.

Step 2b: Compute $\widehat{\Phi}(x, 0, t)$ by applying the inverse Fourier transform to $|f|\Psi(fp_x, 0, f)$ along the f-axis.

Step 2c: For each x, find $\hat{\tau}_\theta$ using equation (3.26) determine $\widehat{\Phi}(p_x, 0, \hat{\tau}_\theta)$ via interpolation, and then add it to $P_\theta(x, z^*, 0)$, as per equation (3.25).

Step 3: For each x, obtain final $P_\theta(x, \hat{z}, 0)$ from $P_\theta(x, z^*, 0)$ via interpolation along the z^*-axis, according to the formula $\hat{z} = z^* + x\frac{\tan\theta}{2}$.

3.5 Comparison to Other Fourier-Domain Methods

Several reconstruction techniques have been proposed in the last few years in the field of biomedical ultrasound imaging that are based on the Fourier transform: Lu's method, Garcia's method, and Fourier-slice-based method [8, 11, 21]. Next, we provide qualitative comparisons of our proposed methods to these three existing Fourier-domain techniques.

Garcia *et al*. [21] have reported an alternative modification of Stolt's method. They account for plane-wave emissions by fitting the ERM velocity model to

$$\hat{v} = \frac{c}{\sqrt{1+\cos\theta+\sin^2\theta}} \tag{3.27}$$

and using the following mapping formula

$$(k_x, k_z) = \left(k_x, \frac{\sqrt{k_x^2+k_z^2 S^2}}{\sqrt{1+\cos\theta+\sin^2\theta}} \right), \tag{3.28}$$

where $S = \frac{1+\cos\theta+\sin^2\theta}{(1+\cos\theta)^{\frac{3}{2}}}$.

In our case, we employ a completely different remapping formula given by equation (3.14), while letting $\hat{v} = c$. Other modifications introduced by Garcia *et al* [21] include multiplying the (*x*, *f*)-domain data by $e^{j2\pi f\frac{x}{c}\sin\theta}$ before migration, multiplying the (k_x, k_z)-domain data by $\frac{f}{k_z}$ during migration, and multiplying the (k_x, *z*)-domain data by $e^{j\frac{2\pi k_x \frac{z}{c}\sin\theta}{2-\cos\theta}}$ after migration. In our case, we multiply (k_x, $\hat{k}_z$)-domain data by our scaling factor $\frac{c}{1+\cos\theta}\left[\ 1-\left(\frac{k_x}{\hat{k}_z}\right)^2\ \right]$ during migration and multiply the (*x*, $\hat{k}_z$)-domain data by $e^{j\pi\hat{k}_z x\tan\theta}$ after migration. The key difference between Garcia's approach and ours is that

the former relies on approximating plane-wave travel time hyperbolas to those arising from synthetic-aperture ERM assumptions (see [21] for details), whereas the latter adjusts "explosion" time of reflectors.

Lu's method [11], which is based on the theory of limited-diffraction beams, models two-way scalar wave propagation in a weakly attenuating medium, where scattering is dominated by reflections. In the case of steered plane-wave imaging, the (k_x, f)-domain data is interpolated along the f-axis using the formula

$$f = \frac{c\sqrt{k_x^2+k_z^2}}{2k_x \sin\theta + 2k_z \cos\theta} \quad . \tag{3.29}$$

Prior to such frequency remapping, the (x, f)-domain data is multiplied by $e^{j2\pi f\frac{x}{c}\sin\theta}$ to account for plane-wave steering delays (as in Garcia's method). Note that for $\theta = 0$, Lu's f-to-k_z remapping formula becomes $\frac{c\sqrt{k_x^2+k_z^2}}{2k_z}$, which is equivalent to our f-to-$\hat{k}_z$ remapping equation (3.14), except for the amplitude scaling factor of $\frac{c}{2}\left[\ 1-\left(\frac{k_x}{\hat{k}_z}\right)^2\ \right]$. However, for $\theta \neq 0$, the remapping formula used by Lu's method is different from equation (3.14) used by our Stolt's method. Another important difference is that pointwise multiplications of the $(x,\ f)$ domain data by $e^{j2\pi f\frac{x}{c}\sin\theta}$ before remapping (Lu's method) are discarded; instead, our Stolt's method multiplies the $(x,\ \hat{k}_z)$-domain data by $e^{j\pi\hat{k}_z x\tan\theta}$ after remapping.

Ultrasound Fourier-slice beamforming (UFSB), which has been proposed by Bernard *et al.* [8], is based on the Fourier-slice theorem and studied in [9] in the context of sparse reconstruction. It operates on the (k, α)-domain data, where $k = \frac{f}{c}$ and $\alpha = \sin^{-1}\frac{k_x}{k}$. The data along the k-axis is interpolated using the remapping formula

$$k = \frac{c\sqrt{k_x^2+k_z^2}}{2k_x \sin\theta + 2k_z \cos\theta} \ , \tag{3.30}$$

which is the same as in Lu's method, while the data along the α-axis is interpolated according to the following equation:

$$\alpha = \tan^{-1}\left(\frac{2k_x k_z \cos\theta + (k_x^2 - k_z^2)\sin\theta}{2k_x k_z \sin\theta + (k_x^2 - k_z^2)\cos\theta}\right) \ . \tag{3.31}$$

Before performing such two-dimensional interpolation, UFSB obtains its (k, α) domain data in the same way our slant-stack migration method obtains $\Psi(fp_x, 0, f)$. In our case, we first compute $\Phi(x, 0, f)$ by applying the Fourier transform to $P(x, 0, t)$, and then for each p_x value, we integrate $\Phi(x, 0, f)e^{-j2\pi f p_x x}$ over the x-axis. In the UFSB case, after computing $\Phi(x, 0, f)$, the (k, α) domain data is obtained for each α by integrating the $\Phi(x, 0, f)e^{-j2\pi x k \sin\alpha}$ over the x-axis too. Interpreting p_x as $\frac{\sin\alpha}{c}$ leads to $fp_x = k\sin\alpha$, which means that $\Phi(x, 0, f)$ is multiplied by the same exponential factor in both cases. In other words, our $\Psi(fp_x, 0, f)$ contains the same information as the (k, α) domain data used

by UFSB. The interpolation step itself, however, is completely different in our slant-stack migration method: it uses the remapping formula given by equation (3.26), which is applied to $\widehat{\Phi}(x, 0, t)$ along the t-axis and followed by integration over the p_x-axis.

To summarize, UFSB, Lu's, Garcia's, and our proposed methods are different from one another in at least three steps out of the following four:

1) data preprocessing before spectral remapping,
2) Fourier-domain interpolation,
3) Fourier-domain amplitude rescaling,
4) data postprocessing after remapping.

From the analytical viewpoint, it is difficult to say which method would produce superior images. In fact, Chapter 4 (where each method's performance is evaluated in terms of image contrast, resolution, and similarity metrics) suggests that no single method reliably outperforms the others in all cases. In other words, all Fourier-domain techniques have their own merits and limitations, and the choice of a particular method ultimately rests with the user. Nevertheless, we should point out that our proposed methods have outperformed the other Fourier-domain techniques in the majority of cases presented in Chapter 4. Also, in comparison to DAS beamforming, our Stolt's method is considerably less expensive in terms of its computational complexity, as are Lu's and Garcia's methods.

Chapter 4

Plane-Wave Constant-Velocity Migration: Evaluation Results

4.1 Introduction

To assess our proposed plane-wave Stolt's and slant-stack migration methods, we have used the *in-vitro* PICMUS RF data [17], acquired with a Verasonics Vantage research system [89] on the CIRS Ultrasound Phantom Model 040GSE [13], as described by Liebgott *et al*. [48]. The plane-wave emission angles ranged from -16° to +16°. For each angle θ, the corresponding data frame was of size 128 ×3328, obtained from n_x = 128 transducer elements (0.30-mm pitch) sampled n_t = 3328 times at 20.832 MHz, after emitting a 5.208-MHz ultrasound plane wave (2.5 cycles, 67% pulse bandwidth). The reconstructed images here correspond to the following three scenarios:

1) using a single plane wave emitted at $\theta = 0°$,
2) using 11 plane waves emitted at $\theta = \pm16°, \pm13°, \pm9.5°, \pm6.5°, \pm3°, 0°$,
3) using all 75 emitted plane waves.

The image quality is evaluated based on the following numerical indicators [48]:

1) Contrast to noise ratio (CNR, reported in dB), obtained for two cyst phantoms (anechoic cylinder targets), shown in Figure 4.1 (top) and referred to as *X* and *Y*.
2) Full width at half-maximum (FWHM, reported in mm), obtained for seven point phantoms (100-micron wire targets), shown in Figure 4.1 (bottom) and referred to as *A*, *B*, *C*, *D*, *E* (five vertically aligned points from top to bottom), *F* (leftmost point), and *G* (rightmost point).

Figure 4.1 mentioned above shows the cyst and point phantom images reconstructed by a basic DAS beamformer (with no receive apodization) using all 75 plane-wave emissions. Tables 4.3 and 4.4 in Sections 4.4 and 4.5 compare the corresponding CNR and FWHM values obtained by the Fourier-domain methods under consideration.

Additionally, we present the carotid artery images (longitudinal and cross-section views) reconstructed from the *in-vivo* PICMUS RF data (128×1536 frame size) [17]. Figure 4.2 shows the DAS-beamformed image using Hamming receive apodization for the case of 75 plane-wave emissions, which we shall use as a reference for evaluation purposes. Our goal is to quantify the similarity between the two-dimensional compounded, normalized, and log-compressed envelope of the DAS-beamformed data (using all 75 plane-wave emissions) and those produced by individual Fourier-domain methods using only 11 plane-wave emissions. We have chosen the structural similarity index [91] and mean-squared error as our evaluation metrics.

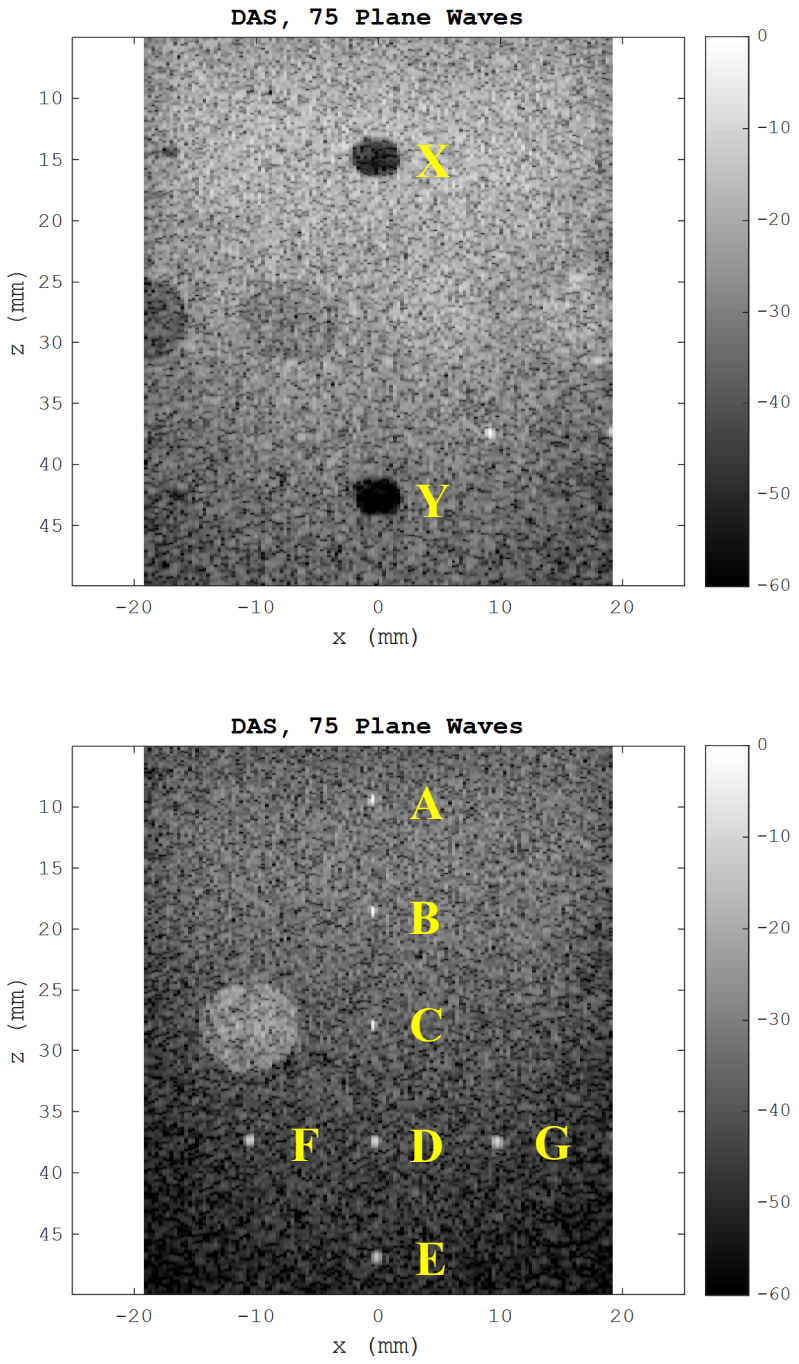

Figure 4.1: Two anechoic cyst phantoms (top) and seven point phantoms (bottom), 75 plane-wave emissions, basic DAS beamforming [17].

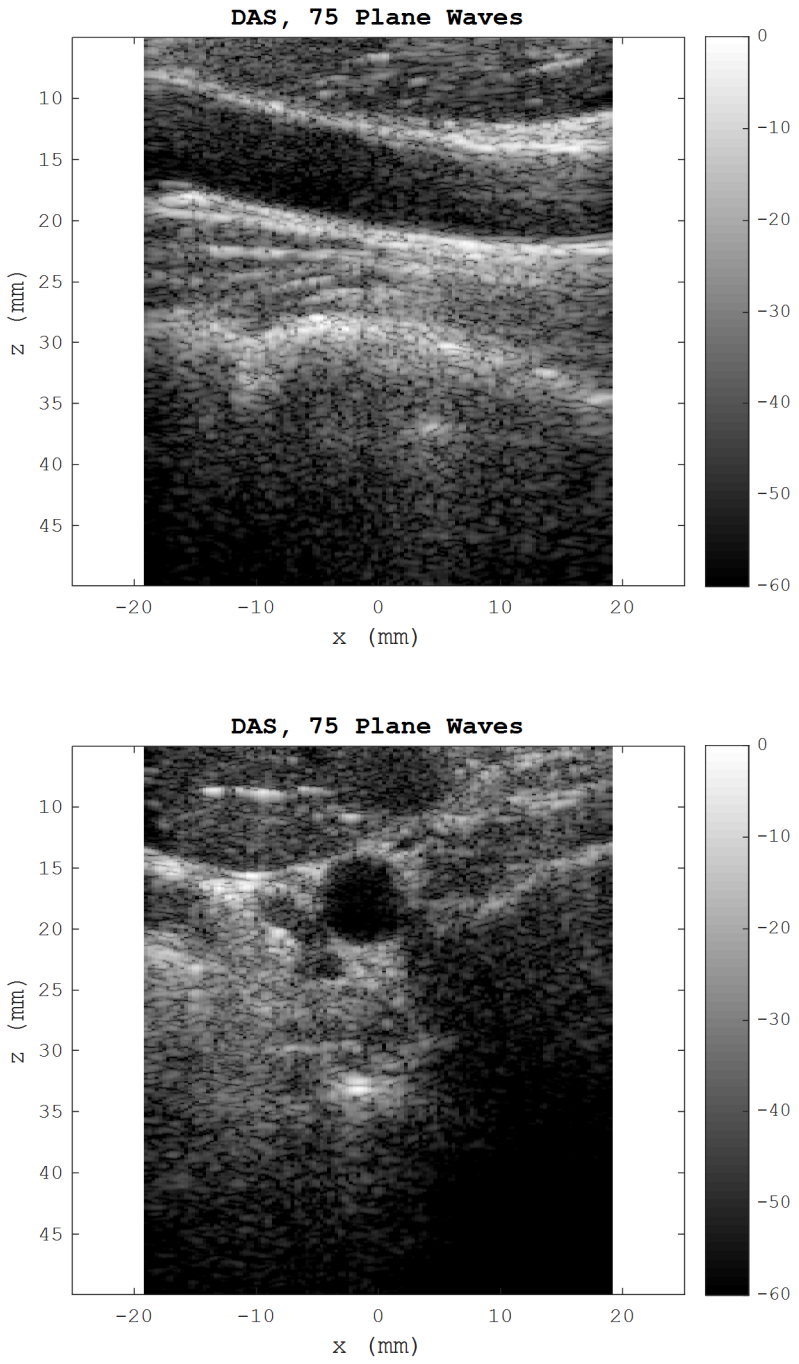

Figure 4.2: Carotid artery, longitudinal (top) and cross (bottom) sections, 75 plane-wave emissions, DAS-Hamming beamforming [17].

4.2 Implementation Details

To ensure reproducible image reconstruction results involving UFSB, Garcia's, and Lu's methods mentioned in Chapter 3, we have used their publicly available implementations from a GITLAB repository [9]. We have not altered them in any way, except for the initial time offset correction (when applicable) to account for the plane wave positioning at the center of the transducer.

In all three implementations, default four-fold zero-padding was used for horizontal (spatial) x-axis and vertical (temporal) t-axis (to avoid FFT wraparound artifacts), which produced the Fourier-domain grids of size 512 ×13312 during *in-vitro* data processing and 512×6144 during *in-vivo* data processing. In our case, the Fourier-domain grid size was 256×4096. All implementations, including ours, employed linear interpolation during remapping, without any filtering or other enhancements [50]. As an illustrative example, Figures 4.3 and 4.4 show the compounded images reconstructed by Lu's method in the case of 11 plane-wave emissions.

For UFSB, we have experimented with several α parameter ranges: $\pm 20^{\circ}$, $\pm 30^{\circ}$, $\pm 40^{\circ}$, $\pm 50^{\circ}$ (default), $\pm 60^{\circ}$, and $\pm 70^{\circ}$, using two selections for $\Delta\alpha$ spacing: either 1/200 (default), or 1/400 of the corresponding α range. Among the resulting twelve configurations, we have chosen the following three best performers (in terms of their CNR and/or FWHM values) for comparison purposes:

a) $\alpha \in [-20, 20]^{o}$ with $\Delta\alpha = 0.2^{o}$ (201 angular samples),

b) $\alpha \in [-30, 30]^{o}$ with $\Delta\alpha = 0.3^{o}$ (201angular samples),

c) $\alpha \in [-40, 40]^{o}$ with $\Delta\alpha = 0.2^{o}$ (401 angular samples).

We refer to these three versions as UFSB$^{\mathbf{a}}$, UFSB$^{\mathbf{b}}$, and UFSB$^{\mathbf{c}}$, respectively.

Similarly, for our plane-wave slant-stack migration (SSM) method, we report three implementations having the following configuration parameters:

a) $p_x \in [-1.79, 1.79] \times 10^{-4}$ s/m with $\Delta p_x = 3.58 \times 10^{-6}$ s/m (101 slant samples),

b) $p_x \in [-2.64, 2.64] \times 10^{-4}$ s/m with $\Delta p_x = 3.52 \times 10^{-6}$ s/m (151 slant samples),

c) $p_x \in [-3.44, 3.44] \times 10^{-4}$ s/m with $\Delta p_x = 3.44 \times 10^{-6}$ s/m (201 slant samples).

We refer to these three versions as SSM$^{\mathbf{a}}$, SSM$^{\mathbf{b}}$, and SSM$^{\mathbf{c}}$, respectively.

We also report the CNR and FWHM results obtained by the following DAS beamforming implementations [17]:

a) basic DAS with no apodization (e.g., see Figure 4.1),

b) DAS with Boxcar receive apodization using the default *F*-number of 1.75,

c) DAS with Hamming receive apodization using the default *F*-number of 1.75 (e.g., see Figure 4.2).

We refer to these three versions as DAS$^{\mathbf{a}}$, DAS$^{\mathbf{b}}$, and DAS$^{\mathbf{c}}$, respectively.

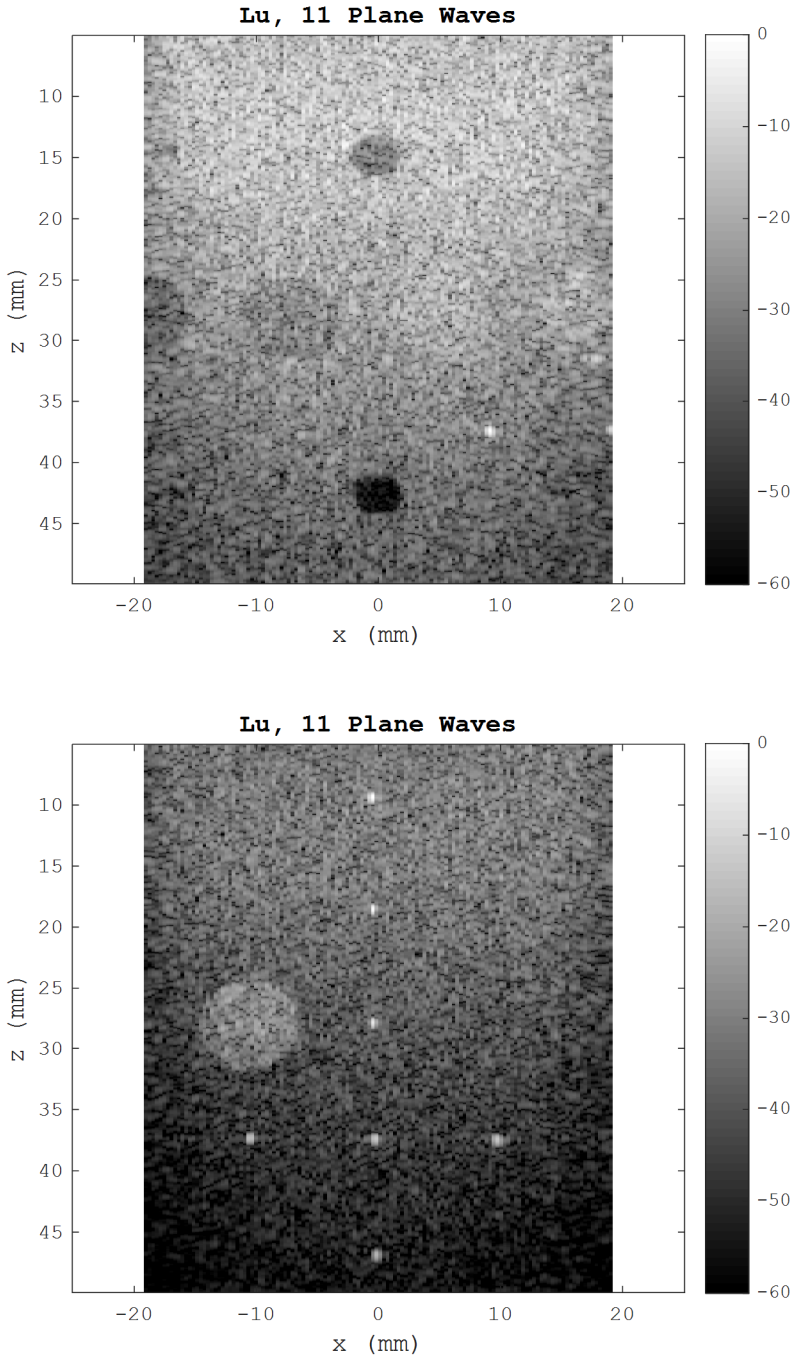

Figure 4.3: Two anechoic cyst phantoms (top) and seven point phantoms (bottom), 11 plane-wave emissions, Lu's method [11].

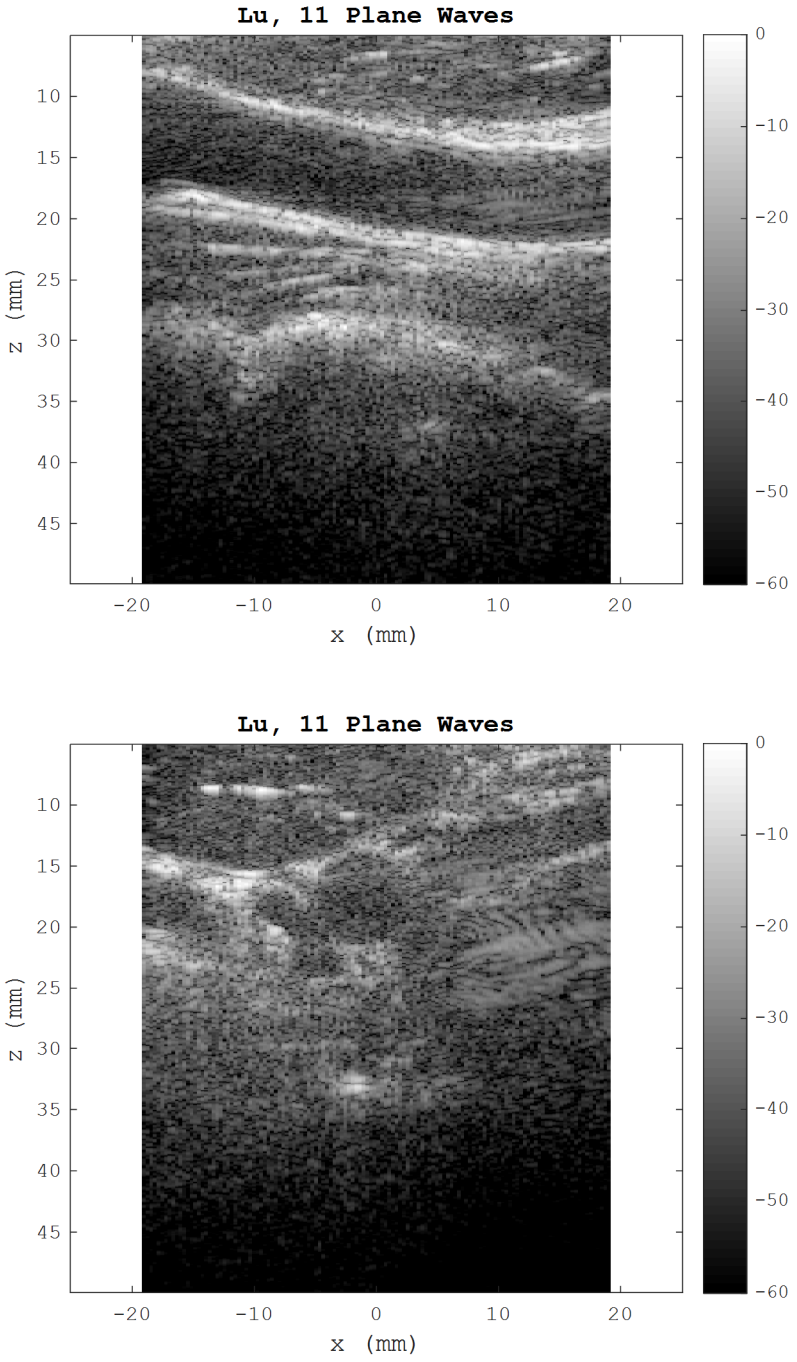

Figure 4.4: Carotid artery, longitudinal (top) and cross (bottom) sections, 11 plane-wave emissions, Lu's method [11].

We let the number of DAS scanlines be equal to the number of transducer elements n_x = 128, so that the DAS beamformed images have the same size as those obtained by the Fourier-domain methods. All implementations reported here process full-sized raw RF data frames to produce full-sized reconstructed test images. The PICMUS-provided CNR and FWHM evaluation routines expect (as an input) image sections whose depth ranges from 5 to 50 mm. Thus, all test images have been cropped accordingly and assessed using the same evaluation code as implemented by the PICMUS developers [17].

4.3 Computational Complexity

The worst-case runtime complexity of DAS beamforming is $O(n_x\, n_t\, n_s)$ per data frame [60], where n_s is the number of scanlines (equal to n_x here). For Lu's, Garcia's, and our proposed Stolt's methods, the complexity is $O(n_x\, n_t \log(n_s\, n_t))$, which is dominated by the cost of computing FFT/IFFT [50, 21]. As to be expected, we have observed that these three methods perform image reconstruction faster than DAS beamforming. The computational cost of obtaining the (k, α)-domain data dominates the UFSB complexity of $O(n_x\, n_t\, n_\alpha)$, where n_α is the number of angular samples used during two-dimensional interpolation. Our proposed SSM method is asymptotically as expensive as UFSB. Its complexity is $O(n_x\, n_t\, n_p)$, dominated by one-dimensional interpolations performed n_p times along the t-axis for each x-axis point, where n_p is the number of p_x slants being stacked. Table 4.1 provides a breakdown of computational complexities associated with each reconstruction method.

Table 4.1: Complexity of individual steps per frame in all reconstruction methods.

Reconstruction Method	Steps	Execution Time Complexity
DAS	2-D linear interpolation	$O(n_x n_t n_s)$
	Weighting and summation	$O(n_x n_t n_s)$
Lu	2-D FFT	$O(n_x n_t \log(n_x n_t))$
	Phase shift $e^{j2\pi f \frac{x}{c} \sin\theta}$	$O(n_x n_t)$
	1-D linear interpolation	$O(n_x n_t)$
	2-D IFFT	$O(n_x n_t \log(n_x n_t))$
Garcia	2-D FFT	$O(n_x n_t \log(n_x n_t))$
	Phase shift $e^{j2\pi f \frac{x}{c} \sin\theta}$	$O(n_x n_t)$
	1-D linear interpolation	$O(n_x n_t)$
	Amplitude scaling	$O(n_x n_t)$
	Phase shift $e^{j\frac{2\pi k_x \frac{z}{c} \sin\theta}{2-\cos\theta}}$	$O(n_x n_t)$
	2-D IFFT	$O(n_x n_t \log(n_x n_t))$
UFSB	1-D FFT	$O(n_x n_t \log(n_t))$
	Phase shift $e^{j2\pi f \frac{x}{c} \sin\alpha}$ and summation	$O(n_\alpha n_x n_t)$
	2-D linear interpolation	$O(n_\alpha n_t)$
	2-D IFFT	$O(n_x n_t \log(n_x n_t))$
Proposed Stolt's	2-D FFT	$O(n_x n_t \log(n_x n_t))$
	1-D linear interpolation	$O(n_x n_t)$
	Amplitude scaling	$O(n_x n_t)$
	Phase shift $e^{j\pi(\hat{k}_z x \tan\theta)}$	$O(n_x n_t)$
	2-D IFFT	$O(n_x n_t \log(n_x n_t))$
Proposed SSM	1-D FFT	$O(n_x n_t \log(n_t))$
	Phase shift $e^{-j2\pi f p_x x}$ and summation	$O(n_p n_x n_t)$
	Amplitude scaling $\lvert f \rvert$	$O(n_p n_t)$
	1-D IFFT	$O(n_p n_t \log(n_t))$
	1-D linear interpolation and stacking	$O(n_p n_x n_t)$
	1-D linear interpolation $\hat{z} = z^* + x\frac{\tan\theta}{2}$	$O(n_x n_t)$

Table 4.2, on the other hand, shows the observed execution times per compounded image on a workstation (3.4-GHz i7 CPU, 8-GB RAM, Scientific Linux 6.8 OS, MATLAB version R2016a) during *in-vitro* dataset processing. Section 4.2 provides the corresponding implementation details for each method under consideration.

Table 4.2: CPU time in seconds.

Reconstruction Method	Single PW	11 PWs	75 PWs	Average per PW
DAS[a]	1.1703	12.5232	87.1456	1.1569
DAS[b]	1.1618	12.7356	85.8364	1.1547
DAS[c]	1.0672	11.6964	78.6918	1.0599
Lu	0.4204	3.4911	21.8020	0.3428
Garcia	0.3372	5.2623	36.2447	0.4330
UFSB[a]	2.6154	30.8666	185.3417	2.6309
UFSB[b]	3.0768	30.6848	206.9356	2.8752
UFSB[c]	6.2380	66.7104	450.2014	6.1018
Proposed Stolt's	0.1139	0.7345	4.9142	0.0821
Proposed SSM[a]	2.5806	26.2536	178.9169	2.4509
Proposed SSM[b]	3.6763	39.3615	268.4037	3.6111
Proposed SSM[c]	5.0392	54.4388	364.1729	4.9479

4.4 Two Cyst Phantoms (*in-vitro*)

Table 4.3 lists the CNR values for the cyst phantoms *X* (top) and *Y* (bottom), obtained by DAS[a,b,c] beamforming and the Fourier-domain methods under consideration. Figures 4.5-4.10 show the example images reconstructed using Garcia's method, UFSB[b], and our proposed Stolt's and SSM[b] methods.

Among nine implementations of the Fourier-domain methods listed in Table 4.3, SSM^{a} and UFSB^{a} produce the best and second-best CNR_X values in the single-emission scenario (8.5 and 8.3 dB, respectively). In the case of 11 plane-wave emissions, the best and second-best CNR_X values are achieved by SSM^{a} and SSM^{b} (10.7 and 10.6 dB, respectively). In the case of 75 plane-wave emissions, SSM^{c} yields the best CNR_X = 13.1 dB, followed by our Stolt's and SSM^{b} methods producing the second-best CNR_X = 12.9 dB.

On the other hand, the best and second-best CNR_Y values in the single-emission scenario are achieved by UFSB^{a} and Lu's method (8.8 and 8.5 dB, respectively). In the case of 11 plane-wave emissions, our Stolt's method and UFSB^{c} yield the best and second-best CNR_Y values (11.6 and 11.5 dB, respectively). In the case of 75 plane-wave emissions, our Stolt's method produces the best CNR_X = 12.2 dB, while SSM^{a} yields the second-best CNR_X = 11.9 dB.

Table 4.3: Experimental contrast (CNR) of cyst phantoms *X* (near-field) and *Y* (far-field).

Reconstruction Method	Cyst *X*, CNR_X in (dB)			Cyst *Y*, CNR_Y in (dB)		
	Single PW	11 PWs	75 PWs	Single PW	11 PWs	75 PWs
DAS[a]	2.5	8.4	13.0	8.7	11.5	11.9
DAS[b]	8.6	11.5	12.7	6.8	11.6	11.9
DAS[c]	10.3	12.2	12.7	8.6	11.7	11.9
Lu/Liu	5.9	6.8	11.0	8.5	11.4	11.7
Garcia	5.6	7.1	11.3	7.8	10.7	11.6
UFSB[a]	8.3	9.2	11.5	**8.8**	10.8	11.2
UFSB[b]	6.3	9.7	11.1	8.1	11.3	11.6
UFSB[c]	6.4	9.0	10.9	8.2	11.5	11.4
Proposed Stolt's	6.0	10.5	12.9	7.1	**11.6**	**12.2**
Proposed SSM[a]	**8.5**	**10.7**	12.7	7.3	10.9	11.9
Proposed SSM[b]	7.6	10.6	12.9	8.3	11.2	11.8
Proposed SSM[c]	4.8	10.2	**13.1**	7.6	11.1	11.8

Table 4.3 shows that UFSB and SSM are somewhat sensitive to the user's choice of their respective implementation parameters (range and discretization). The optimal parameter configuration is likely to be data-dependent, which motivates further investigations into adaptive UFSB and SSM techniques in the future. We have explored only a few parameter setting variations, and it is possible that the CNR values shown in Table 4.3 for UFSB and SSM could still be improved. Nevertheless, it is clear that SSM is certainly competitive with UFSB.

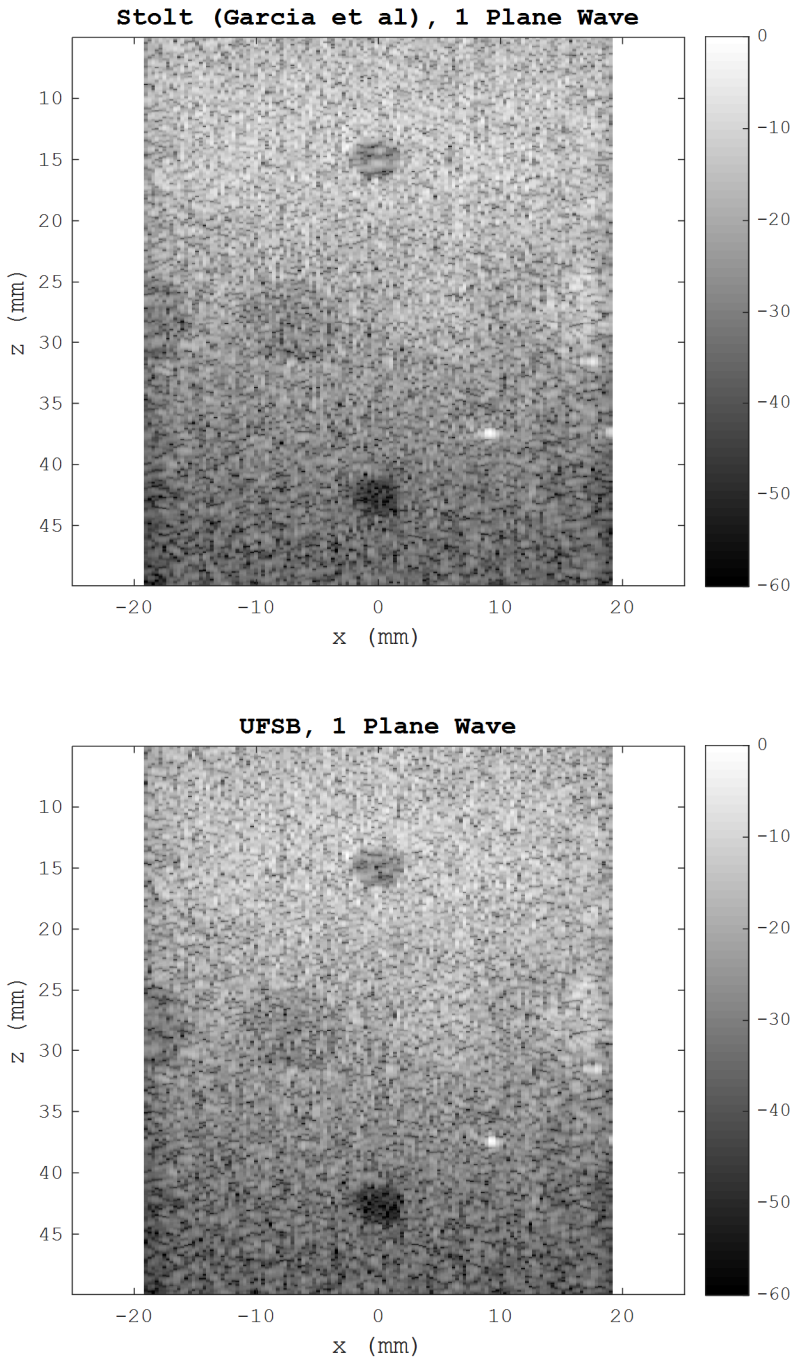

Figure 4.5: Two anechoic cyst phantoms, single plane-wave emission, Garcia's method (top) and UFSB[b] (bottom) [9, 21].

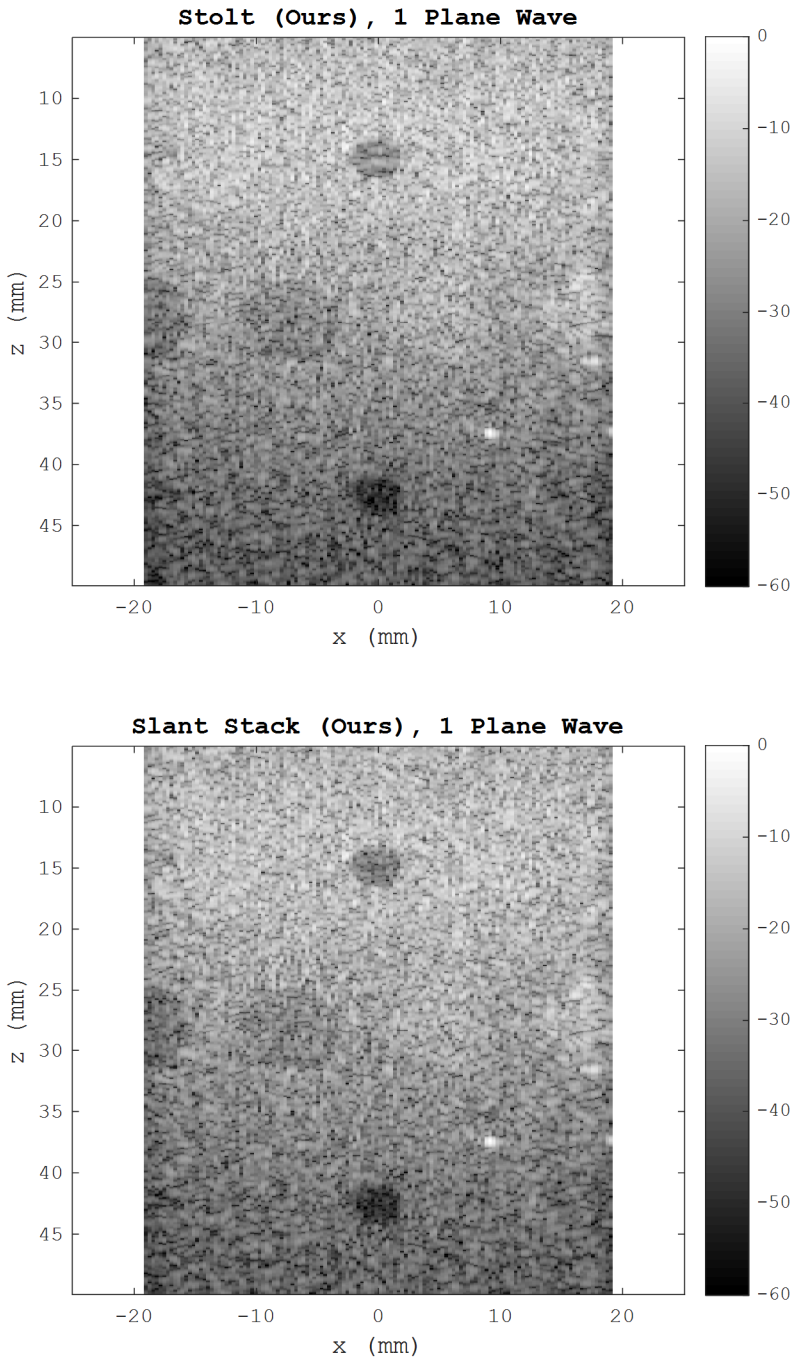

Figure 4.6: Two anechoic cyst phantoms, single plane-wave emission, our proposed Stolt's method (top) and SSM[b] method (bottom) [1].

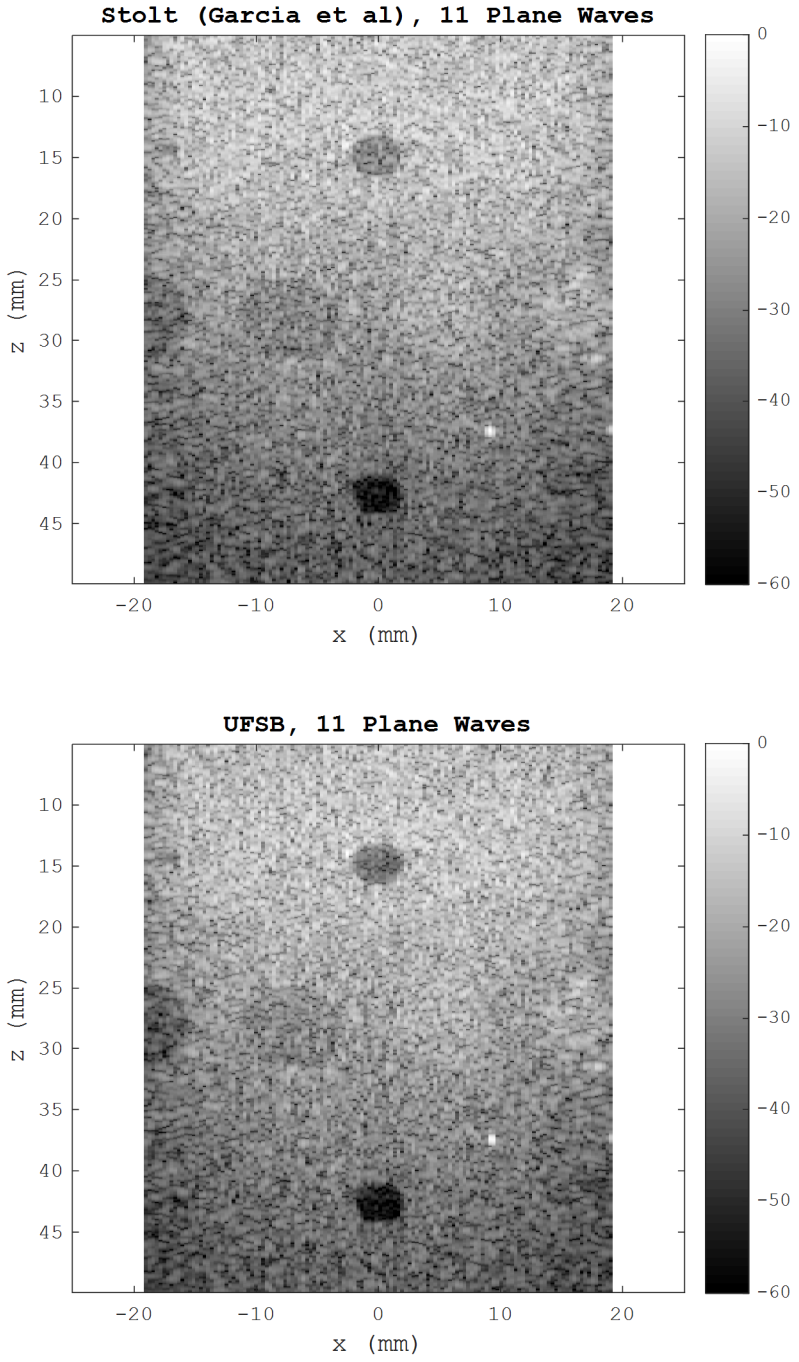

Figure 4.7: Two anechoic cyst phantoms, 11 plane-wave emissions, Garcia's method (top) and UFSB[b] (bottom) [9, 21].

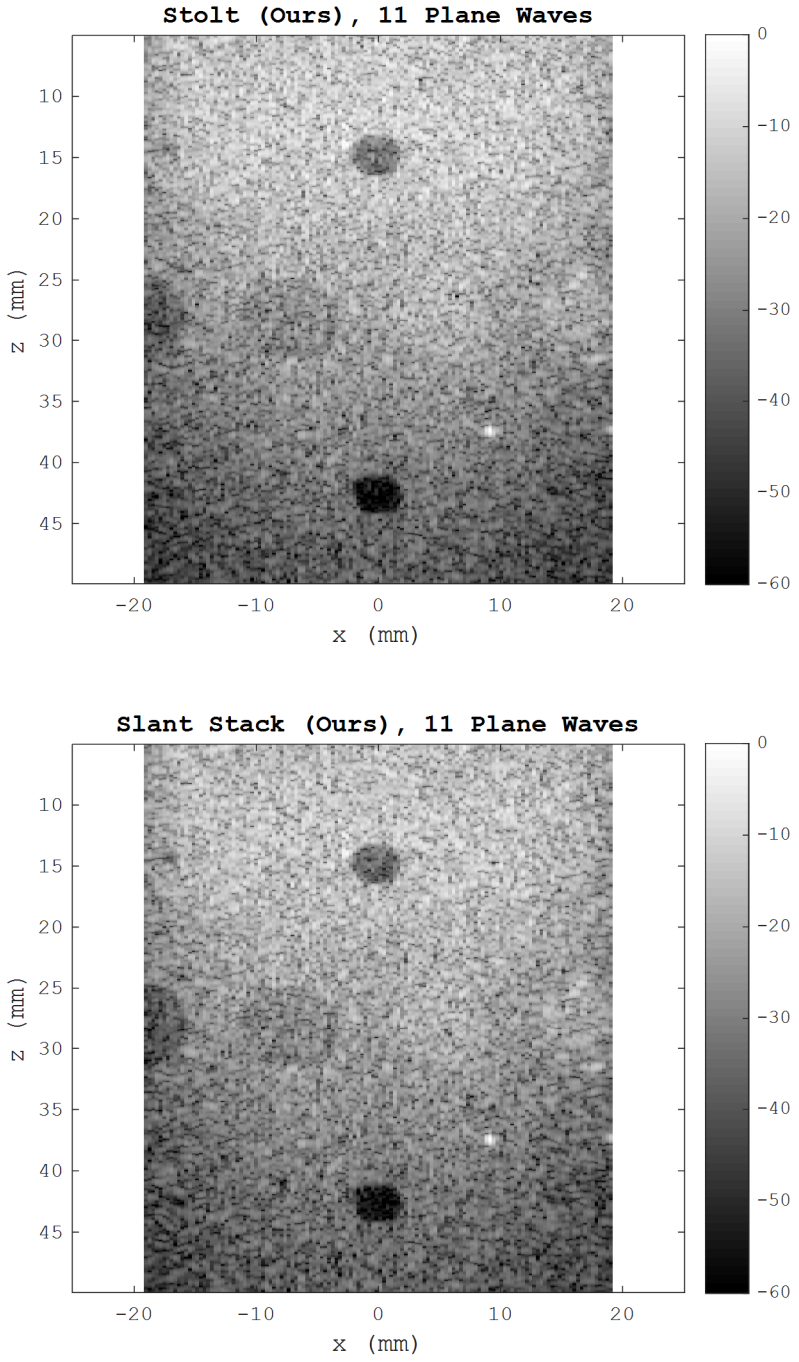

Figure 4.8: Two anechoic cyst phantoms, 11 plane-wave emissions, our proposed Stolt's method (top) and SSM[b] method (bottom) [1].

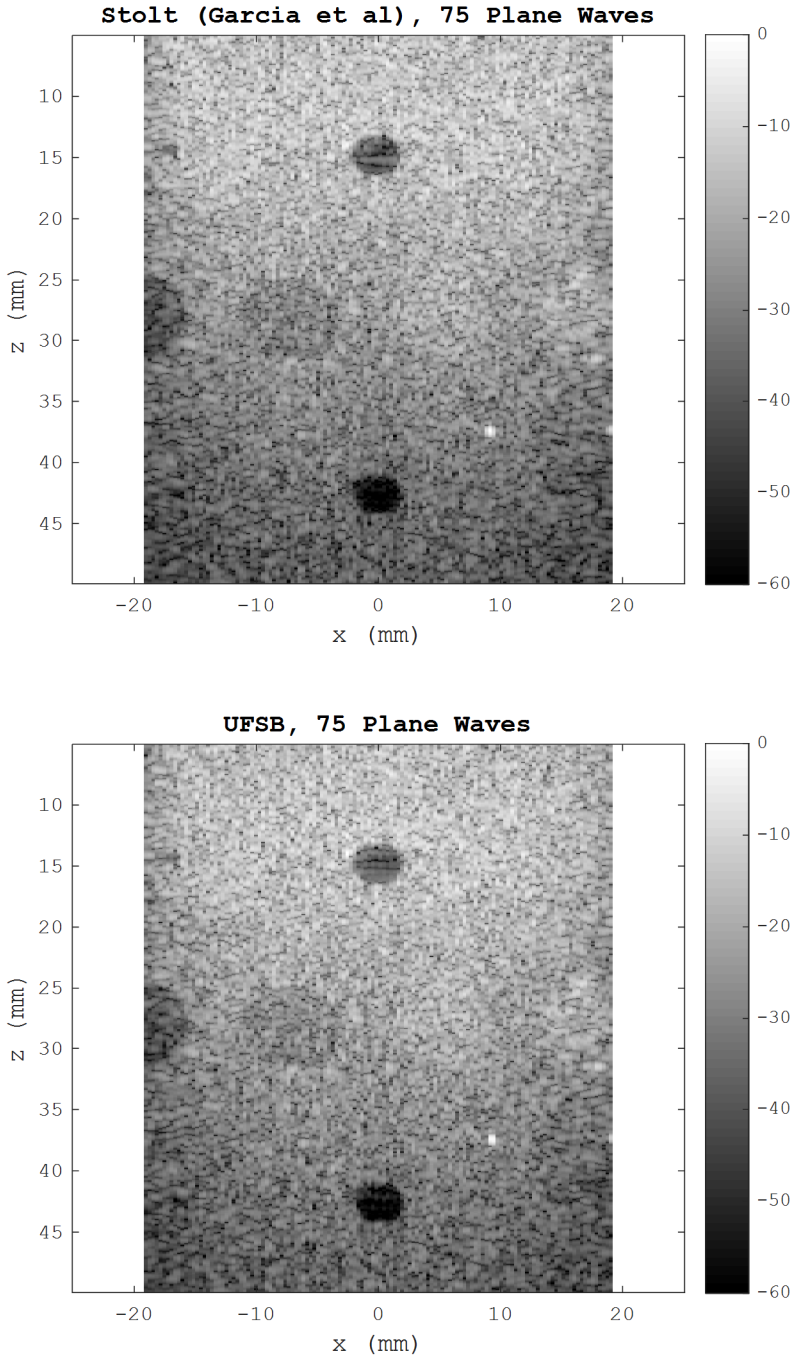

Figure 4.9: Two anechoic cyst phantoms, 75 plane-wave emissions, Garcia's method (top) and UFSB[b] (bottom) [9, 21].

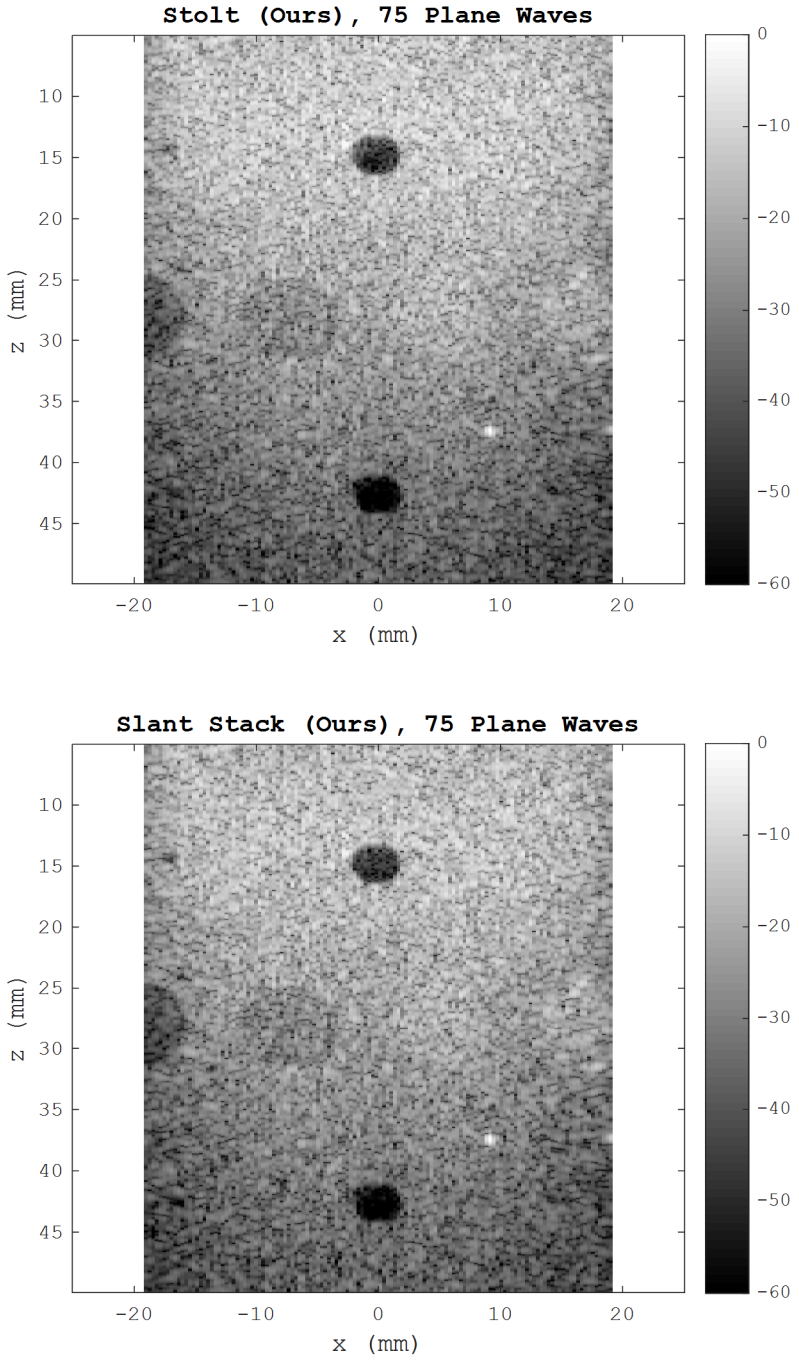

Figure 4.10: Two anechoic cyst phantoms, 75 plane-wave emissions, our proposed Stolt's method (top) and SSM^{b} method (bottom) [1].

Table 4.3 shows that UFSB and SSM are somewhat sensitive to the user's choice of their respective implementation parameters (range and discretization). The optimal parameter configuration is likely to be data-dependent, which motivates further investigations into adaptive UFSB and SSM techniques in the future. We have explored only a few parameter setting variations, and it is possible that the CNR values shown in Table 4.3 for UFSB and SSM could still be improved. Nevertheless, it is clear that SSM is certainly competitive with UFSB.

According to Table 4.3, our Stolt's method outperforms that of Garcia *et al.* [21] in most cases. While both methods aim to adapt classic Stolt's migration to plane-wave imaging, their resulting modifications are drastically different, as explained in Section 3.5. In the single-emission scenario, Garcia's method yields higher CNR_Y = 7.8 dB but lower CNR_X = 5.6 dB compared to those obtained by our Stolt's method (7.1 and 6.0 dB, respectively). In the case of 11 plane-wave emissions, our Stolt's method produces CNR_X = 10.5 dB and CNR_Y = 11.6 dB, which are better than those obtained by Garcia's method (7.1 dB and 10.7 dB, respectively). Similarly, in the case of 75 plane-wave emissions, our Stolt's method yields CNR_X = 12.9 dB and CNR_Y = 12.2 dB, which are better than those obtained by Garcia's method (11.3 dB and 11.6 dB, respectively). As for Lu's method [11, 50], it also performs worse than our Stolt's method in all cases but one, which is the single-emission scenario, where the former's CNR_Y = 8.5 dB is better than the latter's CNR_Y = 7.1 dB.

It is worth noting in Table 4.3 that DAS beamforming often offered better contrast to noise ratios than those of the Fourier domain methods under consideration. Since Lu's, Garcia's, and our Stolt's methods are faster than DAS$^{\mathbf{a,b,c}}$ beamforming, their use is always beneficial from the computational perspective. On the other hand, UFSB$^{\mathbf{a,b,c}}$ and SSM$^{\mathbf{a,b,c}}$ are slower than DAS$^{\mathbf{a,b,c}}$ beamforming, but they have not reliably produced better CNR_X or CNR_Y . Further research is needed to improve both UFSB and SSM in terms of their computational efficiency and image contrast performance [9].

4.5 Seven Point Phantoms (*in-vitro*)

Table 4.4 lists the average lateral and axial FWHM values for the point phantoms *A*-*G*, obtained by DAS$^{\mathbf{a,b,c}}$ beamforming and the Fourier-domain methods under consideration. Figures 4.11-4.16 show the example images reconstructed using Garcia's method, UFSB$^{\mathbf{b}}$, and our proposed Stolt's and SSM$^{\mathbf{b}}$ methods. Since the average axial FWHM values did not vary significantly (ranging from 0.54 mm to 0.58 mm), we limit our further discussion to lateral resolution only.

Among nine implementations of the Fourier-domain methods listed in Table 4.4, the best and second-best average lateral FWHM values in the single-emission scenario are achieved by Lu's and our Stolt's methods (0.40 and 0.41 mm, respectively). In the case of 11 plane-wave emissions, our Stolt's method and SSM$^{\mathbf{c}}$ yield the best lateral resolution (FWHM = 0.29 mm), followed by Lu's method and SSM$^{\mathbf{b}}$ (FWHM = 0.31 mm). In the

case of 75 plane-wave emissions, the best and second-best average lateral FWHM values are obtained by SSM[c] and our Stolt's method (0.28 and 0.29 mm, respectively).

Table 4.4: Averaged experimental resolution (FWHM) for point phantoms *A*-*G*.

Reconstruction Method	Mean Lateral/Axial FWHM in (mm)		
	Single PW	11 PWs	75 PWs
DAS[a]	0.38/0.55	0.26/0.55	0.27/0.55
DAS[b]	0.68/0.57	0.41/0.56	0.44/0.56
DAS[c]	1.08/0.58	0.52/0.56	0.55/0.56
Lu/Liu	**0.40**/0.56	0.31/0.54	0.32/0.54
Garcia	0.64/0.57	0.33/0.55	0.35/0.55
UFSB[a]	0.56/0.57	0.46/0.56	0.43/0.56
UFSB[b]	0.51/0.56	0.42/0.55	0.42/0.55
UFSB[c]	0.50/0.56	0.42/0.55	0.41/0.55
Proposed Stolt's	0.41/0.56	**0.29**/0.55	0.29/0.54
Proposed SSM[a]	0.67/0.57	0.42/0.57	0.44/0.56
Proposed SSM[b]	0.50/0.57	0.31/0.56	0.31/0.56
Proposed SSM[c]	0.42/0.56	**0.29**/0.56	**0.28**/0.56

As we have mentioned earlier, direct comparisons between UFSB and SSM can be misleading, because their performance is affected by the user-chosen parameter settings. For example, in the case of 75 plane-wave emissions, UFSB[c] is better than SSM[a] but worse than SSM[b], in terms of their respective FHWM values. It suffices to say that both UFSB and SSM produce competitive results. As for our Stolt's method, in comparison to Lu's and Garcia's methods, it offers better lateral resolution in all cases but one: in the single-emission scenario, Lu's method yields the average lateral FWHM value of 0.40 mm, which is better than 0.41 mm obtained by our Stolt's method.

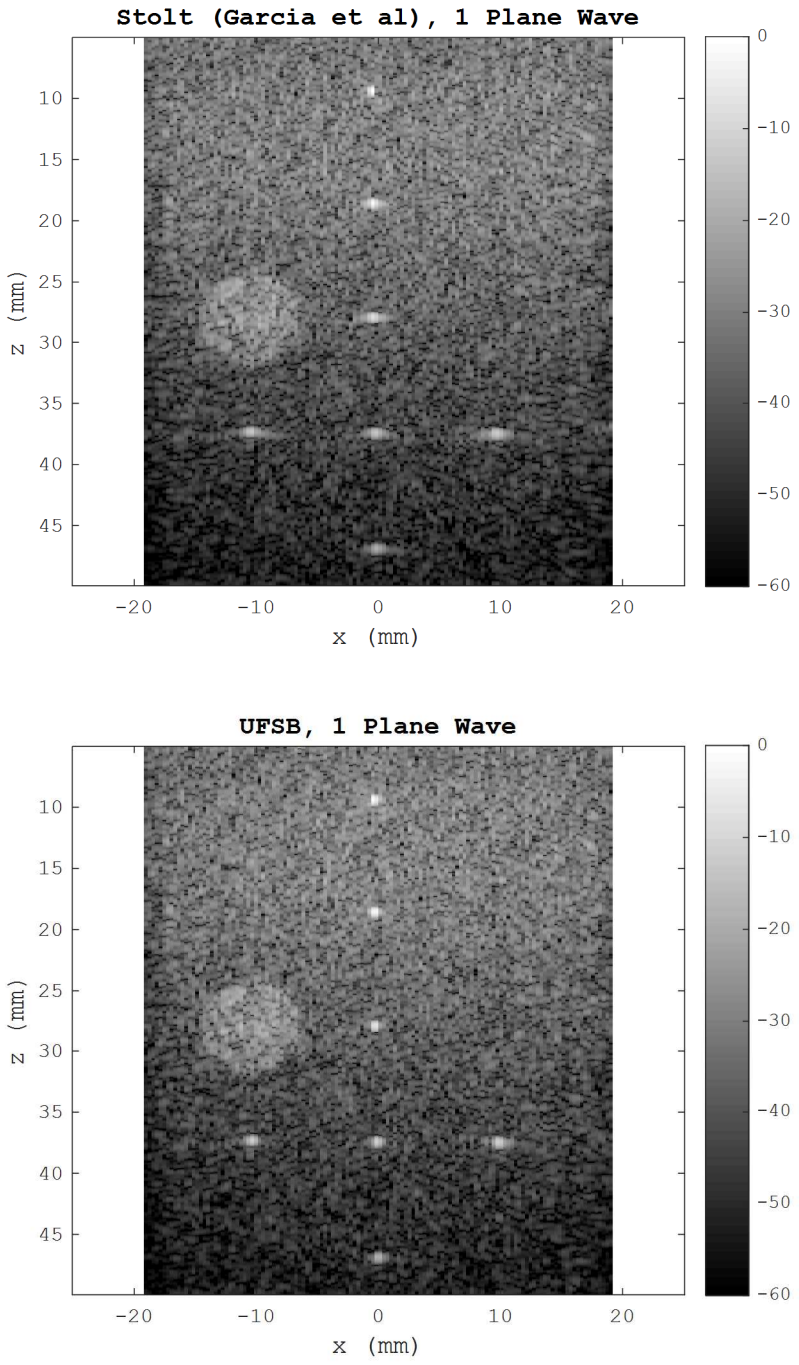

Figure 4.11: Point phantoms, single plane-wave emission, Garcia's method (top) and UFSB[b] (bottom) [9, 21].

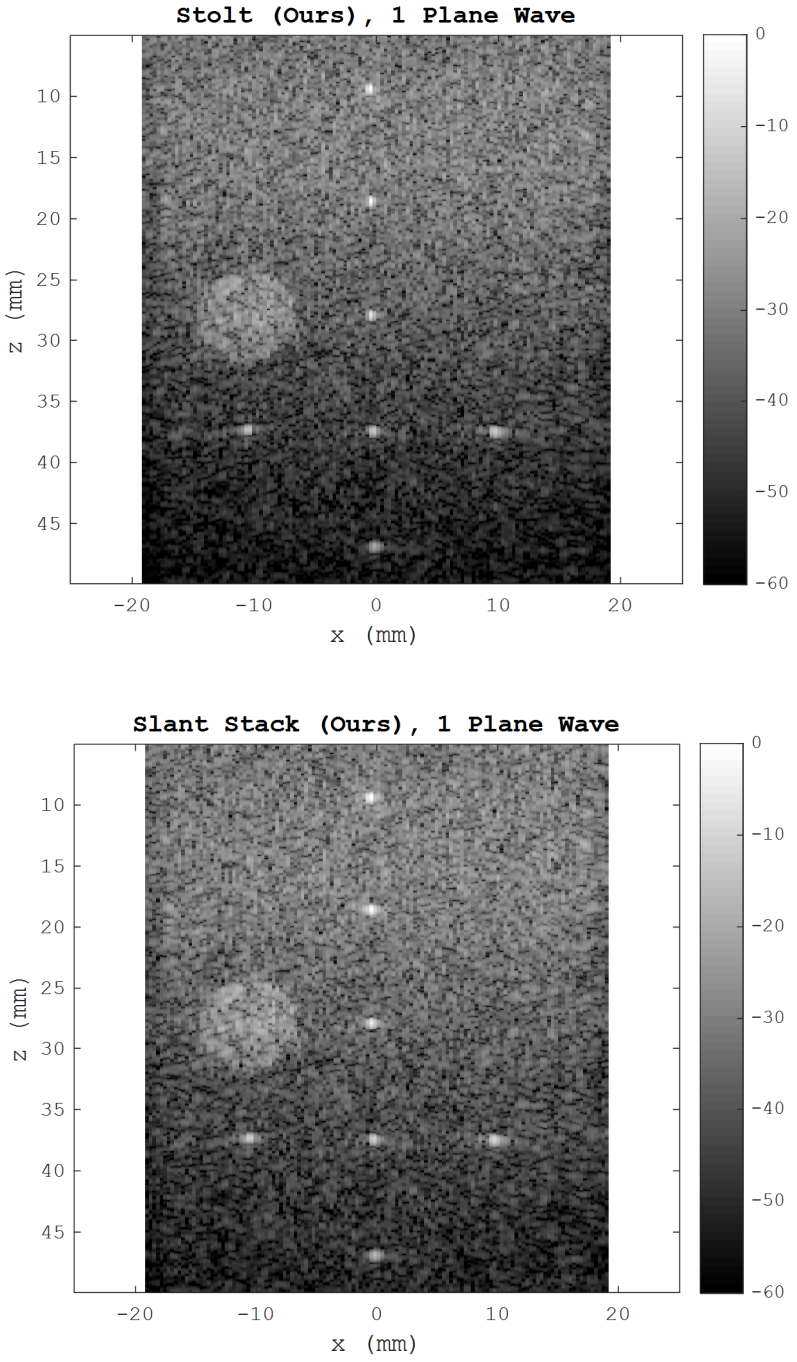

Figure 4.12: Point phantoms , single plane-wave emission, our proposed Stolt's method (top) and SSM[b] method (bottom) [1].

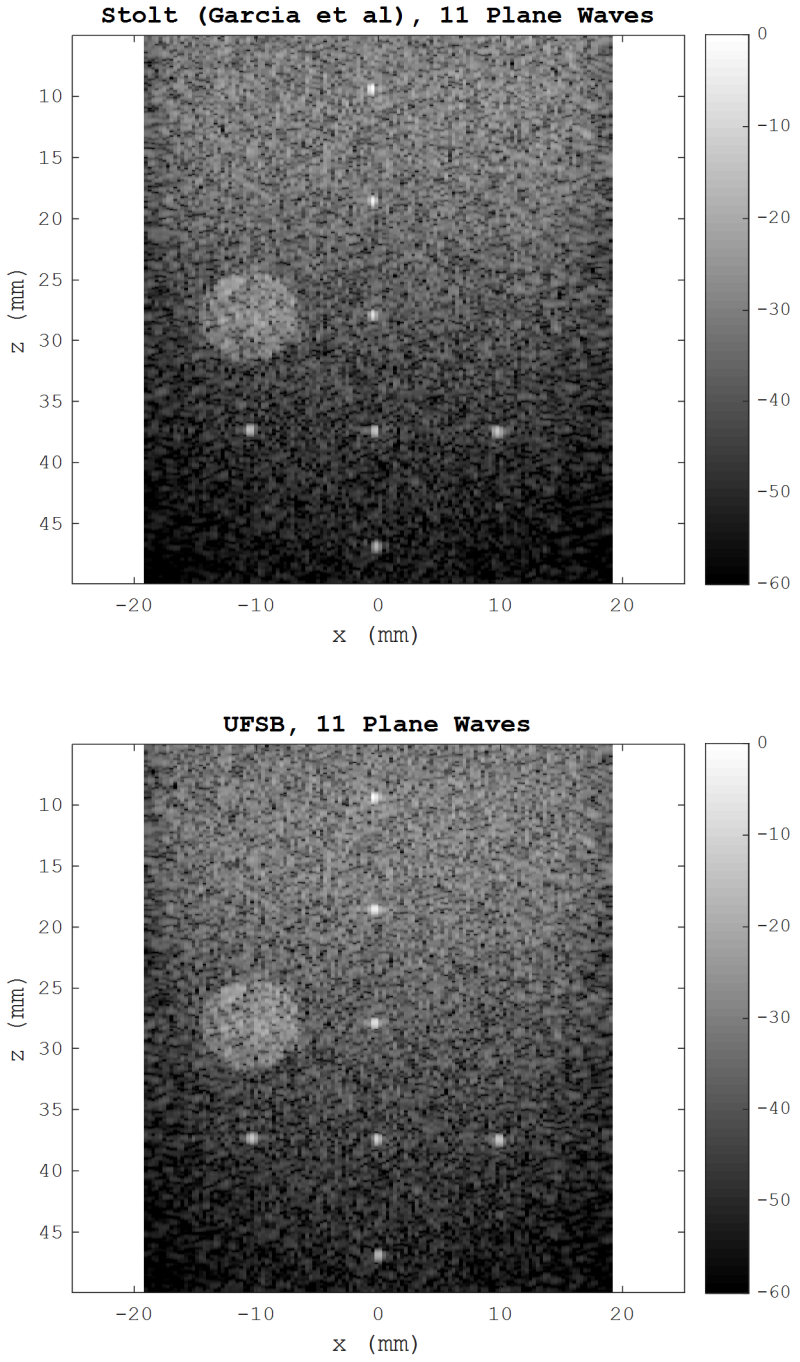

Figure 4.13: Point phantoms, 11 plane-wave emissions, Garcia's method (top) and UFSB[b] (bottom) [9, 21].

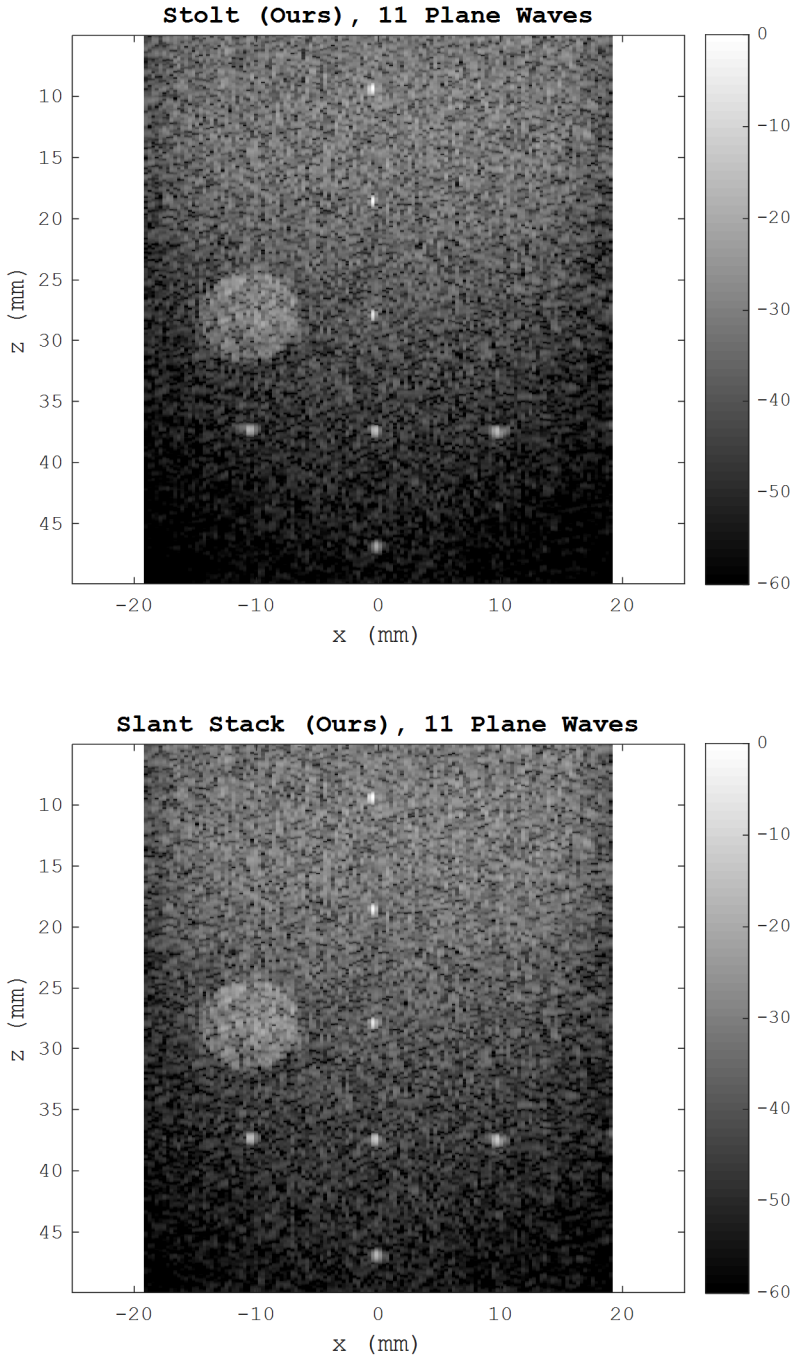

Figure 4.14: Point phantoms , 11 plane-wave emissions, our proposed Stolt's method (top) and SSM[b] method (bottom) [1].

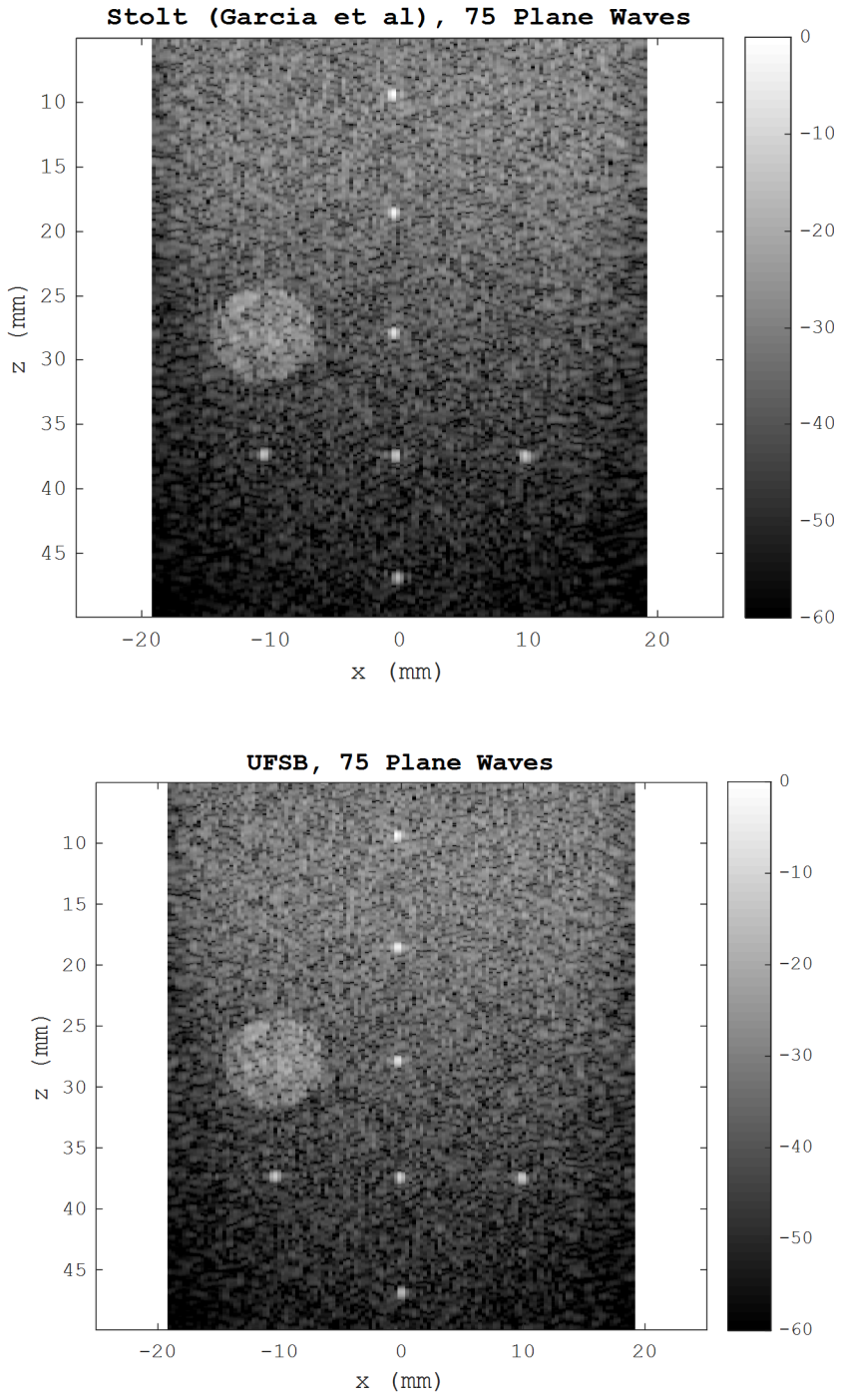

Figure 4.15: Point phantoms, 75 plane-wave emissions, Garcia's method (top) and UFSB[b] (bottom) [9, 21].

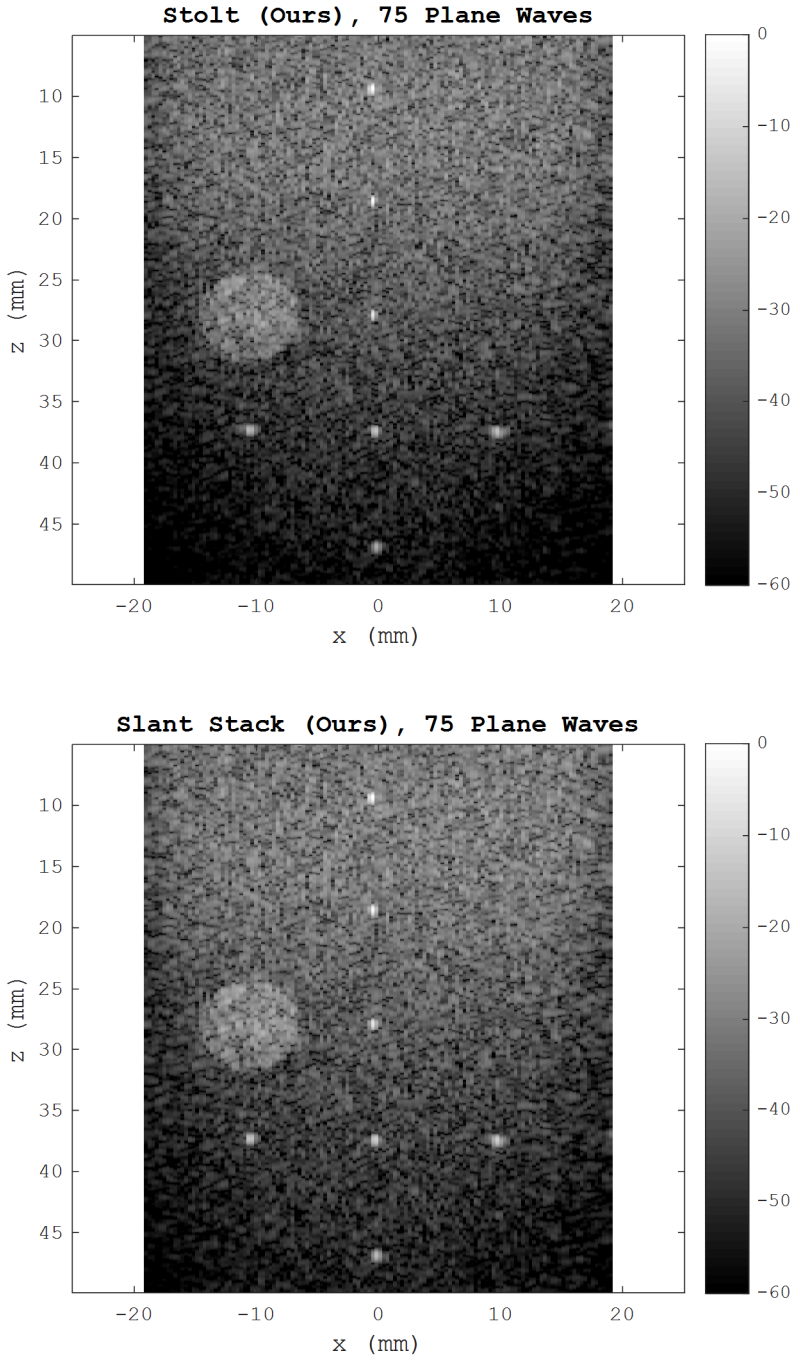

Figure 4.16: Point phantoms , 75 plane-wave emissions, our proposed Stolt's method (top) and SSM[b] method (bottom) [1].

According to Table 4.4, the DAS^{a} beamformer was the best in terms of lateral resolution, and the DAS^{c} beamformer turned out to be the worst. The Fourier-domain methods under consideration outperformed the latter by a sizable margin, which suggests their potential use for enhancing image resolution relative to DAS-Hamming beamforming. Replacing Hamming receive apodization with Hann and Tukey alternatives [17] led us to a similar conclusion.

4.6 Carotid Artery (*in-vivo*)

In addition to the *in-vitro* phantom benchmarks, PICMUS [17] also provides *in-vivo* measurement data for the longitudinal and cross sections of the carotid artery. Figure 4.2 shows the DAS^{c} beamformed images in the case of 75 plane-wave emissions (to be treated as a reference). On the other hand, Figures 4.4 and 4.17-4.20 show the test images reconstructed by the Fourier-domain methods in the case of 11 plane-wave emissions.

The compounded images obtained by the DAS^{c} beamformer using all 75 plane-wave emissions provide a much better view of the carotid artery sections than those obtained by Lu's, Garcia's, UFSB, and our proposed techniques using only 11 plane-wave emissions. Next, we evaluate the Fourier-domain methods under consideration in terms of their respective image data (i.e., two-dimensional normalized and log-compressed envelope) similarity to the reference image data produced by DAS^{c} Hamming beamforming.

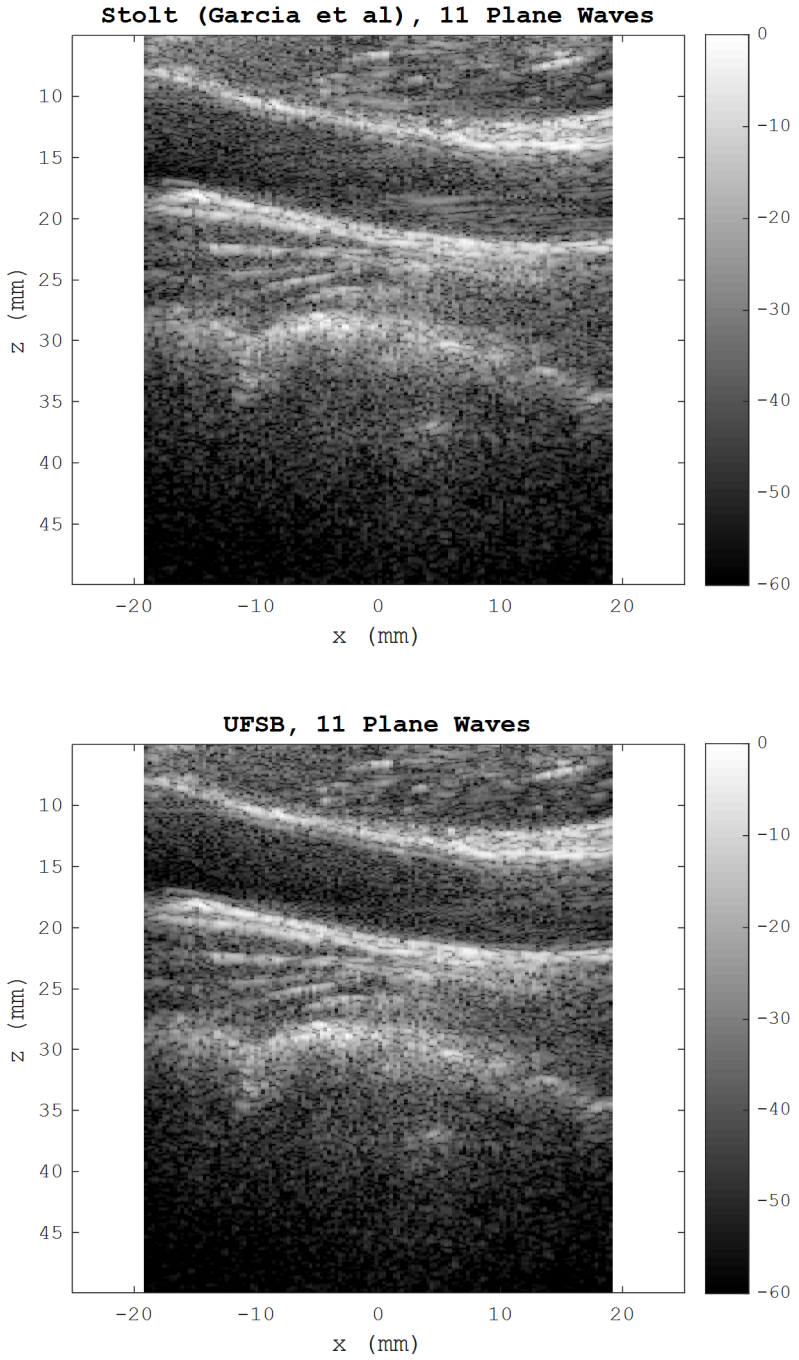

Figure 4.17: Carotid artery, longitudinal section, 11 plane-wave emissions, Garcia's method (top) and UFSB[b] (bottom) [9, 21].

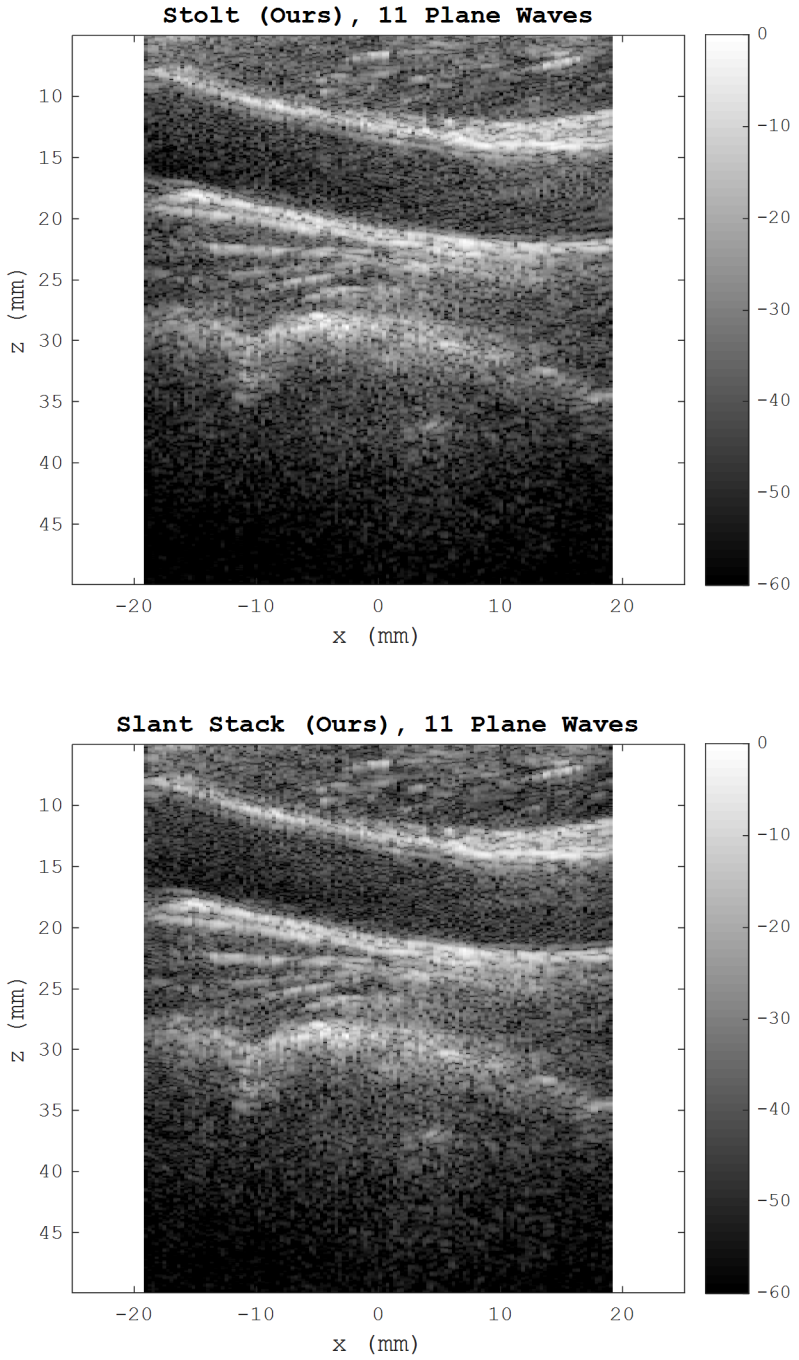

Figure 4.18: Carotid artery, longitudinal section, 11 plane-wave emissions, our proposed Stolt's method (top) and SSM[b] method (bottom) [1].

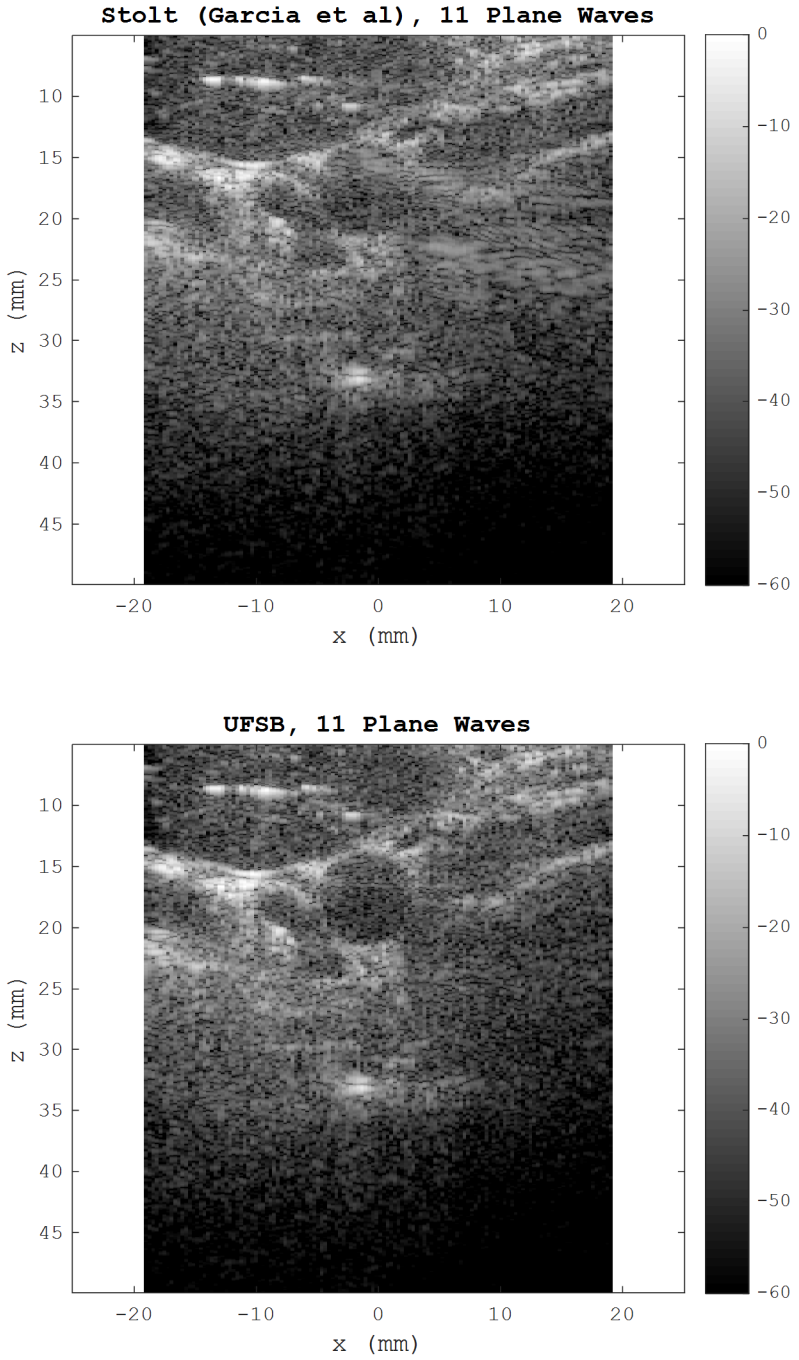

Figure 4.19: Carotid artery, cross section, 11 plane-wave emissions, Garcia's method (top) and UFSB[b] (bottom) [9, 21].

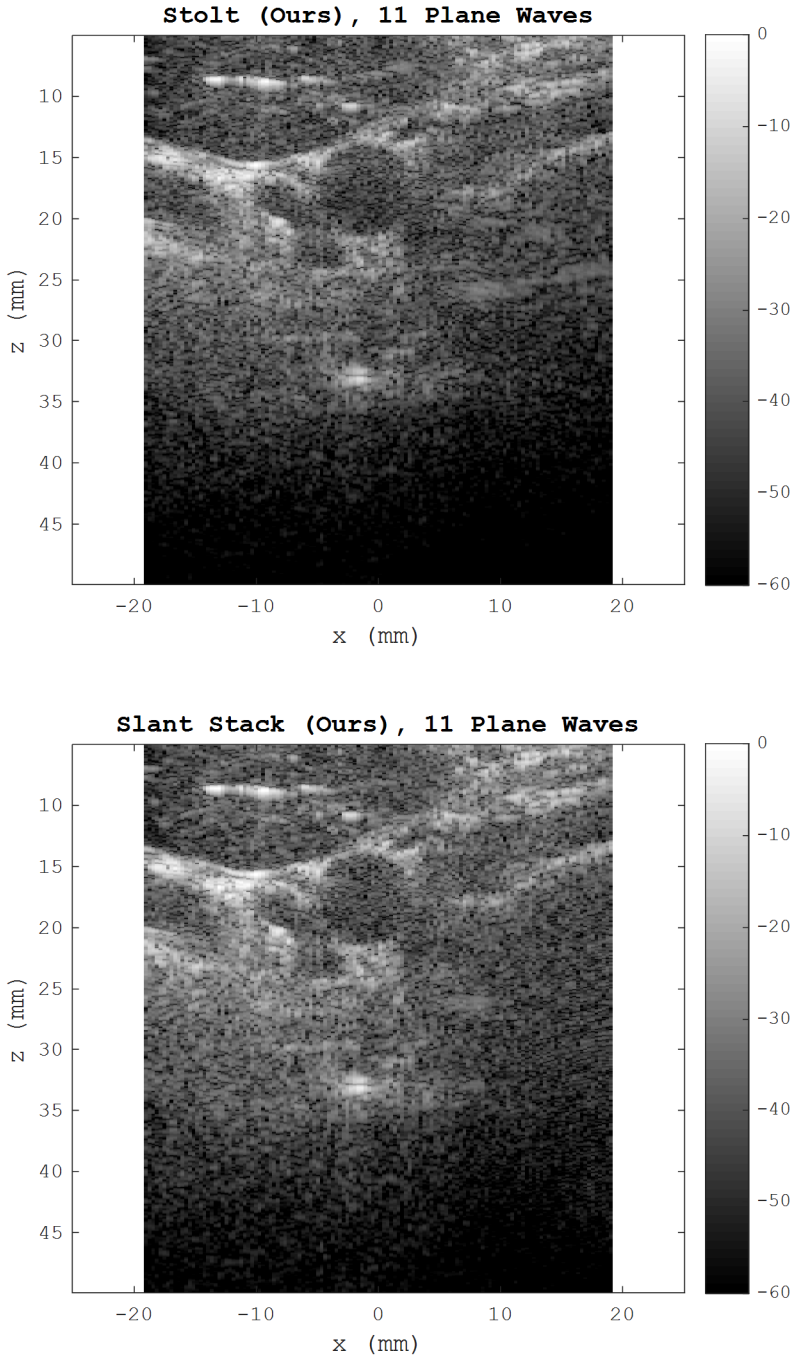

Figure 4.20: Carotid artery, cross section, 11 plane-wave emissions, our proposed Stolt's method (top) and SSM[b] method (bottom) [1].

Table 4.5: Image data similarity, Fourier-domain methods (11 plane waves) versus DAS-Hamming beamforming (75 plane waves).

Reconstruction Method	Longitudinal-section		Cross-section	
	$SSIM_{LS}$	MSE_{LS}	$SSIM_{CS}$	MSE_{CS}
Lu/Liu	0.347	63.5	0.233	102.1
Garcia	0.369	63.1	0.251	108.8
UFSB[a]	0.306	53.8	0.228	**72.6**
UFSB[b]	0.302	55.5	0.224	82.7
UFSB[c]	0.288	59.2	0.205	87.9
Proposed Stolt's	0.341	59.6	0.234	87.6
Proposed SSM[a]	**0.435**	**42.2**	**0.317**	79.7
Proposed SSM[b]	0.373	48.8	0.262	103.7
Proposed SSM[c]	0.327	56.7	0.232	132.5

Our quantitative comparisons, reported in Table 4.5, are based on the structural similarity index (SSIM) [93] and mean-squared error (MSE). According to Table 4.5, SSM[a] offers the best SSIM-based performance with $SSIM_{LS} = 0.435$ (longitudinal section) and $SSIM_{CS} = 0.317$ (cross section), while SSM[b] yields the second best $SSIM_{LS} = 0.373$ (14.3% worse than SSM[a]) and $SSIM_{CS} = 0.262$ (17.4% worse than SSM[a]). Regarding the MSE-based performance, SSM[a] and UFSB[a] offer the best $MSE_{LS} = 42.2$ (longitudinal section) and $MSE_{CS} = 72.6$ (cross section), respectively. The second best $MSE_{LS} = 48.8$ (15.6% worse than SSM[a]) and $MSE_{CS} = 79.7$ (9.8% worse than UFSB[a]) are achieved by SSM[b] and SSM[a], respectively.

Table 4.5 shows that our Stolt's method outperforms both Garcia's and Lu's methods in terms of MSE_{LS} and MSE_{CS}, whereas Garcia's method outperforms both Lu's and our Stolt's methods in terms of $SSIM_{LS}$ and $SSIM_{CS}$. Not surprisingly, the relative performance of UFSB and SSM is affected by the user's choice of their parameter settings. For example, SSM^{c} is worse than $UFSB^{a,b}$ but better than $UFSB^{c}$ in terms of MSE_{LS}, while SSM^{a} is better than $UFSB^{b,c}$ but worse than $UFSB^{a}$ in terms of MSE_{CS}. Table 4.5 also indicates that the SSIM-based performance of SSM is generally better than that of UFSB.

4.7 Summary

Lu's, Garcia's, and our Stolt's methods reconstruct images faster than $DAS^{a,b,c}$, $UFSB^{a,b,c}$, and $SSM^{a,b,c}$ techniques. Table 4.6 ranks them according to their relative imaging performance (based on Tables 4.3, 4.4, and 4.5). One can see that in comparison to Lu's and Garcia's methods, our Stolt's method performs better in terms of MSE, near-field CNR_X, multiple-emission far-field CNR_Y, and multiple-emission lateral FWHM. However, our Stolt's method performs worse than Garcia's method in terms of SSIM and worse than Lu's method in terms of single emission far-field CNR_Y and single-emission lateral FWHM. Overall, our Stolt's method fares quite well relative to Garcia's and Lu's methods.

Table 4.7 ranks our Stolt's and slant-stack migration methods exclusively. Given that the latter is significantly slower than the former, we recommend using SSM^{a} (instead of

our Stolt's method) only when targeting MSE, SSIM, or single-emission near-field CNR_X. One may also consider using SSM^b when targeting single-emission far-field CNR_Y, or using SSM^c when targeting lateral FWHM in the case of 75 plane-wave emissions.

Table 4.6: Relative performance of Lu's, Garcia's and our proposed Stolt's methods based on Tables 4.3, 4.4, and 4.5.

Performance Indicator		Reconstruction Method		
		Lu's	Garcia's	Our Stolt's
CNR_X	Single PW	-1.7%	-6.7%	MAX
	11 PWs	-18.1%	-32.4%	MAX
	75 PWs	-14.7%	-12.4%	MAX
CNR_Y	Single PW	MAX	-8.2%	-16.5%
	11 PWs	-1.7%	-7.8%	MAX
	75 PWs	-4.1%	-4.9%	MAX
FWHM	Single PW	MIN	+60.0%	+2.5%
	11 PWs	+6.9%	+13.8%	MIN
	75 PWs	+10.3%	+20.7%	MIN
$SSIM_{LS}$	11 PWs	-6.0%	MAX	-7.6%
$SSIM_{CS}$	11 PWs	-7.2%	MAX	-6.8%
MSE_{LS}	11 PWs	+6.5%	+5.9%	MIN
MSE_{CS}	11 PWs	+16.6%	+24.2%	MIN

Table 4.7: Relative performance of our proposed Stolt's and slant-stack migration methods based on Tables 4.3, 4.4, and 4. 5.

Performance Indicator		Reconstruction Method			
		Our Stolt's	SSM[a]	SSM[b]	SSM[c]
CNR_X	Single PW	-29.4%	MAX	-10.6%	-43.5%
	11 PWs	-1.9%	MAX	-0.9%	-4.7%
	75 PWs	-1.5%	-3.1%	-1.5%	MAX
CNR_Y	Single PW	-14.5%	-12.0%	MAX	-8.4%
	11 PWs	MAX	-6.0%	-3.4%	-4.3%
	75 PWs	MAX	-2.5%	-3.3%	-3.3%
FWHM	Single PW	MIN	+63.4%	+22.0%	+2.4%
	11 PWs	MIN	+44.8%	+6.9%	MIN
	75 PWs	+3.6%	+57.1%	+10.7%	MIN
$SSIM_{LS}$	11 PWs	-21.6%	MAX	-14.3%	-24.8%
$SSIM_{CS}$	11 PWs	-26.2%	MAX	-17.4%	-26.8%
MSE_{LS}	11 PWs	+41.2%	MIN	+15.6%	+34.4%
MSE_{CS}	11 PWs	+9.9%	MIN	+30.1%	+66.2%

It is important to note that our assessment of the presented Fourier-domain methods is restricted to the test cases described in this chapter. There are numerous alternative tests that can be employed for evaluation purposes (depending on one's needs), and it is possible that in certain cases a relative standing of various methods in terms of their imaging performance could change. For example, references [8, 21] provide different evaluation approaches and conclusions when comparing Lu's, Garcia's, and UFSB techniques.

Chapter 5

Phase-Shift Migration for Plane-Wave Ultrasound Imaging

5.1 Introduction

The methods mentioned in the previous two chapters assume that the speed of sound is constant throughout the propagation medium. However, in imaging cases involving inhomogeneous media with substantial propagation velocity variations (e.g., transcranial ultrasound), we are in need of a more general beamforming technique, which is the subject of this chapter. We describe a novel plane-wave image reconstruction method that takes into account vertical (depth-dependent) velocity variations in a horizontally stratified medium. Our approach is based on the geophysical concept of zero-offset phase-shift migration [24] under the exploding-reflector model assumptions [14] coupled with "explosion" time adjustments (as in the case of our plane-wave Stolt's and slant-stacking migration methods). Instead of considering two-way wave propagation along the vertical z-axis (from a given surface transmitter down to a subsurface reflector and then back up to a surface receiver at the same location), the ERM considers only one-way upward propagation at half-speed (from an "exploding" reflector to the receiver in question). Here we also allow the speed of sound to vary with depth. In what follows, it is shown how one can modify the corresponding equations of classical Gazdag's model to obtain a new method applicable to plane-wave ultrasound imaging of layered media.

5.2 Plane-Wave Phase-Shift Migration

To modify Gazdag's method for plane-wave ultrasound imaging, we first replace the ERM (upward) velocity $\hat{v}_z$ with the original two-way depth-dependent propagation velocity c_z and then multiply $\Psi(k_x, z+\Delta z, f)$ by $e^{j2\pi f\frac{\Delta z}{c}}$ in equation (2.10), rewritten here for convenience:

$$\Psi(k_x, z+\Delta z, f) = \Psi(k_x, z, f)e^{j2\pi k_z \Delta z},$$

which yields its modified version

$$\Psi(k_x, z+\Delta z, f) = \Psi(k_x, z, f)e^{j2\pi \hat{k}_z \Delta z}, \tag{5.1}$$

$$\hat{k}_z = \frac{f}{c_z} + k_z = \frac{f}{c_z}\left[1 + \sqrt{1-\left(\frac{c_z k_x}{f}\right)^2}\right], \qquad f^2 > c_z^2 k_x^2 . \tag{5.2}$$

Consequently, in the special case of $\theta = 0$, we have:

$$P(x, z+\Delta z, 0) = \iint_{f^2>c_z^2k_x^2}\left[\Psi(k_x, z, f)e^{j2\pi \hat{k}_z \Delta z}\right] dk_x df . \tag{5.3}$$

To handle plane-wave emissions with $\theta \neq 0$, we need to determine an appropriate transformation $z + \Delta z$ to $\hat{z} + \Delta\hat{z}$, associated with a propagation medium layer extending from z to $z + \Delta z$, where a refracted plane wave travels with the velocity c_z at an angle θ_z, as illustrated in Figure 5.1.

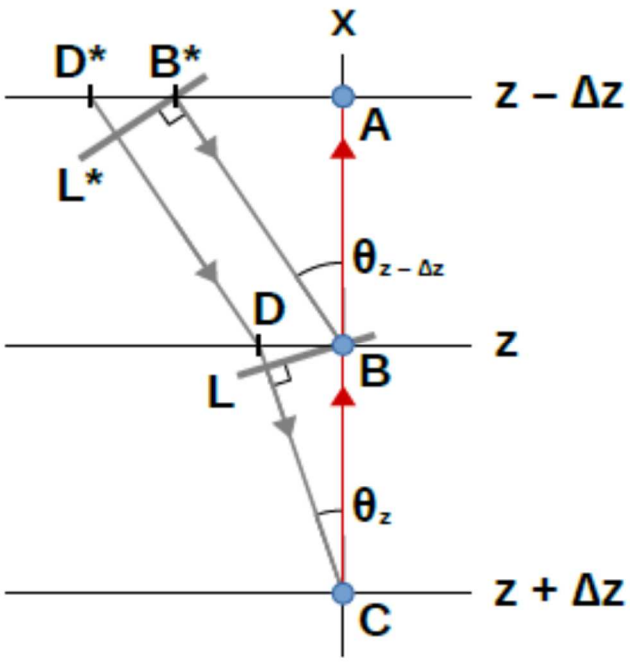

Figure 5.1: Travel-time considerations for depth-dependent-velocity plane-wave migration [2].

First, we equate the two-way travel time $\frac{2\Delta\hat{z}}{c_z}$ along the segment *BC* (zero-offset with respect to *x*) to the travel time $\frac{DC + \mathrm{CB}}{c_z}$ along the path *DCB*, including the arrival-time correction $-\Delta t_z$ for point *D* due its nonzero-offset position:

$$\frac{2\Delta\hat{z}}{c_z} = \frac{\Delta z}{c_z}\left[1 + \frac{1}{\cos\theta_z}\right] - \Delta t_z \ .$$

The nonzero-offset point *D* is reached from the point D^* through the previous layer extending from $z - \Delta z$ to z, where a refracted plane wave travels at an angle $\theta_{z-\Delta z}$ with the velocity $c_{z-\Delta z}$. Figure 5.1 shows the wavefront line L^*, from which the zero-offset point *B* is reached. To account for the nonzero-offset position of *D*, the travel time Δt_z from D^* to L^* needs to be subtracted. We have

$$\Delta t_z = \frac{D^*B^*\,|\sin\theta_{z-\Delta z}|}{c_{z-\Delta z}} = p\Delta z|\tan\theta_z| \ , \tag{5.4}$$

where $p = \frac{|\sin\theta_{z-\Delta z}|}{c_{z-\Delta z}}$ is referred to as the ray parameter.

Therefore,

$$\Delta\hat{z} = \frac{\Delta z}{2}\left[1 + \frac{1}{\cos\theta_z} - pc_z|\tan\theta_z|\right] \ . \tag{5.5}$$

The ray parameter is the same for all layers (Snell's law):

$$p = \frac{|\sin\theta_z|}{c_z} = \frac{|\sin\theta_{z-\Delta z}|}{c_{z-\Delta z}} = \cdots = \frac{|\sin\theta|}{c} \ , \tag{5.6}$$

where θ and c are the angle and the velocity of the plane wave emitted at the surface, respectively. Expressing θ_z in terms of c_z, c, and θ, equation (5.5) becomes as follows:

$$\Delta\hat{z} = \frac{\Delta z}{2}\left[1 + \sqrt{1 - \left(\frac{c_z}{c}\right)^2 \sin^2\theta}\ \right] = \Delta z\ \frac{(1+\cos\theta_z)}{2} \ . \tag{5.7}$$

Note that equation (5.7) can also be derived from the travel time relationship $\frac{2\Delta\hat{z}}{c_z} = \frac{(LC+BC)}{c_z}$, where L denotes the zero-offset wavefront line as shown in Figure 5.1. Using $\Delta\hat{z}$ instead of Δz effectively results in the transformation $z + \Delta z$ to $z^* + \Delta\hat{z}$, where z^* is obtained layer-by-layer using $\Delta z^* = \Delta\hat{z} = \Delta z\ \frac{(1+\cos\theta_z)}{2}$. Hence, for plane-wave emissions with $\theta \neq 0$, we have:

$$P_\theta(x, z^* + \Delta\hat{z}, 0) = \iint_{f^2 > c_z^2 k_x^2} \left[\Psi(k_x, z^* + \Delta\hat{z}, f) e^{j2\pi k_x x}\right] dk_x df \ , \tag{5.8}$$

where

$$\hat{\Psi}_\theta(k_x\ , z^* + \Delta\hat{z}\ , f) = \ \Psi_\theta(k_x\ , z^*\ , f) e^{j2\pi\hat{k}_z\Delta\hat{z}} \ , \tag{5.9}$$

with initial $\Psi_\theta(k_x, z^*, f) = \Psi(k_x, 0, f)$ at $z^* = 0$.

The remaining difference between $z^* + \Delta\hat{z}$ and $\hat{z} + \Delta\hat{z}$, is the term $x\frac{\tan\theta_z}{2}$ that accounts for the positional differences between the actual plane-wave emission (centered at $x = 0$) and the assumed zero-offset wavefront crossing a given $x \neq 0$. Once we have computed $P_\theta(x, z^*, 0)$ for all z^* values of interest, final $P_\theta(x, \hat{z}, 0) = P_\theta\left(x, z^* + x\frac{\tan\theta_z}{2}, 0\right)$ can be obtained for each layer via interpolation along the z^*-axis, where $\tan\theta_z = \frac{1}{\sqrt{\left(\frac{1}{\sin\theta_z}\right)^2 - 1}}$ and $\sin\theta_z = \frac{c_z}{c}\sin\theta$.

In summary, our proposed plane-wave phase-shift migration method consists of the following steps.

Step 1: Compute $\Psi(k_x, 0, f)$ by applying the Fourier transform $P(x, 0, t)$. Set z^* to zero and initialize $\Psi_\theta(k_x, z^*, f)$ to $\Psi(k_x, 0, f)$.

Step 2: Set $\Psi_\theta(k_x, z^*, f)$ to zero whenever $f^2 > c_z^2 k_x^2$. Determine $\Delta\hat{z}$ and compute $\Psi_\theta(k_x, z^* + \Delta\hat{z}, f)$ using equations (5.7) and (5.9).

Step 3: Sum $\Psi_\theta(k_x, z^* + \Delta\hat{z}, f)$ along the *f*-axis, and then apply the inverse Fourier transform along the k_x-axis, thus producing $P_\theta(k_x, z^* + \Delta\hat{z}, f)$, in accordance with

equation (5.8). Set z^* to $z^* + \Delta\hat{z}$ and go to Step 2, until the desired depth has been reached.

Step 4: For each layer (i.e., each c_z), obtain final $P_\theta(k_x, \hat{z}, 0)$ from $P_\theta(k_x, z^*, 0)$ via interpolation along the z^*-axis, according to the formula $\hat{z} = z^* + x\frac{\tan\theta_z}{2}$.

Chapter 6

Plane-Wave Phase-Shift Migration: Evaluation Results

6.1 Simulated Point Targets

To evaluate our proposed phase-shift migration method for plane-wave ultrasound imaging, we have used the K-WAVE MATLAB toolbox [85] to simulate signal acquisition under the following assumptions. A 128-element linear transducer (0.308-mm pitch) emits a 2-MHz plane-wave Gaussian pulse (wavelength λ = 0.770 mm, 4.5 cycles), which propagates through a three-layer medium towards ball-shaped "point" targets (0.616-mm diameter) located at the following (x, z) coordinates:

a) Upper targets: (-13, 22), (0, 22), (13, 22) mm;

b) Middle targets: (-13, 35), (0, 35), (13, 35) mm;

c) Lower targets: (-13, 48), (0, 48), (13, 48) mm.

The propagation medium properties are specified in Table 6.1, mimicking an approximate tissue-bone-tissue layer arrangement. The simulated bone layer extends from 5 mm to 12 mm along the z-axis (depth). The sound speed within this layer is 3198 m/s [81], which is substantially different from the sound speed of 1540 m/s within the adjacent tissue

layers. To enable coherent compounding, we have simulated nine emissions using $\theta = 0^o$, $\pm 4^o$, $\pm 8^o$, $\pm 12^o$, $\pm 16^o$.

Table 6.1: Propagation medium specifications.

Medium layer	Speed c_z, (m/s)	Density, kg/m^3	Absorption coefficient, dB/cm-MHz	Depth span, mm
I	1540	1000	0.75	$0 \leq z < 5$
II	3198	1990	3.54	$5 \leq z < 12$
III	1540	1000	0.75	$12 \leq z < 63$

During simulation, we set the spatial grid spacing at $\lambda/5 = 0.154$ mm and the temporal sampling frequency at 80 MHz. The resulting raw RF datasets of size 128×6592 in the (x, t)-domain were amplified using the time-gain compensation coefficient of 0.4 dB/cm-MHz. During depth migration, we set $\Delta z = \lambda/10 = 0.077$ mm, and the Fourier-domain grid was $2^8 \times 2^{13}$ in size.

Our presented images have been obtained in three steps. First, we sum individual migrated datasets corresponding to each θ value under consideration. Then, within each individual layer boundaries, we perform envelope detection and compression, followed by normalization to a maximum, so that each layer's envelope data range is limited to [0, 1].

In addition, prior to envelope detection, we linearly interpolate the compounded dataset to increase the number of the x-axis grid points by the factor of 4. Finally, we stack the resulting layer subimages to form an entire image.

The complexity of our modified Gazdag's method is dominated by the extrapolation process, whose complexity is $O(n_x n_t^2)$. Table 6.2 provides a breakdown of computational complexities associated with each reconstruction step. The average observed execution time per frame was 2.90 seconds (using the same workstation described in Chapter 4), where the size of each frame was $n_x \times n_t = 128 \times 7252$ (over the three layers in question).

Table 6.2: Complexity of individual steps per frame in phase-shift migration.

Reconstruction Method	Steps	Execution Time Complexity
Phase-shift	2-D FFT	$O(n_x n_t \log(n_x n_t))$
	Phase shift n_l layers	$O(n_x n_t n_l)$
	Extrapolation operation and summation	$O(n_x n_t^2)$
	1-D IFFT	$O(n_x n_t \log(n_x))$
	1-D linear interpolation $\hat{z} = z^* + x\frac{\tan\theta}{2}$	$O(n_x n_t)$

Figure 6.1 (top) shows the image for $\theta = 0^o$ that has been migrated assuming the constant velocity of 1540 m/s throughout the propagation medium. Its poor quality demonstrates the impact of depth-dependent velocity variations that must be taken into account. On the

other hand, Figure 6.1 (bottom) shows the alternative image for $\theta = 0^{o}$ that has been reconstructed using our proposed migration method; clearly, the layer boundaries and point targets are imaged more accurately.

Figure 6.2 shows the migrated image whose quality has been improved by means of coherent compounding given nine plane-wave emissions using $\theta = 0^{o}, \pm 4^{o}, \pm 8^{o}, \pm 12^{o}, \pm 16^{o}$. Table 6.3 lists the lateral FWHM values for the upper, middle, and lower target groups, where each group consists of three "points" labeled *L* (leftmost), *C* (central), and *R* (rightmost). It can be seen that coherent compounding using nine plane waves has improved target resolution quality by approximately 19% on average. Figure 6.3 demonstrates this improvement visually, showing the lateral cross-section of the respective point targets in question: due to coherent compounding, their shapes become more narrow, and the ringing artifacts become less noticeable.

The evaluation results presented in this section indicate that our proposed plane-wave phase-shift migration method is capable of handling velocity variations due to the presence of a horizontal bone-like layer extending from 5 to 12 mm in depth. In practice, the layer boundaries and the associated velocities would need to be estimated beforehand [62]. In the following sections, we will briefly explore our method's performance under erroneous assumptions about:

1) the propagation velocity value within the bone layer,
2) the bone layer boundaries.

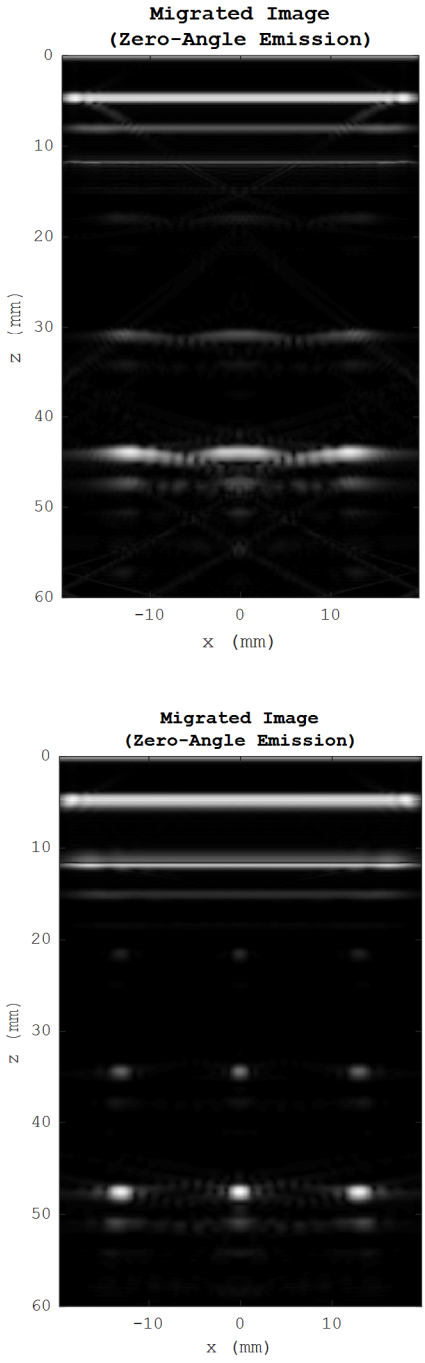

Figure 6.1: Constant-velocity migration (top) and our proposed method (bottom), using a single plane-wave emission at zero angle [2].

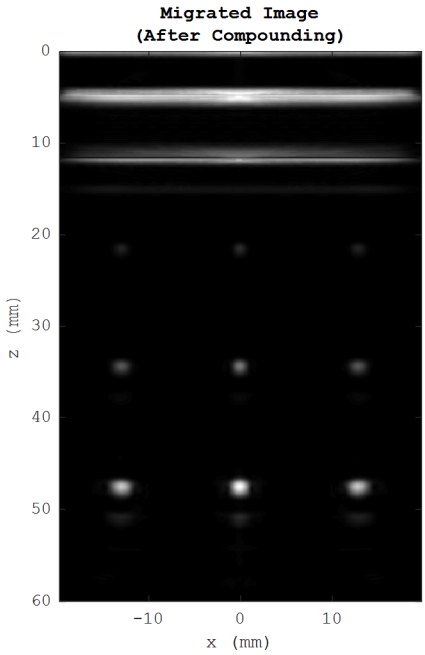

Figure 6.2: Our proposed method with compounding, using $\theta = 0^{o}, \pm 4^{o}, \pm 8^{o}, \pm 12^{o}, \pm 16^{o}$. [2].

Table 6.3: Target resolution quality (Lateral FWHM).

Target Group	One Plane Wave, FWHM, mm			Nine Plane Waves, FWHM, mm		
	L	*C*	*R*	*L*	*C*	*R*
Upper	1.683	1.392	1.712	1.367	1.181	1.365
Middle	1.994	1.617	2.019	1.605	1.329	1.609
Lower	2.413	2.040	2.432	1.910	1.643	1.923

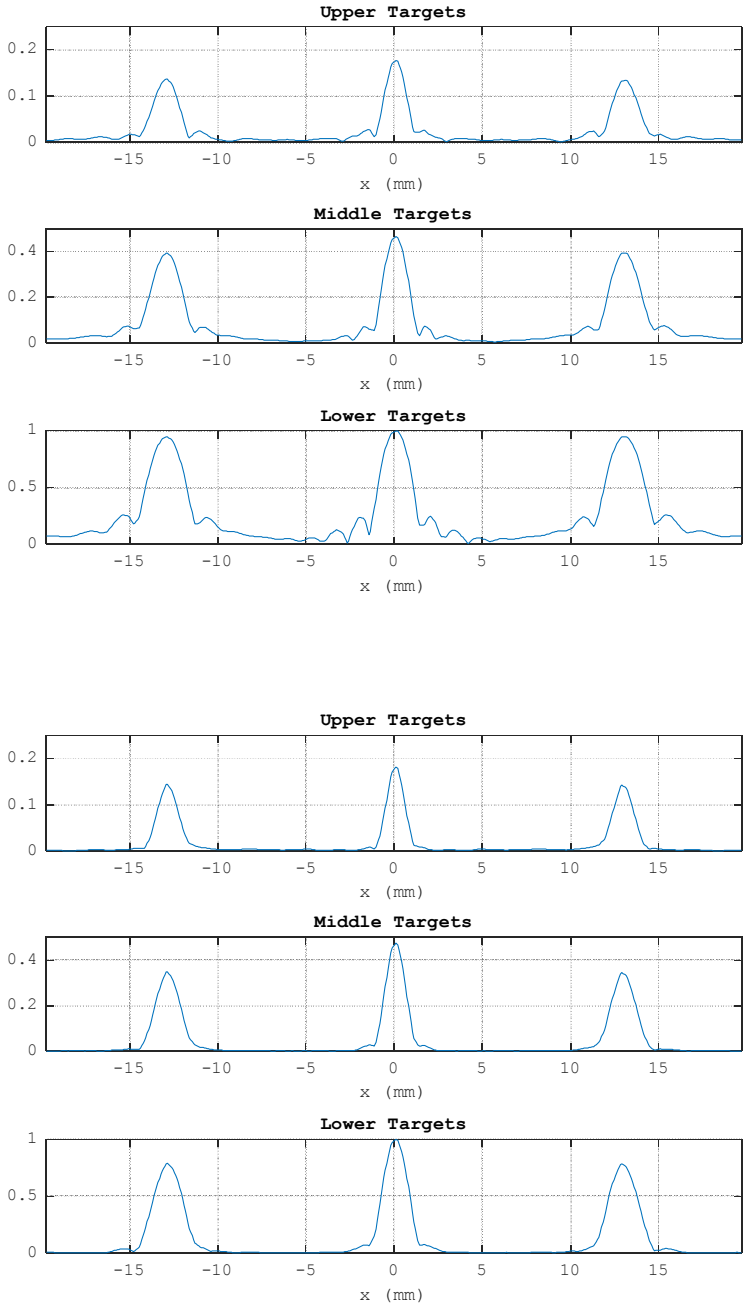

Figure 6.3: Cross-section of targets, single-emission image (top) and compounded image (bottom).

6.2 Sensitivity to Velocity Value Mismatch

In this section, we examine the sensitivity of our method to the mismatch between the "true" velocity of 3198 m/s in the bone layer and the assumed velocity during the migration process. We have investigated several scenarios, where the deviations from the value were set at ±5%, ±10%, ±15%, ±20%. For brevity, we will show only migrated images (using a single-emission scenario) in which the velocity has been underestimated and overestimated by -20% and +20%, respectively.

Figure 6.5 illustrates the sensitivity of our method to a +20% error in the speed of sound through the bone layer, which yields 3838 m/s. On the other hand, in Figure 6.6 the image is migrated using the velocity of 2558 m/s, which represents a -20% error in the "true" velocity of 3198 m/s. As can be seen in Figure 6.5, the image is slightly overmigrated, i.e., the hyperbolas in the (x, t)-domain have taken convex shapes on the image plane, instead of collapsing into focused "point" targets. Meanwhile, Figure 6.6 exhibits the opposite phenomenon: the hyperbolas in the (x, t)-domain have taken concave shapes, due to undermigration caused by the use of the underestimated velocity value for the bone layer. It is worth noting that, the "points" are misplaced from their true positons (downward due to overmigration, or upward due to undermigration).

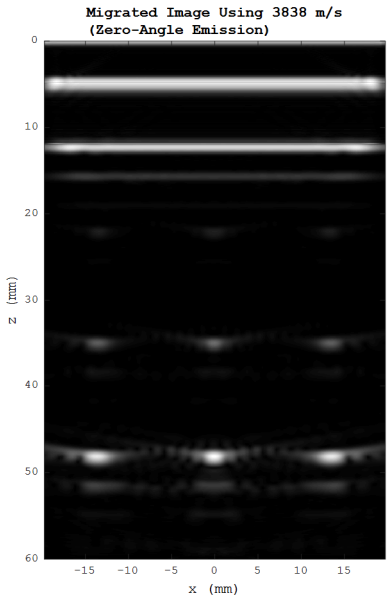

Figure 6.5: Zero-angle plane-wave emission, migrated image using overestimated velocity (+20%, bone layer).

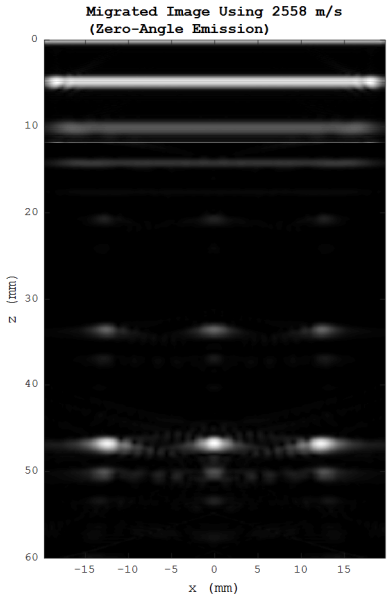

Figure 6.6: Zero-angle plane-wave emission migrated, image using underestimated velocity (-20%, bone layer) .

6.3 Sensitivity to Layer Boundary Mismatch

In the previous section, we assumed the bone layer boundaries were known precisely, but we let the sound speed within that layer deviate from its "true" value of 3198 m/s by as much as ±20% during migration. Here, we assume that the sound speed knowledge is accurate, but we let the bone layer boundaries deviate from their "true" depth positions (i.e., starting at 5 mm and ending at 12 mm). We have examined the following six mismatch scenarios.

a) The bone layer extends from 5 mm to 14 mm in depth; that is, its lower boundary is moved downward by 2 mm, which makes the layer 9-mm thick.
b) The bone layer extends from 3 mm to 12 mm in depth; that is, its upper boundary is moved upward by 2 mm, which makes the layer 9-mm thick.
c) The bone layer extends from 5 mm to 10 mm in depth; that is, its lower boundary is moved upward by 2 mm, which makes the layer 5-mm thick.
d) The bone layer extends from 7 mm to 12 mm in depth; that is, its upper boundary is moved downward by 2 mm, which makes the layer 5-mm thick.
e) The bone layer extends from 7 mm to 14 mm in depth; that is, it is shifted downward by 2 mm while maintaining its "true" thickness of 7 mm.
f) The bone layer extends from 3 mm to 10 mm in depth; that is, it is shifted upward by 2 mm while maintaining its "true" thickness of 7 mm.

In all of the above six cases, a single zero-angle plane-wave emission was used to obtain the migrated images shown in Figures 6.7-6.12.

Figures 6.7 and 6.8, where the 9-mm layer thickness (assumed during migration) is greater than the "true" value of 7 mm, show that the "point" targets are overmigrated, with some artifacts present within the bone layer boundaries. The overmigration effect is attributed to the fact that, the extrapolator iterated over the extended high-velocity bone layer; therefore, by the time it reaches the "point" targets, the wavefield is effectively over-extrapolated ahead.

Figures 6.9 and 6.10, where the 5-mm bone layer thickness (assumed during migration) is less than the "true" value of 7 mm, show that "point" targets are slightly out of focus due to undermigration, and the boundaries of the bone layer are misplaced. Since the high-velocity bone layer is squeezed by 2 mm, by the time the extrapolator reaches the "point" targets the wavefield is still lagging behind.

Figures 6.11 and 6.12, where the 7-mm bone layer is shifted by 2 mm upward and downward, respectively, during migration, show that the "point" targets remain focused; however, the boundaries of the bone layer appear shifted upward and downward, respectively. These shifts affect the bone layer boundaries as expected; however, once the wavefield is extrapolated beyond that layer, the "point" targets are migrated correctly.

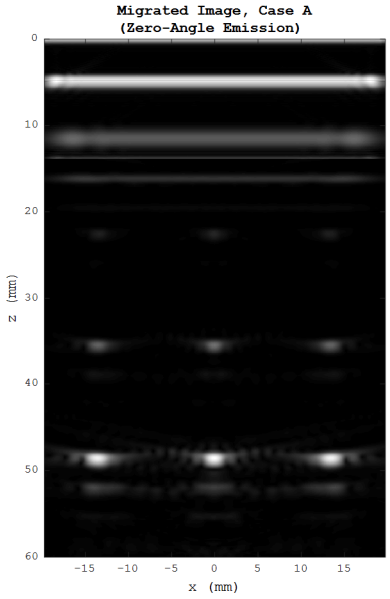

Figure 6.7: Zero-angle plane-wave emission, migrated image, case (a).

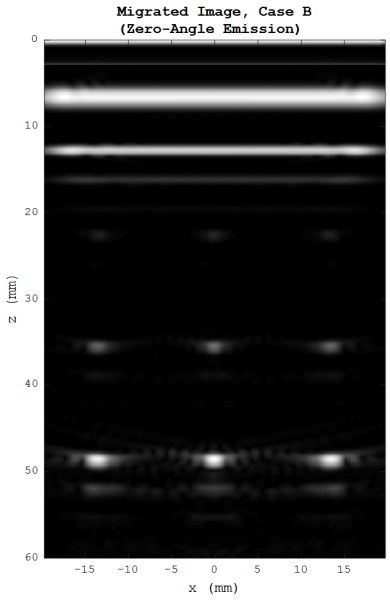

Figure 6.8: Zero-angle plane-wave emission, migrated image, case (b).

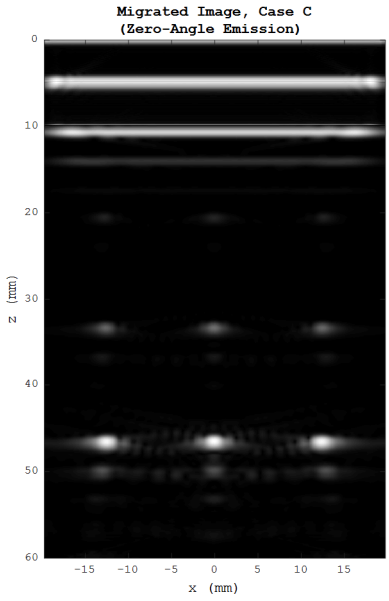

Figure 6.9: Zero-angle plane-wave emission, migrated image, case (c).

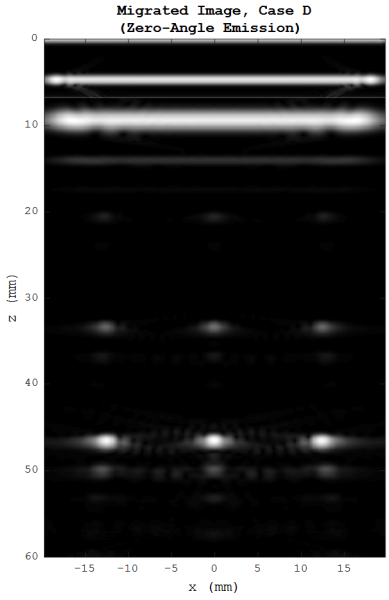

Figure 6.10: Zero-angle plane-wave emission, migrated image, case (d).

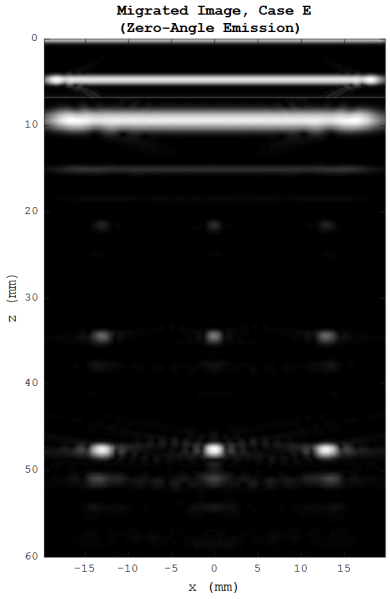

Figure 6.11: Zero-angle plane-wave emission, migrated image, case (e).

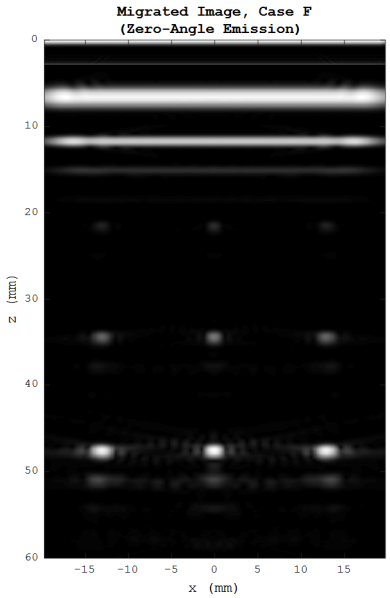

Figure 6.12: Zero-angle plane-wave emission, migrated image, case (f).

Chapter 7

Conclusions and Future Work

In this chapter we briefly summarize our main results and outline several potential directions of future research and development efforts.

7.1 Conclusions

In Chapter 3, we have described novel variants of zero-offset constant-velocity Stolt's and slant-stack migration methods that can be used for plane-wave ultrasound image reconstruction in the spatio-temporal Fourier domain. In Chapter 4, their imaging performance has been demonstrated using the *in-vitro* and *in-vivo* RF data provided by PICMUS [17]. Our proposed methods have also been compared to the three existing Fourier-domain techniques reported in the ultrasound literature, namely, Lu's method [11,50], Garcia's method [21], and UFSB [8, 9].

The compounded images of *in-vitro* phantoms were obtained using three acquisition scenarios:

a) one plane-wave emission (at zero angle),

b) 11 plane-wave emissions,

c) 75 plane-wave emissions.

Steering angles ranged from -16^{o} to +16^{o} [17]. In each scenario, image quality was evaluated based on the cyst CNR values (two anechoic cylinder targets) and the average lateral FWHM values (seven 100-micron wire targets). The compounded images of *in-vivo* carotid artery sections [17] were obtained using 75 plane-wave emissions processed by a DAS-Hamming beamformer, and 11 plane-wave emissions processed by the Fourier-domain methods under consideration. The envelope data of the latter was individually compared to that of the former (used as a reference) to assess their relative similarity based on the SSIM and MSE values.

While no single Fourier-domain technique performed consistently better than the others, our methods produced superior image contrast, resolution, and similarity indicators in most test cases under consideration, which demonstrates their competitive potential. It is worth emphasizing that our derivations of the proposed plane-wave constant-velocity Stolt's and slant-stack migration methods rely the same underlying model, which could be useful when adapting other geophysical data processing techniques to plane-wave ultrasound imaging.

In Chapter 5, we have described a novel Fourier-domain technique for reconstructing plane-wave ultrasound images when the speed of sound varies with depth in a propagation medium. Starting from classic Gazdag's phase-shift migration method used for geophysical data processing, we have shown how one can obtain modified zero-offset model equations applicable to plane-wave ultrasound imaging. In Chapter 6, our simulation results using K-WAVE MATLAB toolbox show that the proposed method is capable of accurately imaging point targets in a three-layer medium, mimicking tissue-bone-tissue ultrasound propagation.

7.2 Future Work

There are several promising research directions that one can pursue based on the work presented here; for example, further reducing the computational complexity of our Stolt's and slant-stack migration methods via numerical approximations, coupling them with adaptive apodization, and applying sparse reconstruction schemes. Furthermore, our slant-stack migration method can certainly benefit from finding the optimal number of slants and optimal spacing between them, which is likely to be data-dependent, thus motivating further investigations into adaptive slant-stack techniques in the future. Other promising research directions include adaptive pre- and post-migration filtering and multimode migration using multiple methods during compounded image reconstruction.

Our phase shift migration algorithm can be further extended to account for the modeling error of the speed-of-sound profile. Such extensions will improve ultrasound imaging quality by decreasing the focusing error. For example, the associated velocities would need to be estimated beforehand using methods such as velocity spectrum mapping techniques [62]. They were originally used to estimate the velocity before applying the NMO delay to obtain the aligned CMP section; hence, they need to be modified to handle the case of plane-wave emissions. Another important problem is dealing with lateral velocity variations, which could be based on methods such as the split-step Fourier migration [76], Gaussian beam migration [34], and spatial FIR filtering [61]. Handling propagation velocity variations along both the lateral and axial will enable more accurate imaging of heterogeneous biological medium. As for the efficiency aspect, our phase-shift migration could be used in conjunction with our Stolt's method based on the ideas presented in [74].

Bibliography

[1] M. Albulayli and D. Rakhmatov, "Fourier-Domain depth migration for plane-wave ultrasound imaging," *IEEE Transactions on Ultrasonics, Ferroelectrics, and Frequency Control*, vol. 65, no. 8, pp. 1321-1333, Aug. 2018.

[2] M. Albulayli and D. Rakhmatov, "Phase-shift depth migration for plane-wave ultrasound imaging," *2018 Annual International Conference of the IEEE Engineering in Medicine and Biology Society,* pp.1-6, July 2018.

[3] M. Albulayli, D. Rakhmatov, "Dynamic receive aperture downsampling for ultrasound imaging," *IEEE International Conference on Acoustics, Speech and Signal Processing* (*ICASSP*), pp. 5130-5134, May 2014.

[4] M. Albulayli, D. Rakhmatov, "Hybrid adaptive/nonadaptive beamforming for ultrasound imaging," *IEEE International Conference on Acoustics, Speech and Signal Processing* (*ICASSP*), pp. 1061-1065, May 2013.

[5] M. Ali, D. Magee, and U. Dasgupta. *"*Signal processing overview of ultrasound systems for medical imaging*." SPRAB12, Texas Instruments*, Texas, Nov. 2008.

[6] B. M. Asl and A. Mahloojifar, "Eigenspace-based minimum variance beamforming applied to medical ultrasound imaging," *IEEE Transactions on Ultrasonics, Ferroelectrics, and Frequency Control*, vol.57, no.11, pp.2381-2390, Nov. 2010.

[7] A. J. Berkhout, "A unified approach to acoustical reflection imaging, Part I: The forward model," *The Journal of the Acoustical Society of America,* vol.93, pp. 2005-2016, Oct. 1993.

[8] O. Bernard, M. Zhang, F. Varray, P. Gueth, J. Thiran, H. Liebgott, and D. Friboulet, "Ultrasound Fourier slice imaging: a novel approach for ultrafast imaging technique," *Proceedings. IEEE Ultrasonics Symposium* pp. 129–132, Sept. 2014.

[9] A. Besson, M. Zhang, F. Varray, H. Liebgott, D. Friboulet, Y. Wiaux, J. Thiran, R. Carrillo, and O. Bernard, "A sparse reconstruction framework for Fourier-based plane-wave imaging," *IEEE Transactions on Ultrasonics, Ferroelectrics, and Frequency Control,* vol. 63, no. 12, pp. 2092–2106, Dec. 2016.

[10] G. Chau, R. Lavarello, and J. Dahl, “Short-lag spatial coherence weighted minimum variance beamformer for plane-wave images,” *IEEE Ultrasonics Symposium*, pp. 1–3, Sept. 2016.

[11] J. Cheng and J.-Y. Lu, “Extended high frame rate imaging method with limited diffraction beams,” *IEEE Transactions on Ultrasonics, Ferroelectrics, and Frequency Control*, vol. 53, pp. 880–899, May 2006.

[12] T. Chernyakova, Y. Eldar, “Fourier-domain beamforming: the path to compressed ultrasound imaging," *IEEE Transactions on Ultrasonics, Ferroelectrics, and Frequency Control*, vol.61, no.8, pp.1252-1267, Aug. 2014.

[13] CIRS, “Multi-Purpose Multi-Tissue Ultrasound Phantom, Model 040GSE,” 2013. [Online]. Available: http://www.cirsinc.com/products/ all/67/multi-purpose-multi-tissue-ultra%sound-phantom/.

[14] J. F. Claerbout, *Imaging the Earth’s Interior*. Blackwell Science, 1985 [Online]. Available: http://sepwww.stanford.edu/sep/prof/iei/toc_html/.

[15] R. Cobbold, *Foundations of Biomedical Ultrasound*. NY: Oxford University Press, 2007.

[16] R. Cohen, Y. Sde-Chen, T. Chernyakova, C. Fraschini, J. Bercoff and Y. Eldar, "Fourier domain beamforming for coherent plane-wave compounding," *2015 IEEE International Ultrasonics Symposium (IUS)*, 2015, pp. 1-4.

[17] CREATIS, “Plane-wave Imaging Challenge in Medical UltraSound: PICMUS.” [Online]. available: https://www.creatis.insa-lyon.fr/Challenge/IEEE IUS 2016/

[18] A. Deylami, J. Jensen, and B. Asl, “An improved minimum variance beamforming applied to plane-wave imaging in medical ultrasound,” *IEEE Ultrasonics Symposium*, pp. 1–4, Sept. 2016.

[19] Y. Eldar "*Sampling Theory: Beyond Bandlimited Systems*", Cambridge University Press, April 2015.

[20] J. Fessler, B. Sutton, "Nonuniform fast Fourier transforms using min-max interpolation," *IEEE Transactions on Signal Processing*, vol.51, no.2, pp.560-574, Feb. 2003.

[21] D. Garcia, L. Tarnec, S. Muth, E. Montagnon, J. Porée, G. Cloutier,"Stolt's f-k migration for plane wave ultrasound imaging," *IEEE Transactions on Ultrasonics, Ferroelectrics, and Frequency Control*, vol.60, no.9, pp.1853-1867, Sept. 2013.

[22] J. Gazdag, P. Sguazzero, "Migration of seismic data," *Proceedings of the IEEE*, vol.72, no.10, pp.1302-1315, Oct. 1984.

[23] J. Gazdag and P. Sguazzero, "Migration of seismic data by phase shift plus interpolation," *Geophysics*, vol. 49, no. 2, pp. 124–131, Feb. 1984.

[24] J. Gazdag, "Wave equation migration with the phase-shift method," *Geophysics*, vol. 43, no. 7, pp. 1342–1351, Dec. 1978.

[25] R. Gonzalez, R. Woods, (2008). *Digital Image Processing* (3rd ed.). Upper Saddle River, N.J.: Prentice Hall.

[26] J. Goodman, *Introduction to Fourier Optics*. CO: Roberts and Company Publishers, 2005.

[27] J. Goutsias, and J. Mendel, "Inverse problems in two-dimensional acoustic media: A linear imaging model," *The Journal of the Acoustical Society of America*, vol.81, no.5, pp.1471-1485, May 1987.

[28] D. Guenther and W. Walker, "Optimal apodization design for medical ultrasound using constrained least squares, part I: theory," *IEEE Transactions on Ultrasonics, Ferroelectrics, and Frequency Control*, vol.54, no.2, pp.332-342, Feb. 2007.

[29] D. Guenther and W. Walker, "Optimal apodization design for medical ultrasound using constrained least squares, part II: simulation results," *IEEE Transactions on Ultrasonics, Ferroelectrics, and Frequency Control*, vol.54, no.2, pp.343-358, Feb. 2007.

[30] D. Guenther and W. Walker, "Robust finite impulse response beamforming applied to medical ultrasound," *IEEE Transactions on Ultrasonics, Ferroelectrics, and Frequency Control*, vol.56, no.6, pp.1168-1188, June 2009.

[31] D. Hale, "Stable explicit depth extrapolation of seismic wavefields," *Geophysics*, vol. 56, no. 11, pp. 1770–1777, Nov. 1991.

[32] M. A. Haun. *New Approaches to Aberration Correction in Medical Ultrasound Imaging*. Ph.D. dissertation, University of Illinois at Urbana-Champaign, 2003.

[33] W. Harlan, "Avoiding interpolation artifacts in Stolt migration," *Stanford Exploration Project*, vol. 30, pp. 103–110, 1982.

[34] N. Hill, "Gaussian beam migration," *Geophysics*, vol. 55, no. 11, pp. 1416–1428, Nov 1990.

[35] I. Holfort, F. Gran, and J. Jensen, "Broadband minimum variance beamforming for ultrasound imaging," *IEEE Transactions on Ultrasonics, Ferroelectrics, and Frequency Control*, vol.56, no.2, pp.314-325, Feb. 2009.

[36] K. W. Hollmand, K. W. Rigby, and M. O'Donnell, "Coherence factor of speckle from a multi-row probe," *IEEE Ultrasonics Symposium*, pp.1257-1260, 1999.

[37] A. Hunter, B. Drinkwater, and P. Wilcox, "The wavenumber algorithm for full-matrix imaging using an ultrasonic array," *IEEE Transactions on Ultrasonics, Ferroelectrics and Frequency Control,* vol. 55, no. 11, pp. 2450–2462, Nov. 2008.

[38] J. A. Jensen, "Medical ultrasound imaging," *in Progress in Biophysics and Molecular Biology*, vol.93, issues 1–3, pp. 153-165, Jan. 2007.

[39] J. A. Jensen *et al*., "Ultrasound research scanner for real-time synthetic aperture data acquisition," *IEEE Transactions on Ultrasonics, Ferroelectrics, and Frequency Control*, vol. 52, no. 5, pp. 881-891, May 2005.

[40] J. A. Jensen: *Linear description of ultrasound imaging systems,* Notes for the International Summer School on Advanced Ultrasound Imaging, Technical University of Denmark, July 1999.

[41] D. Johnson and D. Dudgeon, *Array Signal Processing: Concepts and Techniques*. Upper Saddle River, NJ: Prentice-Hall, 1993.

[42] L. J. Karam and J. H. McClellan, "Efficient design of digital filters for 2-D and 3-D depth migration," *IEEE Transactions on Signal Processing*, vol. 45, no. 4, pp. 1036–1044, Apr. 1997.

[43] P. Kearey, M. Brooks, and I. Hill., *An Introduction to Geophysical Exploration*. Blackwell Science, 3rd edition, 2002.

[44] S. Khezerloo and D. Rakhmatov, "Gradient-driven beamforming for biomedical ultrasound," *2009 Annual International Conference of the IEEE Engineering in Medicine and Biology Society*, pp. 444-450, Sept. 2009.

[45] J. Kirkhorn, "Introduction to IQ-demodulation of RF-data," Technical Report, Norwegian University of Science and Technology, Trondheim, Norway, Sept.1999, http://folk.ntnu.no/htorp/Undervisning/TTK10/IQdemodulation.pdf (last accessed 12/11/2015).

[46] P. Kruizinga, F. Mastik, N. de Jong, A. F. W. van der Steen, and G. van Soest, "Plane-wave ultrasound beamforming using a nonuniform fast Fourier transform," *IEEE Transactions on Ultrasonics, Ferroelectrics, and Frequency Control*, vol. 59, no. 12, pp. 2684–2691, Dec. 2012.

[47] T. Lehmann, C. Gonner, K. Spitzer, "Survey: interpolation methods in medical image processing," *IEEE Transactions on Medical Imaging*, vol.18, no.11, pp.1049-1075, Nov. 1999.

[48] H. Liebgott, A. Rodriguez-Molares, F. Cervenansky, J. Jensen, and O. Bernard, "Plane-wave imaging challenge in medical ultrasound," *IEEE Ultrasonics Symposium*, pp. 1–4, Sept. 2016.

[49] D. L. Liu, "Plane wave scanning reception and receiver," U.S. Patent, No. 6685641 B2, issued Feb. 3, 2004.

[50] D. Liu and T. Ji, "Plane wave image formation in spatial-temporal frequency domain," *2016 IEEE International Ultrasonics Symposium (IUS)*, Tours, 2016, pp. 1-5.

[51] D. L. Liu and R. C. Waag, "Propagation and backpropagation for ultrasonic wavefront design," *IEEE Transactions on Ultrasonics, Ferroelectrics, and Frequency Control*, vol. 44, no. 1, pp. 1–13, Jan. 1997.

[52] B. Lokesh and A. Thittai, "Spatial resolution improvement in plane wave imaging using adaptive sign coherence factor weighting," *IEEE Ultrasonics Symposium*, pp. 1–4, Sept 2016.

[53] J.-Y. Lu, "Experimental study of high frame rate imaging with limited diffraction beams," *IEEE Transactions on Ultrasonics, Ferroelectrics, and Frequency Control*, vol. 45, pp. 84–97, Jan. 1998.

[54] J.-Y. Lu, "2-D and 3-D high frame rate imaging with limited diffraction beams," *IEEE Transactions on Ultrasonics, Ferroelectrics, and Frequency Control*, vol. 44, pp. 839–856, Jul. 1997.

[55] J.-Y. Lu and J. F. Greenleaf, "Ultrasonic nondiffracting transducer for medical imaging," *IEEE Transactions on Ultrasonics, Ferroelectrics, and Frequency Control*, vol. 37, pp. 438–447, Sept. 1990.

[56] G. F. Margrave, "*Numerical Methods of Exploration Seismology"*. CREWES Educational Resources, 2003 [Online]. Available: http://www.crewes. org/ResearchLinks/FreeSoftware/NumMeth.pdf

[57] S. Marple, "Computing the discrete-time "analytic" signal via FFT," *IEEE Transactions on Signal Processing*, vol.47, no.9, pp.2600-2603, Sept. 1999.

[58] G. Matrone, A. Savoia, and G. Magenes, “Filtered delay multiply and sum beamforming in plane-wave ultrasound imaging: Tests on simulated and experimental data,” *IEEE Ultrasonics Symposium*, pp. 1–4, Sept. 2016.

[59] E. Moghimirad, C. V. Hoyos, A. Mahloojifar, B. Asl, and J. Jensen, “Synthetic aperture ultrasound Fourier beamformation using virtual sources,” *IEEE Transactions on Ultrasonics, Ferroelectrics and Frequency Control,* vol. 63, no. 12, pp. 2018–2030, Dec. 2016.

[60**]** G. Montaldo, M. Tanter, J. Bercoff, N. Benech, and M. Fink, “Coherent plane-wave compounding for very high frame rate ultrasonography and transient elastography,” *IEEE Transactions on Ultrasonics, Ferroelectrics, and Frequency Control*, vol. 56, no. 3, pp. 489–506, Mar. 2009.

[61] W. A. Mousa, "Imaging of the SEG/EAGE Salt Model Seismic Data Using Sparse *f-x* Finite-Impulse-Response Wavefield Extrapolation Filters," *IEEE Transactions on Geoscience and Remote Sensing*, vol. 52, no. 5, pp. 2700-2714, May 2014.

[62] W. A. Mousa and A. A. Al-Shuhail, “Processing of seismic reflection data using MATLAB,” *Synthesis Lectures Signal Processing*, vol. 5, no. 1, pp. 1–97, Sept. 2011.

[63] C. Nilsen, I. Hafizovic, "Beamspace adaptive beamforming for ultrasound imaging," *IEEE Transactions on Ultrasonics, Ferroelectrics and Frequency Control*, vol.56, no.10, pp.2187-2197, Oct. 2009.

[64] C. Nilsen and S. Holm, "Wiener beamforming and the coherence factor in ultrasound imaging," *IEEE Transactions on Ultrasonics, Ferroelectrics and Frequency Control*, vol.57, no.6, pp.1329-1346, June 2010.

[65] J. Quistgaard, "Signal acquisition and processing in medical diagnostic ultrasound," in *IEEE Signal Processing Magazine*, vol. 14, no. 1, pp. 67-74, Jan 1997.

[66] K. Ranganathan and W. Walker, "A novel beamformer design method for medical ultrasound, part I: theory," *IEEE Transactions on Ultrasonics, Ferroelectrics and Frequency Control*, vol.50, no.1, pp.15-24, Jan. 2003.

[67] K. Ranganathan and W. Walker, "A novel beamformer design method for medical ultrasound, part II: simulation results," *IEEE Transactions on Ultrasonics, Ferroelectrics and Frequency Control,* vol.50, no.1, pp.25-39, Jan. 2003.

[68] H. Rehouma, D. Rakhmatov and M. Albulayli, "Two-pass beamforming for ultrasound imaging," *IEEE International Symposium on Circuits and Systems (ISCAS),* pp. 25-28, May 2016.

[69] O. Rindal and A. Austeng, "Double adaptive plane-wave imaging," *IEEE Ultrasonics Symposium*, pp. 1–4, Sept. 2016.

[70] E. A. Robinson, "Image Reconstruction in Exploration Geophysics," *IEEE Transactions on Sonics and Ultrasonics*, vol. 31, no. 4, pp. 259-270, July 1984.

[71] M. Sasso and C. Cohen-Bacrie, "Medical ultrasound imaging using the fully adaptive beamformer," *IEEE International Conference on Acoustics, Speech and Signal Processing* (*ICASSP*), pp. 489- 492, Mar. 2005.

[72] T. Shah and T. Kailath, "Adaptive beamforming for coherent signals and interference," *IEEE Transactions on Acoustics, Speech and Signal Processing*, vol.33, no.3, pp. 527- 536, Jun 1985.

[73] R. Schmidt, "Multiple emitter location and signal parameter estimation," *IEEE Transactions on Antennas and Propagation*, vol.34, no.3, pp.276-280, Mar. 1986.

[74] M. Skjelvareid, T. Olofsson, Y. Birkelund, and Y. Larsen, " Synthetic aperture focusing of ultrasonic data from multilayered media using an omega-k algorithm," *IEEE Transactions on Ultrasonics, Ferroelectrics, and Frequency Control,* vol. 58, no. 5, pp. 1037–1048, 2011.

[75] T. Stepinski, "An implementation of synthetic aperture focusing technique in frequency domain," *IEEE Transactions on Ultrasonics, Ferroelectrics and Frequency Control,* vol. 54, no. 7, pp. 1399–1408, July 2007.

[76] P. Stoffa, J. Fokkema, R. Freire, W. Kessinger, "Split-step Fourier migration," *Geophysics*, vol. 55, no. 4, pp. 410–421, Apr. 1990.

[78] R. Stolt, "Migration by Fourier transform," *Geophysics*, vol. 63, no. 1, pp. 23–48, Feb. 1978.

[79] J-F. Synnevag, A. Austeng, and S. Holm, "Adaptive beamforming applied to medical ultrasound imaging," *IEEE Transactions on Ultrasonics, Ferroelectrics and Frequency Control,* vol.54, no.8, pp.1606-1613, Aug. 2007.

[80] J-F. Synnevag, A. Austeng, and S. Holm, "A low-complexity data-dependent, beamformer," *IEEE Transactions on Ultrasonics, Ferroelectrics and Frequency Control,* vol.58, no.2, pp.281-289, Feb. 2011.

[81] T. Szabo, *Diagnostic Ultrasound Imaging: Inside Out.* MA: Elsevier, 2014.

[82] M. Tanter and M. Fink, “Ultrafast imaging in biomedical ultrasound,” *IEEE Transactions on Ultrasonics, Ferroelectrics and Frequency Control,* vol. 61, no. 1, pp.102–119, Jan. 2014.

[83] P. Thevenaz, T. Blu, M. Unser, "Interpolation revisited [medical images application]," *IEEE Transactions on Medical Imaging*, vol.19, no.7, pp.739-758, July 2000.

[84] J. W. Thorbecke, K. Wapenaar, and G. Swinnen, “Design of one-way wavefield extrapolation operators, using smooth functions in WLSQ optimization,” *Geophysics*, vol. 69, no. 4, pp. 1037–1045, Jul. 2004.

[85] B. Treeby, B. Cox, and J. J, “k-Wave: A MATLAB toolbox for the time-domain simulation of acoustic wave fields.” [Online]. Available: http://www.k-wave.org/

[86] H. L. V. Trees, *Detection, Estimation, and Modulation Theory IV: Optimum Array Processing*. NY: Wiley, 2002.

[87] R. Tur, Y. Eldar, Z. Friedman, "Innovation rate sampling of pulse streams with application to ultrasound imaging," *IEEE Transactions on Signal Processing,* vol.59, no.4, pp.1827-1842, Apr. 2011.

[88] F. Varray, M. Kalkhoran, and D. Vray, “Adaptive minimum variance coupled with sign and phase coherence factors in IQ domain for plane wave beamforming,” *IEEE Ultrasonics Symposium*, pp. 1–4, Sept. 2016.

[89] Verasonics, “Vantage Research Ultrasound Systems,” 2017. [Online]. Available: http://verasonics.com/vantage-systems/

[90] F. Vignon, M. Burcher, "Capon beamforming in medical ultrasound imaging with focused beams,” *IEEE Transactions on Ultrasonics, Ferroelectrics, and Frequency Control,* vol.55, no.3, pp.619-628, Mar. 2008

[91] N. Wagner, Y. Eldar, Z. Friedman, "Compressed beamforming in ultrasound imaging," *IEEE Transactions on Signal Processing*, vol.60, no.9, pp.4643-4657, Sept. 2012.

[92] O. Yilmaz, *Seismic Data Analysis*, 2nd ed. OK: SEG, 2001, vol. 1.

[93] W. Zhou, A. Bovik, H. Sheikh, and E. Simonchelli, “Image quality assessment: from error visibility to structural similarity,” *IEEE Transactions on Image* Processing, vol. 13, no. 4, pp. 600–612, Apr. 2004.